QUARTIC: AN ULTRA-FAST TIME-OF-FLIGHT COUNTER

by

PEDRO MIGUEL DUARTE

Presented to the Faculty of the Graduate School of

The University of Texas at Arlington in Partial Fulfillment

of the Requirements

for the Degree of

MASTER OF SCIENCE IN PHYSICS

THE UNIVERSITY OF TEXAS AT ARLINGTON

August 2007

ACKNOWLEDGEMENTS

I want to thank several people who contributed to this project. The most important is my advisor Andrew Brandt who presented me with this idea when I arrived at UTA in 2005 and gave me the opportunity to work on it. I thank him for his support in difficult circumstances and I acknowledge his great effort in bringing the QUARTIC detector to life. Erik Ramberg at the Test Beam in Fermilab was also very supportive and I learned a great deal from him about data acquisition and about the patience necessary to debug systems that for moments make no sense. Joaquin Noyola and Shane Spivey from UTA provided valuable help. Joaquin helped me with the simulations of the QUARTIC detector and Shane helped with the analysis of Run I and II data and with Run II at the Test Beam. Arnab Pal also provided valuable discussions about the $H \to b\bar{b}$ decay in central exclusive production. I thank also collaborators Mike Albrow from Fermilab, Tomasz Pierzchala, Luc Bonnet, and Pierre Rodegheiro from UC Louvain and Sean Walston from LBNL for their efforts in Run I and II at the Test Beam. The help of Arnab Pal and Dipanjan Roy from UTA who went to Fermilab briefly during Run I to provide necessary manpower is also greatly appreciated. I also acknowledge the efforts in this Fast Timing venture by the rest of the collaboration members at UC Louvain and the University of Alberta: Krzysztof Piotrzkowski, Jim Pinfold, Yushu Yao, Lars Holm and John Schaapman.

June 28, 2007

ABSTRACT

QUARTIC: AN ULTRA-FAST TIME-OF-FLIGHT COUNTER

Publication No. _____

PEDRO MIGUEL DUARTE, M.S.

The University of Texas at Arlington, 2007

Supervising Professor: Andrew Brandt

The QUARTIC time-of-flight detector is a part of a proposed upgrade that adds proton taggers 420 m upstream and downstream of the ATLAS and CMS detectors. The entire project is called FP420 (Forward Protons at 420 meters), and it is an international collaboration with members from 10 countries and 29 institutions. Double proton tagging at 420m offers a unique opportunity to extend the discovery reach of the LHC and has the potential to give a high scientific return. Proton tagging may be the discovery channel for the Higgs boson in certain regions of the MSSM and, in most scenarios, will help untangle the properties of the Higgs and its charge and parity quantum numbers.

Fast time-of-flight counters are planned to dramatically decrease backgrounds to events with a massive central system and forward/backward protons, by using timing to confirm that the protons originated from the same vertex as the central system. QUARTIC's design uses an array of fused silica (quartz-like) bars aligned at an angle with respect to the beam. The protons pass through the bars and emit Cherenkov photons which are detected by a micro-channel plate photomultiplier tube at the end of the bars.

In this work I present the results of the first stage of R&D efforts for the QUARTIC detector. Preliminary studies and results of simulations of several detector geometries are summarized. The experimental tools and analysis framework developed to allow testing of the first two prototypes in the Meson Test Beam Facility at Fermilab are described. Finally the results obtained in August 2006 and March 2007 runs at the Test Beam are presented.

TABLE OF CONTENTS

LIST OF FIGURES

LIST OF TABLES

CHAPTER 1

INTRODUCTION

1.1 High Energy Physics and the Large Hadron Collider

The field of Physics known today as High Energy Physics stemmed from the discovery of elementary particles. By the 1970's the three interactions of subatomic physics—the strong, weak, and electromagnetic interactions—that govern the behavior of particles were clearly delineated but not entirely understood. The strong and the weak were still mysterious at the time. Hundreds of strongly interacting particles had been discovered without a unifying organization; and the weak interactions' property of parity violation had been discovered but its origin was not clear.

Today the situation is much better understood. All the strongly interacting particles are now understood to be bound states of quarks. The leptons—electron, muon, and tau along with its neutrinos—share with the quarks a structure of couplings to spin-1 bosons that accounts for their weak interactions. All three interactions are known to be mediated by spin-1 particles. The spin-1 particles are called gauge bosons and appear in the set of equations of motion called a Yang-Mills theory which has couplings representing a fundamental group of symmetries that characterizes each interaction. The resulting structure of interacting quarks, leptons and gauge bosons is called the Standard Model[1].

There are, however, conceptual difficulties with the Standard Model. For instance, the symmetry of the weak interaction group is not manifest in the masses of the weak interaction bosons $W^{\pm}$ and Z^0. It actually requires them to be massless and they have

[1]See Ref. [1] for more on the future experimental program implied by the Standard Model and the next stage of physics beyond it.

been observed to be heavy particles. The exact symmetry of the weak interaction as required by the Yang-Mills equations of motion can be spontaneously broken by the postulated Higgs scalar field. This is the simplest extension of the Standard Model and would account for the masses of the gauge bosons, leptons and quarks, but there is not much that we know about the Higgs field from experiment.

The Large Hadron Collider (LHC) is a proton-proton collider under construction in Geneva, Switzerland at the European Laboratory for Particle Physics, CERN. The LHC will have a center of mass energy of 14 TeV and at this high energy new physics (beyond the Standard Model) is expected to show up. Even with the first 1 fb^{-1} of data anticipated by the end of 2008, new physics could be observed in the form of quark substructure and excited quarks, high mass lepton pairs, discovery of the Higgs in the $WW \to \ell\ell\nu\nu$ channel, and the lightest supersymmetric particle [2].

1.2 Diffractive Physics at the LHC

The term diffraction comes from optics, where it describes the coherent phenomenon that occurs when a beam of light strikes an obstacle or passes through an opening. The light hitting the barrier is absorbed and the remaining wave propagates to the other side. The propagation and the interaction of hadrons is not so different in the sense that there is an absorption of their wave function caused by the many inelastic channels that are open at high center of mass energies.

In purely particle physics terms, diffractive high energy physics[2] encompasses the collisions in which no quantum numbers are exchanged between the interacting particles. As the energy of the collision increases (more inelastic channels become available) diffraction dominates the reaction process. The most general diffractive reaction can be represented by

$$AB \to A^* B^* \tag{1.1}$$

[2]A comprehensive and up-to-date overview of high-energy particle diffraction can be found in [3].

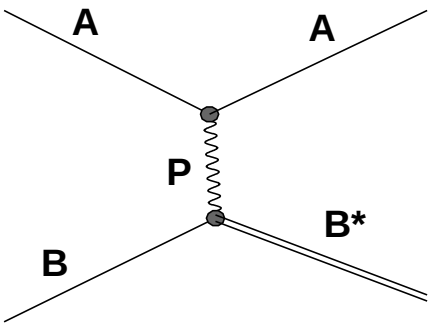

Figure 1.1. Single diffractive process. $AB \rightarrow AB^*$ through exchange of a Pomeron.

where A^* and B^* have the same quantum numbers as A and B respectively. This process is said to be dominated by the exchange of a Pomeron or equivalently the exchange of vacuum quantum numbers [4]. Fig. 1.1 shows the particular case of single diffraction, where A remains intact after the collision.

After its discovery in the 1960's diffractive physics was studied extensively until the quark model gained popularity. A revival of theoretical and experimental interest in diffraction in the early 1990's was spurred on by Bjorken's [5] observacion that large rapidity gaps were a signature of diffractive events, and Ingelman-Schlein's [6] proposal that diffraction could be used as a tool to understand and develop Quantum Chromodynamics (QCD), the theory of strong interactions. Jet production in $p\bar{p}$ collisions with a leading proton in the final state—a proton carrying a large fraction of the initial proton's momentum—was observed for the first time at the UA8 experiment at CERN [7]. Using electron-proton collisions, hard diffraction was observed at HERA (Hadron-Electron Ring Accelerator). In this case it was characterized by large rapidity gaps between the remaining proton and the products of the hadronization of the photon mediating the interaction (see Fig. 1.2). Events with large rapidity gaps between two jets were discovered by CDF and D0 at the Tevatron [8].

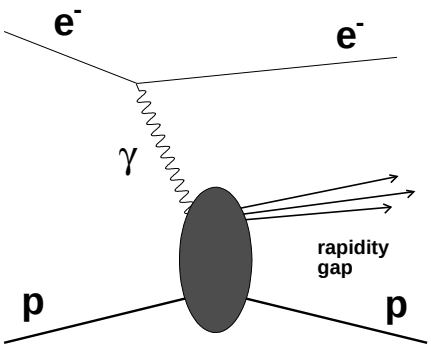

Figure 1.2. Hard Diffraction at HERA.

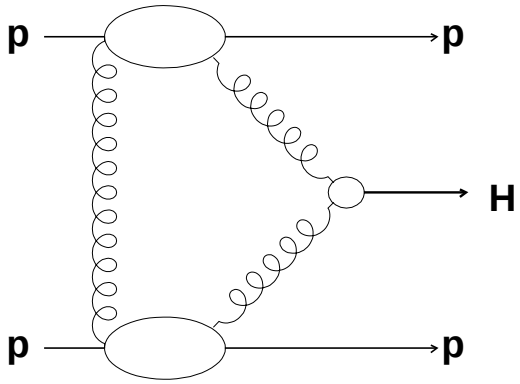

Figure 1.3. Central exclusive production of Higgs.

Despite these advances, diffraction has not been typically thought of as an area of study within which physics beyond the Standard Model might appear. The possibility of using diffractive interactions as a search tool for new physics was proposed in the early 1990's [9], and this idea has been developed recently into an experimental proposal [10]. The idea is that a diffractive process called central exclusive production (also known as double pomeron exchange) may provide a particularly low background method of searching for and identifying the nature of new particles at the LHC. The central exclusive production process, shown in Fig. 1.3 for the case of Higgs production, is the process

$$pp \rightarrow p + X + p\,,$$

where + denotes the rapidity gap between the outgoing (forward) protons—which lost a small fraction of their momentum—and the decay products of the central system X. The protons correspond to A and B in Eq.(1.1) and the central system is a product of the collision of two of the pomerons that mediate the diffractive interaction of the protons. If forward protons remain intact then the central system is produced in a spin-0 CP even state, allowing a determination of the quantum numbers of any observed resonance. [10]. This is in contrast to gluon-gluon collision processes which bring no conserved quantum numbers into the reaction except for the basic color quantum numbers of the strong interactions [1]. It has been shown that, subject to the installation of suitable forward proton detectors providing excellent mass resolution on the central system, signal to background ratios greater than unity are predicted for Standard Model Higgs central exclusive production [11] and for the lightest Higgs boson in certain regions of the MSSM[3] parameter space [12].

1.3 FP420

The mass acceptance and resolution of suitable forward proton detectors is an important issue which depends primarily on the LHC beam optics, the distance of the detectors from the interaction point, how close is the active region of the detectors to the beam and how accurately the position of the detectors relative to the beam can be known. FP420 works as a magnetic spectrometer, measuring the momentum loss of the outgoing protons which corresponds to the mass of the central system in central exclusive production. At a distance of 420 meters from the interaction point, protons with a 60 GeV [4] momentum loss deviate from the beam by at least 10σ.[5] This distance gives the name to the FP420 collaboration project, an international collaboration with members from 10 countries and 29 institutions whose aim is to assess the feasibility of installing

[3]MSSM is the minimal supersymmetric extension of the Standard Model.

[4]60GeV$\sim m_H/2$, half the mass of a light Higgs.

[5]σ is the standard deviation of the beam width, in this case its value in the 420m region.

proton tagging detectors at 420m from the interaction points of the ATLAS and/or CMS experiments at the LHC.

Due to the low mass of the central system (Higgs) the momentum fraction lost by the proton, denoted by ξ, has values in the range of 10^{-3} to 10^{-2}. A typical technique to detect scattered protons at small angles and with small relative momentum loss is by using Roman Pot detectors [13]. An issue facing FP420 is the unsuitability of the connection cryostat, currently at the 420m section of the LHC, for the addition of proton detectors. The connection cryostat, which is part of the accelerator design, maintains a series of superconducting bus-bars, and the beam pipes themselves, at a temperature of 1.7K. The upgrade proposed by FP420 replaces this connection cryostat with a modified design allowing the insertion of proton taggers called a "Hamburg Pipe" which enables proton detection at small angles [14]. In this design, the stations are rigidly fixed to the beam pipe and the entire structure will then be moved to place the detectors closer to the beam line itself. The position of each station with respect to the beam will be measured using beam positioning monitors and in situ callibration. With this design the forward proton detectors can have an acceptance in ξ down to 10^{-3}. The detectors could then be used to determine the proton momenta and angle by measuring, with respect to the beam axis, the horizontal displacement at the upstream and downstream locations. A variation of $\Delta\xi = 5 \times 10^{-4}$ produces a $80\,\mu$m difference in the horizontal displacement of a diffractively scattered proton[11],[15]. State-of-the-art silicon microstrip detectors that can measure this displacement with a precision of the order of 5 μm are being developed. This detectors use 3D silicon for edgeless tracking to maximize near beam acceptance and are suitable for extreme radiation environments [16].

1.4 Fast timing

As part of the proton tagging detectors, time-of-flight (TOF) counters can be used to dramatically decrease background to central exclusive events with a central system

and forward protons, by using timing to confirm that the protons originated from the same vertex as the central system. The goal of this thesis is to present the R&D efforts in the development of this time-of-flight counters, a work carried out by my advisor Andrew Brandt and myself through the course of the last two years in collaboration with the University of Alberta, Fermilab, and UC Louvain. The QUARTIC (Quartz Timing Counter) time-of-flight detector is an array of fused silica (quartz-like) bars aligned at an angle with the beam. The protons pass through the bars and emit Cherenkov photons which are detected by a micro-channel plate photomultiplier tube at the end of the bars. The QUARTIC detector is being developed mainly by UTA, Alberta, and Fermilab. A complementary fast timing solution named GasTOF (gas time-of-flight) is being pursued by UC Louvain. The QUARTIC and GasTOF detectors have complementary features and both of them are planned to be installed as part of the FP420 stations. Utilizing both technologies a $\lesssim$10ps time measurement is expected.

In this work, I present the results of the first stage of R&D efforts for the QUARTIC detector. Preliminary studies and results of simulations of several detector geometries are summarized. The experimental tools and analysis framework developed to allow testing of the first two prototypes in the Meson Test Beam Facility at Fermilab are described. Finally the results obtained in August 2006 and March 2007 runs at the Test Beam are presented.

CHAPTER 2

CENTRAL EXCLUSIVE HIGGS: BACKGROUND REJECTION

2.1 Central exclusive Higgs boson production

In this section a more detailed review of the process

$$pp \to p + (H \to b\bar{b}) + p$$

is presented, where the Higgs boson decays via the $b\bar{b}$ channel. This is the dominant decay channel for a light Higgs boson predicted in the intense coupling region of the MSSM ($m_H \sim 120\text{GeV}$) [17]. The Higgs predicted by the Standard Model ($140\text{GeV} \leq m_H \leq 200\text{GeV}$) is more likely to be observed via the WW^* channel [18]. The contents of this section follow closely the discussion in [11]. Central exclusive production is attractive because the mass of the Higgs boson can be measured to high accuracy if the forward outgoing protons are tagged, $M_H = \Delta M$ where ΔM is the missing mass. The $b\bar{b}$ channel also allows an independent measurement of the Higgs mass via the $H \to b\bar{b}$ decay in the central detector, $M_H = M_{b\bar{b}}$. The existence of matching peaks, centered about $\Delta M = M_{b\bar{b}}$ is a unique feature of the central exclusive production process. This sets it apart from the central inclusive process

$$pp \to M_1 + H + M_2$$

where the outgoing protons dissociate diffractively into M_1 and M_2 (rapidity gaps but without forward protons to tag); and also from the central inelastic production process

$$pp \to p + (M \to HX) + p$$

where there are also rapidity gaps and forward protons but $\Delta M > M_H$.

The leading order diffractive backgrounds to $pp \to p + (H \to b\bar{b}) + p$ include the central exclusive production of a gg pair in which the outgoing gluons are misidentified as b and $\bar{b}$ jets. The central exclusive production of $b\bar{b}$, which one might think to be the main background, is highly suppressed by a $J_z = 0$ selection rule.

To select the central diffractive events requires a sufficient suppression of the huge non-diffractive event rates. This is achieved by, at the Level 1 trigger, selecting events with a pair of back to back jets in the central detector with $|\eta| < 2.5$ with $E_T > 40$ GeV. The information from the FP420 proton taggers will arrive at the central trigger processor 3 μs after the interaction occurred, which is too late for it to be included in a Level 1 decision.

The cross section of the central exclusive production of the Higgs is [11]

$$\sigma(pp \to p + H + p) \approx 3\text{fb}.$$

A calculation of the signal to background ratio for the $pp \to p + (H \to b\bar{b}) + p$ process is presented in [11]. This calculation takes into account the efficiency of b jet tagging, which is correlated with the probability to misidentify a gluon as a b jet. Accounting also for the $\frac{2}{3}$ branching ratio for $H \to b\bar{b}$ reduces the original

$$(\sigma = 3\,\text{fb}) \times (\mathcal{L} = 30\text{fb}^{-1}) = 90 \text{ Higgs events}$$

to a signal of 11 $H \to b\bar{b}$ events[1]. The signal to background ratio depends on the resolution of the missing mass and is given by

$$\frac{S}{B} = 3\left(\frac{1\text{GeV}}{\delta(\Delta M)}\right)$$

[1]An integrated luminosity of 10fb^{-1} per year is expected in the first years of LHC running, 30fb^{-1} would be three years of data. The luminosity is expected to increase after the first years so 30fb^{-1} would require a much shorter running period.

Thus for $\Delta M \approx 2\,\mathrm{GeV}$ there correspond a total of about 8 background events to the 11 signal events in $30\mathrm{fb}^{-1}$. The signal to background ratio is currently being studied in more detail using Monte Carlo data by Arnab Pal at UTA. He includes the ATLFast simulation of the central detector and uses a Gaussian smearing to simulate the FP420 missing mass resolution. His study allows an optimization of the cuts used to select the central exclusive $b\bar{b}$ jets.

2.2 Pile-up background

Besides the background from other physics processes, discussed in the last section, another potentially more important source of background is from pile-up, which refers to the multiple interactions per bunch crossing and is a price to pay for the unprecedented high luminosities to be expected at the LHC. Pile-up events that combine collisions with forward protons and collisions with a central system can fake the signatures that FP420 is pursuing. Processes that result in forward protons include single diffraction (see Fig.1.1) and double pomeron exchange (i.e. central exclusive production). Also certain non-diffractive events can have leading protons with fractional momentum loss small enough to be near the beam. These three are contributions to the event pile-up and contribute a major background source for the selection of diffractive events when they occur in the same bunch crossing (pile-up) as inclusive dijet events that have no forward protons. This type of background can be reduced, in the case of central exclusive production, by kinematic constraints matching the central system and the forward protons.

Kinematic constrains alone do not appear to be sufficient at high luminosity, motivating the use of fast timing counters that can determine whether the protons seen in the FP420 tracking stations come from the same vertex as the hard scatter seen in the central detector. This is the motivation of this document and we see that the addition of suitable timing detectors decreases pile-up background.

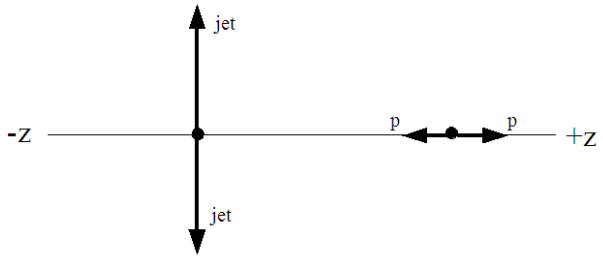

Figure 2.1. Pile-up background [X][pp].

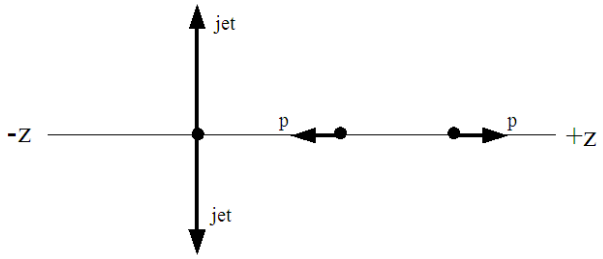

Figure 2.2. Pile-up background [X][p][p].

2.2.1 Possible pile-up topologies

The signature of the central exclusive signal is two jets in the central detectors with forward protons in the upstream and downstream FP420 stations. There are three ways that this can be faked by pile up background. The first (see Fig. 2.1) is back to back jets in the central detector, overlapped with two forward protons originating from the same diffractive vertex, [X][pp]. The second (see Fig. 2.2) is back to back jets in the central detector, overlapped with two forward protons, each of the protons coming from a different diffractive vertex, [X][p][p]. The third case (see Fig. 2.3) is back to back jets and one forward proton, from a diffractive vertex, and a second forward proton coming from a different diffractive vertex, [pX][p].

The way to estimate the cross section for each of the event topologies is the following. One starts with the non-diffractive (i.e. QCD) cross section for a two jet event and

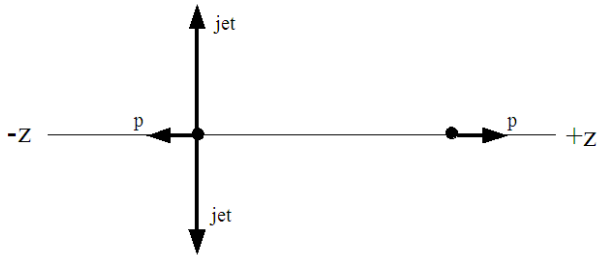

Figure 2.3. Pile-up background [pX][p].

then scales it down by the appropriate factors for a single bunch crossing. For instance, in [X][pp] we have:

$$\sigma_{[X][pp]} = N_{\mathcal{L}}\, P_e\, \sigma, \tag{2.1}$$

where $\sigma \sim 500$ fb is the non-diffractive cross section, $N_{\mathcal{L}}$ is the number of pile-up events per crossing (dependent on the instantaneous luminosity), and P_e is the probability of a pile up having two protons in the acceptance of the FP420 stations. When forward protons are accepted in the FP420 stations there is an amount of missing mass that will show up in the central detector in addition to the QCD jets. Some fraction of these events may be rejected through kinematic constraints including $\Delta M \neq M_{b\bar{b}}$ or, depending on the secondary vertexing capabilities of the central detector, both the QCD and diffractive vertices may be identified and differentiated with the use of FP420 time-of-flight vertexing. In [X][p][p] we have to include the number of ways to select two pile-up events and a factor of 1/2 that ensures the two protons go in opposite directions:

$$\sigma_{[X][p][p]} = \frac{1}{2}\binom{N_{\mathcal{L}}}{2} P_i^2\, \sigma = \frac{N_{\mathcal{L}}(N_{\mathcal{L}}-1)}{4}\, P_i^2\, \sigma, \tag{2.2}$$

where P_i is the probability of the pile-up event being single diffractive and causing a hit in the FP420 station. The value of P_i has been estimated using a Monte Carlo simulation to be $P_i = 0.012$, [17]. The cross section of [X][p][p] is expected to be the most significant pile-up background. [pX][p] is different because we have to start with the cross section

for a single diffractive event with two jets. This case is expected to be the least relevant since the hard diffractive cross section is much smaller than the QCD cross section for two jet events .

$$\sigma_{[pX][p]} = \frac{1}{2} N_{\mathcal{L}}\, P_i\, \sigma_{\text{single diff}}. \tag{2.3}$$

The factor of two ensures the opposite directions of the outgoing protons.

2.3 Background rejection potential of a fast TOF counter

A fast time-of-flight counter can be used to reject most of the pile-up events in the three cases above by measuring the time-of-flight difference of the two forward protons in the upstream and downstream FP420 stations. Referring to the stations as right (R) and left (L), measurements of $t_{\rm R}$ and $t_{\rm L}$ yield an interaction vertex associated with the forward protons, $z_{\rm FP}$. The uncertainty in the measurement of $z_{\rm FP}$ is related to the uncertainty in the measurement of the time-of-flight, δt:

$$z_{\rm FP} = c\,\frac{t_{\rm L} - t_{\rm R}}{2} \tag{2.4}$$

$$\begin{aligned} \delta z_{\rm FP} &= \sqrt{\left(\frac{c}{2}\delta t_{\rm L}\right)^2 + \left(\frac{c}{2}\delta t_{\rm R}\right)^2} \\ &= \frac{c}{\sqrt{2}}\delta t, \end{aligned} \tag{2.5}$$

where $\delta t_{\rm L} = \delta t_{\rm R} = \delta t$. With a sufficiently fast TOF with a resolution of 10 ps, the interaction vertex can be determined to an accuracy of $\delta z_{\rm FP} = 2.1$ mm. The jets measured by the central detector (which triggered recording of the event at Level 1) are associated with an interaction vertex determined by the central tracker, $z_{\rm CT}$, with an uncertainty $\approx$50 μm [19]. In the case of pile-up if

$$|z_{\rm CT} - z_{\rm FP}| \leq \alpha_{cut}\sqrt{(\delta z_{\rm FP})^2 + (\delta z_{\rm CT})^2} \approx \alpha_{cut}\delta z_{\rm FP} \tag{2.6}$$

then we are erroneously led to believe that this is a central exclusive production event. Considering this, I examine the background rejection potential of timing the forward protons. I show the results for $\alpha_{cut} = 1$ and $\alpha_{cut} = 1.5$.

At the LHC, the luminous region is assumed to have a Gaussian profile in z, and the probability of an interaction occurring in the vicinity of z is given by

$$P(z)\mathrm{d}z = \frac{1}{\sigma_{\mathrm{LR}}\sqrt{2\pi}} \exp\left[-\frac{z^2}{2\sigma_{\mathrm{LR}}^2}\right] \mathrm{d}z \tag{2.7}$$

where σ_{LR} is the standard deviation of the luminous region, $\sigma_{\mathrm{LR}} = \sqrt{2}\sigma_z \approx 5.6$cm [19]. The interactions in the bunch crossing are also distributed in time. The distribution in time is simply $P(ct)$, with P as defined above, if we set $t = 0$ at the point of total bunch overlap.

The TOF counter measurement of the $t_L - t_R$ difference will always yield a vertex even if the left and right protons originated at different interaction points. A fake vertex is obtained in the [X][p][p] and [pX][p] topologies but this does not affect the rejection factors as will be shown below.

2.3.1 [X][pp]

When the left and right protons come from a single interaction as in [pp] the distribution of TOF reconstructed vertexes is $P(z)$. We start by calculating the probability density that, given two interaction vertices (z_1, z_2) in the same bunch crossing, the difference between them, $z_1 - z_2$, is equal to s. This probability density is labeled $F(s)$.

$$\begin{aligned} F(s) &= \int_{-\infty}^{\infty} P(z)P(z-s)\mathrm{d}z \\ &= \frac{1}{2\sigma_{\mathrm{LR}}\sqrt{\pi}} \exp\left[-\frac{s^2}{4\sigma_{\mathrm{LR}}^2}\right]. \end{aligned} \tag{2.8}$$

One of the vertices, say z_1 is the TOF vertex, and the other is the central detector vertex. If the distance between the two interaction vertices is less than $\alpha_{cut}\delta z_{\mathrm{FP}}$, as in Eq.(2.6),

we cannot reject it as pile-up background. The percentage of [X][pp] pile-up events for which this happens is given by

$$\int_{-\alpha_{cut}\delta z_{\rm FP}}^{\alpha_{cut}\delta z_{\rm FP}} F(s)\mathrm{d}s. \tag{2.9}$$

This depends on $\delta z_{\rm FP}$, which is directly proportional to the time resolution of the fast timing counters δt. Table 2.1 shows the rejection factor for [X][pp] pile-up events, defined as the number of pile events before time-of-flight rejection cuts divided by the remaining number of events after cuts.

2.3.2 [X][p][p]

In this case we have three interaction vertices and the two forward protons come from distinct vertices. When a measurement of $t_{\rm L}$ and $t_{\rm R}$ is performed by the FP420 time-of-flight counters, the algorithm assumes that times are from a common vertex (z and time) and thus produces a fake vertex at a certain z location. If the two single diffractive interactions occurred at s_1, t_1 and s_2, t_2, the fake vertex is given by

$$z_{\rm fake} = \frac{s_1 + s_2}{2} - \frac{c(t_1 - t_2)}{2}. \tag{2.10}$$

The inequality (2.6) can be written as

$$\begin{aligned} &|z_{\rm CT} - z_{\rm fake}| \leq \alpha_{cut}\delta z_{\rm FP} \\ \Rightarrow\ &2(z_{\rm CT} - \alpha_{cut}\delta z_{\rm FP}) \leq s_1 + s_2 - ct_1 + ct_2 \leq 2(z_{\rm CT} + \alpha_{cut}\delta z_{\rm FP}). \end{aligned} \tag{2.11}$$

When this inequality is satisfied this pile-up event will not be rejected. The distribution of $s_1 + s_2 - (ct_1 - ct_2) \equiv l$ is given by

$$G(l) = \int_{-\infty}^{\infty} \left[\int_{-\infty}^{\infty} P(s_1)P(x - s_1)\mathrm{d}s_1\right] \left[\int_{-\infty}^{\infty} P(ct_1)P(ct_1 - x + l)\mathrm{d}ct_1\right] \mathrm{d}x \tag{2.12}$$

$$= \int_{-\infty}^{\infty} F(x)F(x - l)\mathrm{d}x. \tag{2.13}$$

Table 2.1. Rejection factor, cases [X][pp] and [X][p][p]

δt	Rejection Factor	
	$\alpha_{cut} = 1$	$\alpha_{cut} = 1.5$
10ps	47	32
20ps	24	16
30ps	16	11
40ps	12	8
80ps	6	4
100ps	5	3

Then the percentage of pile-up not rejected, for fixed z_{CT}, is given by

$$\int_{2(z_{\mathrm{CT}}-\alpha_{cut}\delta z_{\mathrm{FP}})}^{2(z_{\mathrm{CT}}+\alpha_{cut}\delta z_{\mathrm{FP}})} G(l)\mathrm{d}l. \tag{2.14}$$

Integrating over the distribution of z_{CT}, the percentage of pile-up not rejected is

$$\int_{-2\alpha_{cut}\delta z_{\mathrm{FP}}}^{2\alpha_{cut}\delta z_{\mathrm{FP}}} \int_{-\infty}^{\infty} P(z_{\mathrm{CT}})G(u+2z_{\mathrm{CT}})\mathrm{d}z_{\mathrm{CT}}\mathrm{d}u. \tag{2.15}$$

By coincidence, we have that

$$\int_{-2\alpha_{cut}\delta z_{\mathrm{FP}}}^{2\alpha_{cut}\delta z_{\mathrm{FP}}} \int_{-\infty}^{\infty} P(z_{\mathrm{CT}})G(u+2z_{\mathrm{CT}})\mathrm{d}z_{\mathrm{CT}}\mathrm{d}u = \int_{-\alpha_{cut}\delta z_{\mathrm{FP}}}^{\alpha_{cut}\delta z_{\mathrm{FP}}} F(v)\mathrm{d}v,$$

and the results for various timing resolutions are the same as in the first topology. Table 2.1 shows the results.

2.3.3 [pX][p]

As in [X][p][p] we have the reconstruction of a fake vertex. $z_{\mathrm{FP}} = (s_1 + s_2 - ct_1 + ct_2)/2$ and in this case $s_1 = z_{\mathrm{CT}}$. Inequality (2.6) leads to

$$z_{\mathrm{CT}} - 2\alpha_{cut}\delta z_{\mathrm{FP}} \leq s_2 - ct_1 + ct_2 \leq z_{\mathrm{CT}} + 2\alpha_{cut}\delta z_{\mathrm{FP}} \tag{2.16}$$

Table 2.2. Rejection factor, [pX][p]

δt	Rejection Factor	
	$\alpha_{cut} = 1$	$\alpha_{cut} = 1.5$
10ps	33	22
20ps	17	11
30ps	11	8
40ps	9	6
80ps	4	3
100ps	3.4	2

The distribution of $s_2 - ct_1 + ct_2 \equiv k$ is

$$H(k) = \int_{-\infty}^{\infty} P(s_2 \left[\int_{-\infty}^{\infty} P(ct_1) P(ct_1 - s_2 + k) \mathrm{d}ct_1 \right] \mathrm{d}s_2 \tag{2.17}$$

$$= \int_{-\infty}^{\infty} P(s_2) F(s_2 - k) \mathrm{d}s_2. \tag{2.18}$$

For fixed z_{CT},

$$\int_{z_{\mathrm{CT}} - 2\alpha_{cut}\delta z_{\mathrm{FP}}}^{z_{\mathrm{CT}} + 2\alpha_{cut}\delta z_{\mathrm{FP}}} H(k) \mathrm{d}k = \int_{-2\delta z_{\mathrm{FP}}}^{2\delta z_{\mathrm{FP}}} H(u + z_{\mathrm{CT}}) \mathrm{d}u \tag{2.19}$$

and integrating over z_{CT} we get:

$$\int_{-2\alpha_{cut}\delta z_{\mathrm{FP}}}^{2\alpha_{cut}\delta z_{\mathrm{FP}}} \int_{-\infty}^{\infty} P(z_{\mathrm{CT}}) H(u + z_{\mathrm{CT}}) \mathrm{d}z_{\mathrm{CT}} \mathrm{d}u \tag{2.20}$$

Table 2.2 shows the rejection factor. Due to the correlation between the two vertices, the rejection factor is smaller in this case.

2.4 Background cross-section

The rejection factor of fast timing can then be included in the pile-up background cross sections, Eqs. (2.1, 2.2, 2.3). The cross sections are scaled by the inverse of the

Table 2.3. $N_{\mathcal{L}}$ and the [X][p][p] pile-up cross section for different instantaneous luminosities.

lumi ($\mathrm{cm}^{-2}\mathrm{s}^{-1}$)	$\langle N_{\mathcal{L}} \rangle$	$\langle \sigma_{[X][p][p]} \rangle_{\mathcal{L}}$; α_{cut}=1	α_{cut}=1.5
1×10^{33}	3.5	4.7×10^{-3} fb	7.0×10^{-3} fb
2×10^{33}	7.0	1.8×10^{-2} fb	2.8×10^{-2} fb
5×10^{33}	17.5	1.1×10^{-1} fb	1.7×10^{-1} fb
7×10^{33}	25.0	2.4×10^{-1} fb	3.6×10^{-1} fb
1×10^{34}	35.0	4.7×10^{-1} fb	7.0×10^{-1} fb

rejection factor. In the optimistic scenario of a 10 ps resolution time measurement and with α_{cut}=1.5:

$$\sigma_{[X][pp]} = (0.032) \times N_{\mathcal{L}}\, P_e\, \sigma, \tag{2.21}$$

$$\sigma_{[X][p][p]} = (0.032) \times \frac{N_{\mathcal{L}}(N_{\mathcal{L}} - 1)}{4}\, P_i^2\, \sigma, \tag{2.22}$$

$$\sigma_{[pX][p]} = (0.045) \times \frac{N_{\mathcal{L}}}{2}\, P_i\, \sigma_{\text{single diff}} \tag{2.23}$$

and the background cross sections are dramatically reduced. The background rejection factors are luminosity independent to the extent that they assume only one forward proton hits an FP420 station per bunch crossing. At high luminosities there are two ways the pile-up background can scale. First the number of pile-up events per crossing, $N_{\mathcal{L}}$, would increase with luminosity and second higher order pile-up topologies will be present with more than three interaction vertices and more than one forward proton in the acceptance region per bunch crossing. The first effect has been studied by Grothe [20] and the values of $N_{\mathcal{L}}$ as a function of luminosity are in Table. 2.3. Notice that the value obtained by Grothe is the expected value $\langle N_{\mathcal{L}} \rangle$ of the pile-up interactions per bunch crossing. If Poisson statistics are assumed the expected value of the pile-up background cross sections can be estimated as a function of luminosity as well, for example

$$\langle \sigma_{[X][p][p]} \rangle_{\mathcal{L}} = \sum_{k=0}^{\infty} \frac{e^{-\lambda}\lambda^k}{k!} \sigma_{[X][p][p]}(\mathcal{L})$$

in the [X][p][p] case, where $\lambda = \langle N_{\mathcal{L}} \rangle$. In the last column of Table 2.3 I show the pile-up background cross section for [X][p][p]. In the other two cases the statistics are trivial since the cross section is $\propto N_{\mathcal{L}}$, but currently there are no estimated values for P_e and $\sigma_{\text{single diff}}$ so I can't quote the exact cross section.

CHAPTER 3

TIME-OF-FLIGHT COUNTERS

3.1 Time-of-flight and its applications in High Energy Physics

A time-of-flight counter (TOF) is a particle detector that aims to accurately measure the time at which a particle is detected with respect to a reference time. Sometimes a reference clock with very low jitter compared to the time resolution of the TOF counter is provided as the reference time; but in the absence of an arbitrarily precise reference a time-of-flight measurement implies the measurement of a time difference. In the best case the time difference is obtained through two measurements using equally precise detectors. If one detector is much better than the other, the resolution of the time difference will be dominated by the worse detector. The measurement of a time difference along a fixed length or for two points on a particle's track allows determination of the velocity of the particle. Since the momentum of a track can be observed as the curvature of the track on a magnetic field, the TOF measurement yields the mass associated with the track and is an effective form of particle identification in collider experiments.

In the CDF experiment at the Tevatron in Fermilab, a TOF system complements particle identification done through energy loss (the $\mathrm{d}E/\mathrm{d}x$ method) [21]. TOF is the simplest and most cost effective way to provide the ability to identify B-hadron decay products over a good fraction of their momentum spectrum. The separation between kaons and pions is critical for reconstructing B-decays, allowing the determination of the b-quark flavor, which in turn is crucial for CP violation studies. All other experiments dedicated to the study of B-physics (BaBar at SLAC, BELLE at KEK) employ some type of particle identification for this reason. Besides TOF and $\mathrm{d}E/\mathrm{d}x$, another technique

is Cherenkov angle measurement which will be discussed further later in this chapter. Particle identification is also useful in test beam experiments. Frequently test beams are composed of a mixture of protons, pions and other particles. A TOF counter in the beam would be able to identify the beam particles, allowing a selection of the type of beam particle desired by the individual experiment.

A TOF counter is made up of three basic components, the radiator (also loosely referred to as the detector), the photo-detector and the readout electronics. All of this three components contribute independently to the time resolution of the counter. The radiator is a material with a certain geometry that emits light when a particle passes through it. The photo-detector is then used to detect and amplify this light into an electronic signal which is processed by the readout electronics. The light that arrives from the radiator to the photodetector is distributed in time and this distribution corresponds to the detector component of the counter resolution, σ_{det}. There is also a jitter inherent to the transit time of amplification of the light by the photodetector, this is the photodetector resolution component σ_{pd}. Furthermore the readout electronics have to digitize the time of pulses with randomly varying amplitudes and this introduces the electronics resolution component σ_{elec}. The three independent contributions add in quadrature to give the intrinsic time resolution of the TOF counter,

$$\sigma_{\text{counter}} = \sqrt{\sigma_{\text{det}}^2 + \sigma_{\text{pd}}^2 + \sigma_{\text{elec}}^2}. \tag{3.1}$$

The purpose of this chapter is to introduce the principal characteristics of the three TOF counter components to contextualize the discussion of the QUARTIC and GasTOF designs in Chapter 4.

3.2 TOF detectors and Cherenkov radiation

The detectors most generally used for TOF counters are scintillators[1]. Scintillators can have a time resolution of $\frac{100}{n}$ps, where n is the index of refraction of the scintillating material ($\sim$1.5). A charged particle traversing a scintillator leaves behind it a wake of excited molecules. Certain types of molecules will release a small fraction of this energy as optical photons. The plastic scintillators used in high-energy physics are made with a base plastic scintillator which emits in the ultraviolet and have also mixtures of fluorescent compounds (fluors) which act as wave shifters absorbing this UV light and re-emitting closer to the visible wavelengths. Plastic scintillators are labeled as binary or ternary depending on how many fluors are involved in the ladder that shifts the wavelengths to the visible region. The typical yields are about 1 photon per 100eV of energy deposit. A 1 cm-thick scintillator traversed by a minimum ionizing particle will therefore yield $\approx 2 \times 10^4$ photons. The resulting signal will depend on the collection and transport efficiency of the optical package and the quantum efficiency of the photodetector [22]. With such a high photon yield and good time response, scintillators are very reliable particle detectors. The low cost and the ease of fabrication into desired shapes has made plastic scintillators a common detector component.

As was discussed in Chapter 2, a time resolution of $\sim$10 ps is necessary to dramatically reduce pile-up background. Although scintillators are a versatile detector, the timescales of the emission and absorption processes that yield visible light lend to a detector time resolution on the order of $\gtrsim$100ps. The random (spontaneous) nature of the emitted light in a scintillator does not allow a geometrical design that guides the light to the photo-detector without considerable spread in time. Cherenkov detectors are an al-

[1] A detailed account of organic and inorganic scintillators and their properties is found in [22]

ternative to scintillation detectors to better the time resolution. Cherenkov radiation[2] is emitted when a charged particle moving in a medium has a velocity exceeding the phase velocity of light in that medium. The charged particle polarizes the atoms along its trajectory creating time dependent dipoles. If the velocity of the particle v is $< c/n$ (n being the index of refraction) the dipole distribution is symmetric around the particle position (front and back) and the sum of all dipoles vanishes. If $v > c/n$ the distribution is asymmetric and the total time dependent dipole does not vanish and thus radiates [23, 24]. The timescale of the radiation of Cherenkov light is essentially instantaneous since there is no excitation and de-excitation cascade as in scintillators, but rather time-changing dipoles induced in the immediate vicinity of the charged particle. Cherenkov radiators are ideal for time-of-flight measurements because of the promptness of the light emitted. As a drawback, Cherenkov radiation is a weak source of photons and for this reason, light collection and detection must be as efficient as possible. The process is nondestructive since it takes away a negligible fraction of the incident particle's energy.

The angle θ_c at which the radiation is emitted relative to the particle's trajectory is given by

$$\cos\theta_c = \frac{1}{n\beta} \tag{3.2}$$

where, n is the index of refraction and the velocity of the particle is $v = \beta c$, see Figs. 3.1, 3.2. The wavefronts of the radiation emitted at this angle form the Cherenkov cone of emission. The emission angle can be interpreted qualitatively as a shock wave similar to the shock front in supersonic flight or the bow shock of a boat in water. The Cherenkov cone of emission is built up by the individual photons being emitted at the Cherenkov angle. This can be observed because the amount of light emitted is so weak that in some applications individual photons are detected [25]. Besides its use as a radia-

[2]Sections on Cherenkov radiation and Cherenkov detectors are found in the reviews of the Particle Data Group [22].

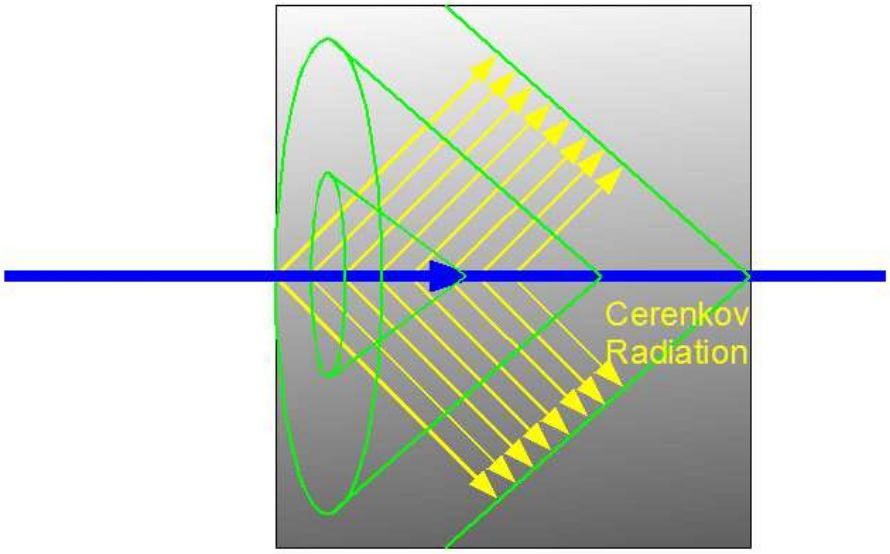

Figure 3.1. Illustration of the Cherenkov effect.

tion mechanism in timing counters, the Cherenkov effect can be used to identify particles by measuring the angle of emission. Threshold Cherenkov counters are used in beams of fixed momentum to flag particles above a certain mass. Detection of internally reflected Cherenkov light (DIRC) is used to identify particles in the BaBar experiment at SLAC [26].

The number of photons produced per unit path length of a particle with charge e and per unit wavelength interval of the photons is

$$\frac{d^2N}{d\lambda dx} = \frac{2\pi\alpha}{\lambda^2}\left(1 - \frac{1}{\beta^2 n^2(\lambda)}\right) \tag{3.3}$$

If the path length of the radiator is L, the number of photoelectrons detected in a given device is

$$N_{\text{p.e.}} = 2\pi\alpha L \int \epsilon(\lambda)\left(1 - \frac{1}{\beta^2 n^2(\lambda)}\right) \mathrm{d}\lambda, \tag{3.4}$$

where $\epsilon(\lambda)$ is the efficiency for collecting the Cherenkov light and transducing it in photoelectrons [22].

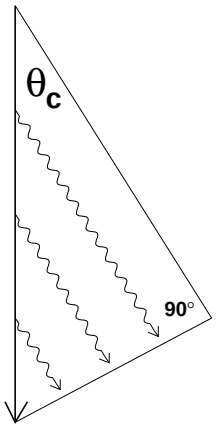

Figure 3.2. Cherenkov angle construction.

In choosing a material as a Cherenkov radiator one needs to consider factors such as material density, radiation length, transmission bandwidth, absorption length, chromatic dispersion, availability and cost. The geometry of the material is of importance not only because of the path length for the particle to radiate but because the material needs to be efficient in guiding the photons to the photo-detector.

3.3 Microchannel Plate Photomultiplier Tubes

The devices used as photo-detectors in TOF counters are generally photomultiplier tubes. They are very versatile and widely used in high-energy physics. Photomultiplier tubes have a photocathode material with a low work function and when a photon hits the cathode it liberates an electron, which is accelerated and guided by electric fields to hit a secondary-emission electrode. The multiplication process is repeated to generate a gain that depends on the applied high voltage and that is typically in the range of $10^5 - 10^6$ with pulse risetimes of the order of $\sim$1ns.

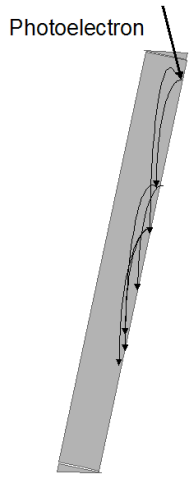

Figure 3.3. Microchannel as an electron multiplier.

Microchannel plate photomultiplier tubes [27] (MCP-PMT's) were initially developed as amplifiers for image intensification devices, but their sensitivity for charged particles and energetic photons has made them very useful in many fields including particle physics. A microchannel plate is an array of parallel miniature channels (10 μm -100 μm in diameter), each of which acts as an electron multiplier, see Fig. 3.3. Microchannel plates allow electron multiplication factors of $10^4 - 10^7$ with high time resolution ($\sim$20 ps) and spatial resolution limited only by the channel dimensions and spacings (12 μm diameter and 15 μm center-to-center spacings are typical values). The small time resolution is what makes MCP-PMT's suitable for the development of fast timing applications and has recently motivated several R&D efforts in this direction [28], [26], [29], including the work presented in this thesis. The microchannel plate is made of lead glass treated so that the walls of the channels are optimized for secondary electron emission. The front and rear of the plate are made into electrodes by the deposition of a metallic coating, the resistance between them being on the order of $10^9\,\Omega$.

An important parameter in MCP-PMT's is $\alpha = l/d$ the length to diameter ratio of the channels. For fixed α, as the high voltage increases so does the secondary electron

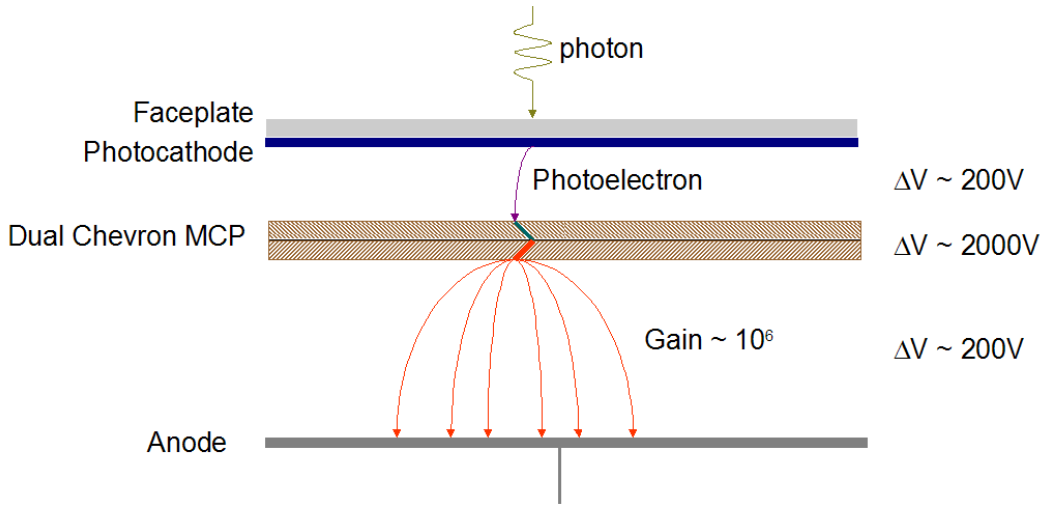

Figure 3.4. Illustration of the Burle 25 μm microchannel plate photomultiplier tube with a Chevron configuration.

yield since each collision occurs at a higher energy, but the number of collisions within a channel decreases. The interplay of these two effects leads to a maximum in the Gain vs. V characteristic. The gain also has an observed maximum in α and typical values are $40 < \alpha < 100$.

Ion feedback is the production of secondary electrons in the photocathode due to the probability of producing positive ions in the high charge density region at the output of the channel (where the amplified charge is mostly concentrated). The ions are produced by electron collisions with residual gas, and with gas molecules desorbed from the channel walls under electron bombardment. These positive ions can drift back to the photocathode and produce secondary electrons leading to performance instabilities. To prevent ion feedback and allow higher gains, the channel axes are biased at a small angle to the MCP surface and a secondary MCP separated by $50 - 150\,\mu$m from the primary MCP is used in what is called the Chevron configuration, see Fig.3.4.

Microchannel plates are widely used in night vision image intensifiers in conjunction with phosphor screens to yield the familiar green shaded night-vision images. Other

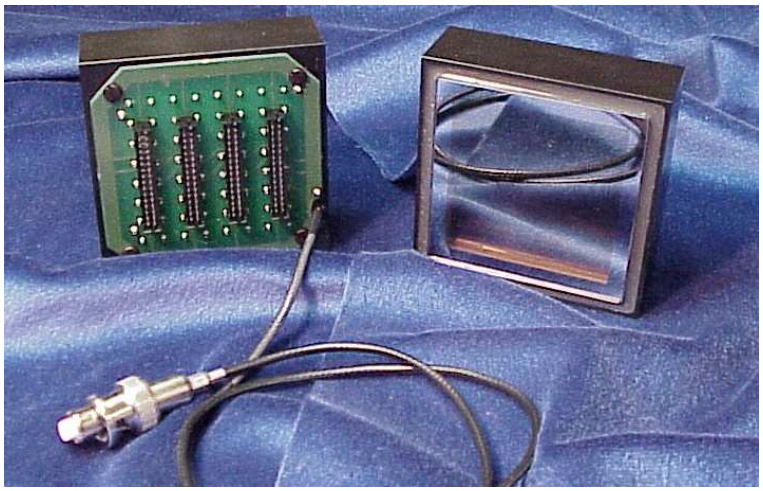

Figure 3.5. Planacon MCP-PMT.

applications are imaging in x-ray astronomy, medical x-ray imaging, and imaging in positron-emission tomography (PET). It is evident that the main feature of PMT's that makes it attractive for applications outside high energy physics is the position information, preserved by amplification within the microchannels. Applications in high energy physics benefit the most of the short length of the electron amplification region, i.e. the microchannel, which results in fast response, high timing resolution and operability in magnetic fields. The spatial resolution comes as and added feature that is also exploited in the design of the QUARTIC time-of-flight detector.

3.4 Timing with MCP-PMT's

In this section the fast timing experimental results with MCP-PMT's obtained by the Nagoya group [28], [30] and by SLAC [26] are summarized. The studies of this two groups used Burle and Hamamatsu PMT's. Burle/Photonis and Hamamatsu are the two main manufacturers of MCP-PMT's.

Burle Industries (now merged with Photonis) is the manufacturer of the Planacon MCP-PMT's, oriented towards high energy physics applications. The 25 μm pore

Table 3.1. Burle 85011-501 parameters

Photocathode type	Bialkali
Number of MCP's	2 - chevron
Total average gain at 2.4kV	$\sim 5 \times 10^5$
Max voltage	2.5kV
MCP channel diameter	25μm
α (=l/d for a channel)	40
MCP channel angle with perpendicular	12°
Photocathode to MCP1 gap	6.1mm
MCP1 to MCP2 gap	0mm
MCP2 to anode gap	5.2mm
Voltage divider ratio	1:10:1
Geometrical collection efficiency of the 1st MCP	60-65%
Fraction of late photoelectron arrivals	20%
Matrix of anode pixels	8×8

Planacon tube features a 2" square face with a large active area, see Fig. 3.5. The spectral response is in the visible 165-660 nm and it is available in several multi-anode 2×2, 8×8 and 32×32 pixel configurations. The parameters for the Burle 85011-501 are listed in Table 3.1. Burle has also produced 10 μm pore Planacons that have been tested by the SLAC group.

The Hamamatsu 3809U-50 is a single anode tube with 6 μm channel diameter. Its main target applications are outside high energy physics and for that reason it is a single anode tube and the active area is not very large compared to the body of the tube, see Fig.3.6 and Table 3.2.

3.4.1 SLAC results

The main goal of the SLAC R&D effort is to develop photon detectors for a fast focusing DIRC counter. The DIRC at the BaBar experiment currently provides particle identification through measurement of the Cherenkov angle by measuring x and y coordinates for each photon. A next generation detector will have not only position sensitivity

Figure 3.6. Hamamatsu MCP-PMT.

but also allow measurement of the TOF of each photon with a resolution better than 100 ps (resolution in the current system is 1.6 ns) which will allow a correction of the chromaticity error. Their application requires sub-100 ps single photon timing resolution on over 300 channels.

TTS, the transit time spread, is the fluctuation in transit time (specified as FWHM) with the incident light having a single photoelectron state. It is related to the single electron resolution, σ_{TTS}, which is the same quantity but specified as the standard deviation of a Gaussian fit, i.e. if the distribution is really Gaussian TTS $= 2.34\,\sigma_{\mathrm{TTS}}$. σ_{TTS} is the main quantity measured by SLAC for the Burle 25 μm and 10 μm multi-pad anode tubes. The setup to measure the σ_{TTS} consists of a PiLas (635 nm) laser diode which provides a timing resolution of 35 ps (FWHM) between an internal electrical trigger and a light pulse. The study was done on a single pad illuminated at its center and connected coaxially to a fast amplifier. All other pads in the anode were grounded. With this arrangement fixed, amplifiers of various bandwidths were varied. The amplifiers were

Table 3.2. Hamamatsu 3809U-50 parameters

Photocathode type	Multialkali
Number of MCP's	2 - chevron
Total average gain at 3.0kV	$\sim 2 \times 10^5$
Max voltage	3.6kV
MCP channel diameter	6μm
α	40
MCP channel angle with perpendicular	13°
Photocathode to MCP1 gap	2.1mm
MCP1 to MCP2 gap	0.03mm
MCP2 to anode gap	1.0mm
Voltage divider ratio	2:4:1
Matrix of anode pixels	Single anode

coupled to two types of constant fraction discriminators (CFD)[3] which provided a square NIM pulse to a LeCroy time to digital converter (TDC) with 24 ps/count.

Figure 3.7 shows the time resolution obtained for the Burle 25 μm tube. The tail in the distribution, fitted by a second Gaussian in blue, is caused by electrons that recoil off the MCP instead of going through a channel directly as they come from the photocathode. The SLAC group also measured $\sigma_{\rm TTS}$ for a 10 μm Burle tube and in this case they measured the timing resolution as a function of the number of photoelectrons, (Figs. 3.8 and 3.9). With more photoelectrons a better resolution is achieved, but after about 20 photoelectrons the resolution does not improve. In the range of 0-20 photoelectrons the improvement of the time resolution can be described as $\sigma_{\rm MCP} \sim \sigma_{\rm TTS}/\sqrt{N_{\rm p.e.}}$.

The group at SLAC also studied the spatial response across the faces of several 8×8-pixel Burle MCP-PMT's. The scanning measured the relative single photoelectron response of different pixels and different points within pixels. This efficiency measurement folds in several contributions, such as the photocathode quantum efficiency, photoelectron

[3]I will talk more about CFD's in Section 3.4.2 and Section 4.4.

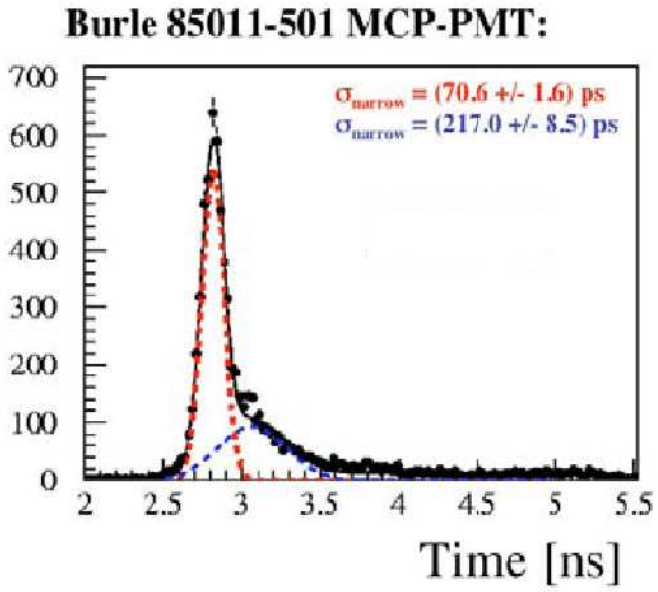

Figure 3.7. Timing resolution for Burle 25 μm, photocathode to MCP gap 6.1 mm. σ_{TTS}=70.6 ps.

[26].

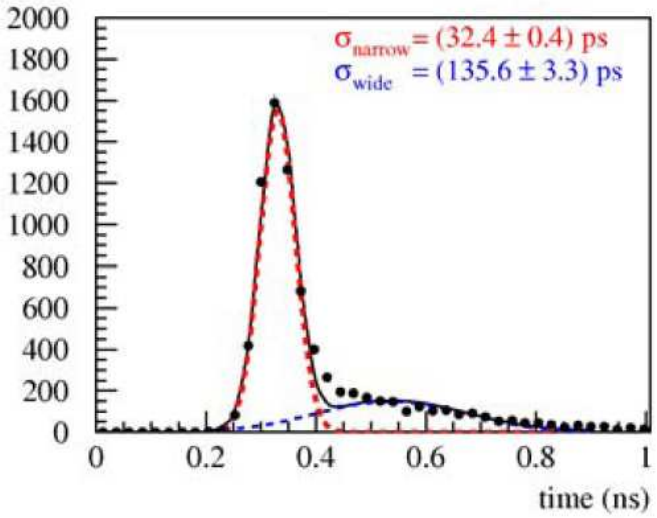

Figure 3.8. Timing resolution for Burle 10μm. σ_{TTS}=32.4ps.
[31].

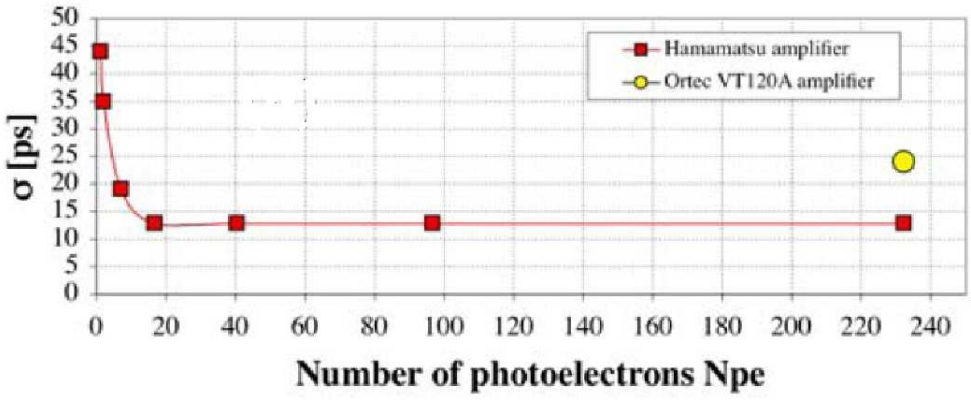

Figure 3.9. Timing resolution, Burle 10μm for varying number of photoelectrons. [31].

transmission losses and detection efficiency. The average value of the single electron efficiency for the Burle tube is 50-60% dropping to 30-50% at the edges of the tube.

3.4.2 Nagoya results

The goal of the Nagoya group is to develop a Cherenkov ring imaging detector for particle identification for a potential upgrade of the Belle detector. Their requirements are a transit time spread $\sigma_{\rm TTS}$ <100 ps in a magnetic field of $B = 1.5$T, conditions for which MCP-PMT's are the device of choice.

The Nagoya group irradiated the MCP-PMT's with single photons varying the magnetic field strength and angle. They used a Hamamatsu Picosec light-pulser with a wavelength of 405 nm and a pulse width of 34 ps with a jitter of less than 10 ps. They performed measurements on 4 different PMT's two of which were the Burle 25 μm and the Hamamatsu 6 μm, see Tables. 3.1 and 3.2. I omit here the results for the two other tubes. They measured the time of the PMT pulses using a preamplifier, a threshold discriminator and a TDC. They also measured the output charge with an analog to digital converter (ADC). Using the ADC distributions for single photon irradiation they

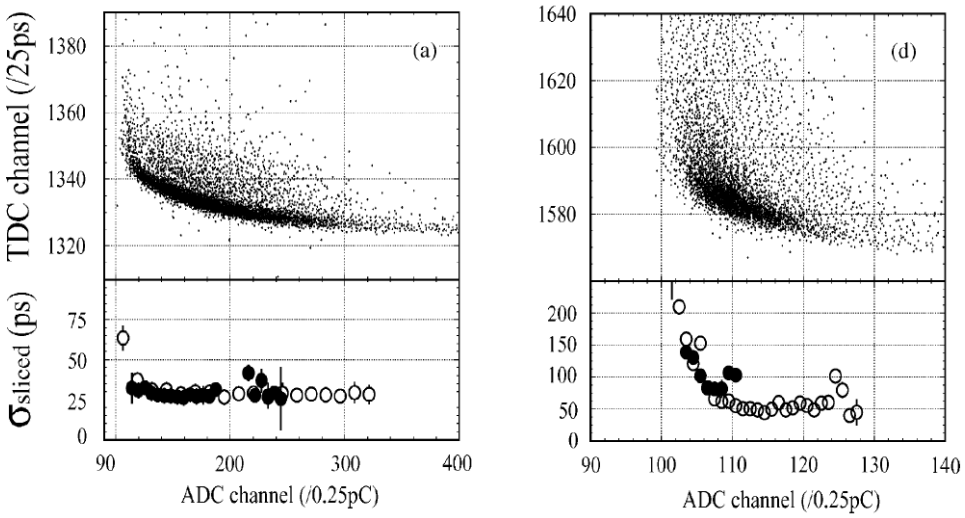

Figure 3.10. ADC vs. TDC scatter plot for single photon irradiation. Hamamatsu 6 μm (left) and Burle 25 μm (right).

[28].

were able to measure the effect of the magnetic field on the gain. An interesting plot is the ADC vs TDC scatter plot for single photon irradiation shown in Fig.3.10. This plot shows the timewalk caused by timing pulses of varying amplitudes. Even for single-photon irradiation there is a distribution in the output charge at the anode of the PMT, i.e. the amplitude of the pulses varies randomly. This is a problem when trying to time this pulses with a threshold discriminator, since some of them cross the threshold faster than others and this leads to a spread in time, see Fig. 3.11. For this reason, constant fraction[4] discriminators (CFD's) are generally used in fast timing applications. In the ADC vs. TDC plot the effect of the timewalk is measurable and a correction can be applied since the output charge of all the pulses is known. Also one could just select a slice of the charge output distribution and there would be no need to apply the correction. This is shown in the lower part of Fig. 3.10 where the time resolution using pulses with

[4]They receive this name because they time the pulses at a constant fraction of the risetime, which is pulse height independent as long as the rise time remains constant.

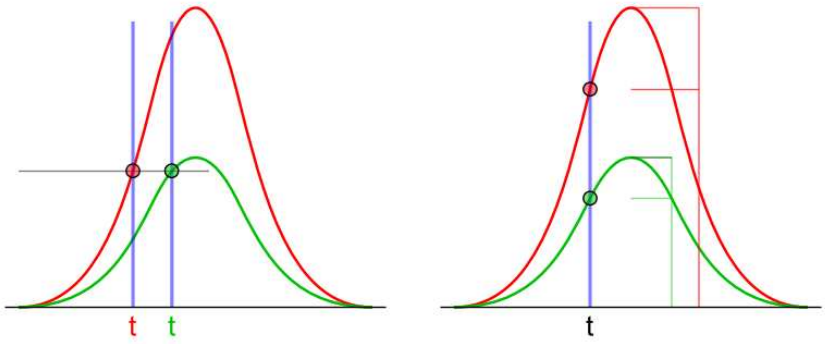

Figure 3.11. Comparisson of threshold triggering (left) and constant fraction triggering (right) for pulses of different amplitudes.

.

similar charge outputs is plotted. σ_{sliced} is determined as the standard deviation of a Gaussian fit of the time distribution.

The Nagoya group has also constructed and beam tested (in a 3 GeV pion peam) two prototypes ([28] and [30], see Fig. 3.12) of a TOF counter using quartz as a Cherenkov radiator and MCP-PMT's. The group also tested the MCP's themselves as detectors with Cherenkov light radiated in the 3 mm quartz window in front of the photocathode. Their first prototype used a Hamamatsu 10 μm tube and a 40 mm long quartz radiator directly in front of the tube. It obtained a time resolution of σ=10.6 ps, dominated by the electronics component which they estimated to be around 8-9 ps. The number of photoelectrons detected was 100-200. With so many photoelectrons the resolution component of the PMT is much lower that the single electron transit time spread and the rising slope of the output pulses is so pronounced that there is no need for a constant fraction discriminator. On their second prototype they used a Hamamatsu 6 μm tube with a 10 mm quartz radiator. Their readout electronics were replaced by a

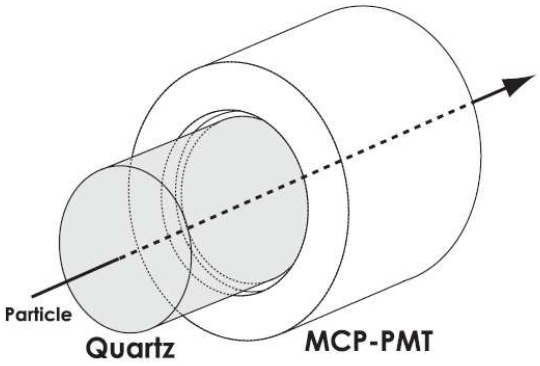

Figure 3.12. Schematic drawing of the Nagoya TOF counter.
Reproduced from [30].

time-correlated single photon counting module (Becker&Hickl GmbH SPC-134) with a time resolution of 4.1 ps. The time resolution obtained was σ=6.2 ps.

CHAPTER 4

THE QUARTIC DETECTOR

4.1 Detector geometry of the original design

The QUARTIC TOF counter is meant to be a near beam detector. It cannot be in the path of the beam as the prototype tested by the Nagoya group because the protons at the LHC have very high energies. It is not desirable to bring a photomultiplier tube so close to a 7 TeV beam. Furthermore the protons to be detected, which are 3 mm separated from the beam, have only lost 60 GeV/c of their momentum so they are still very energetic themselves and the PMT must not be in their path.

The original design, proposed by Mike Albrow from Fermilab is shown in Figs. 4.1 and 4.2. The Cherenkov radiator consists of bars of fused silica which is similar to quartz but has better transmission properties, see Fig. 4.3. The photodetector is the 8×8 pixel multi-pad anode Burle Planacon 85011-501 MCP-PMT with either 10 μm or 25 μm pores and with each fused silica bar matching a pixel for individual readout. The bars are oriented at the Cherenkov angle so that the radiation emitted is guided towards the PMT which lies off the path of the beam by 43.1mm as is shown in Fig. 4.4. The index of refraction of fused silica, see Fig. 4.5, shows a strong variation for lower wavelengths and is more steady at longer wavelengths. To optimize the design the bars must be oriented at the Cherenkov angle given by the mean value of the index of refraction. The

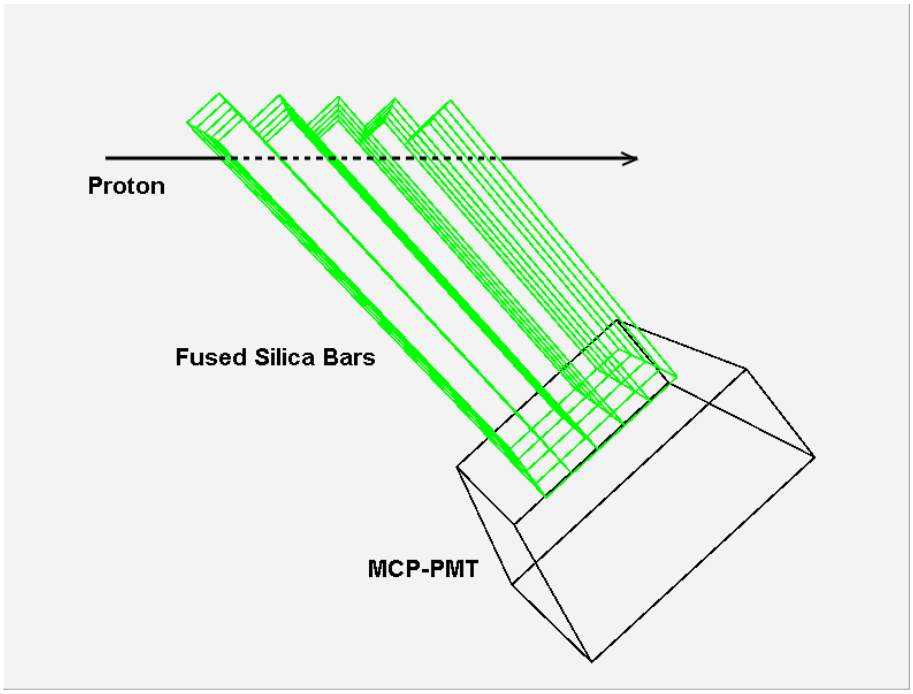

Figure 4.1. QUARTIC, original design.

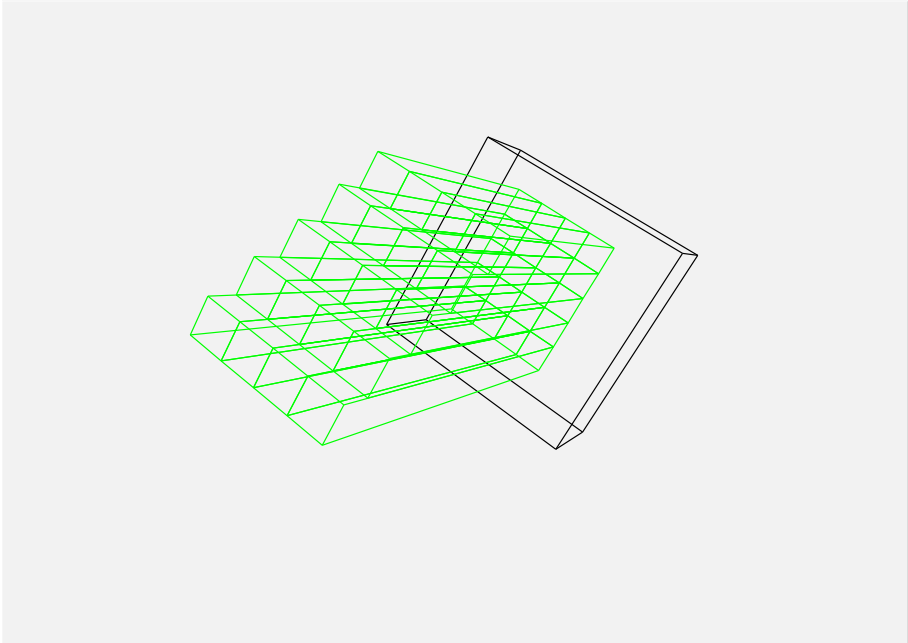

Figure 4.2. QUARTIC, original design. Another view.

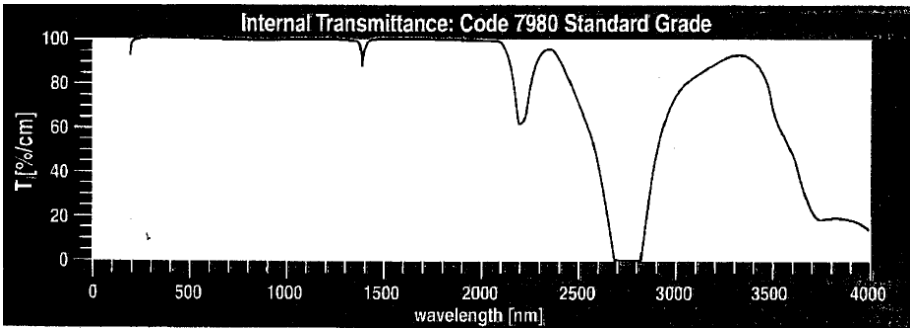

Figure 4.3. Internal transmittance of fused silica. Percentage loss on intensity per centimeter, provided by Corning Specialty Glass.

index of refraction is weighted by the number of photons accepted at a given wavelength, see Eq.(3.3), assuming $\beta \approx 1$ (particles traveling near the speed of light)

$$\left(\frac{dN}{d\lambda}\right)_{\text{accepted}} \propto L_{\text{rad}} \frac{\epsilon(\lambda)}{\lambda^2}\left(1 - \frac{1}{n^2(\lambda)}\right)$$

$$n_{\text{avg}} = \frac{\int_{185\text{nm}}^{650\text{nm}} n(\lambda)\left(\frac{dN}{d\lambda}\right)_{\text{accepted}} \mathrm{d}\lambda}{\int_{185\text{nm}}^{650\text{nm}} \left(\frac{dN}{d\lambda}\right)_{\text{accepted}} \mathrm{d}\lambda} = 1.5029$$

$$\Rightarrow \theta_c = 48.3^\circ \tag{4.1}$$

where $\epsilon(\lambda)$ includes the quantum efficiency of the photocathode and the collection efficiency of the photomultiplier tube. The quantum efficiency is the average percentage of incident photons that convert to photoelectrons and is dependent on wavelength. The collection efficiency depends mainly on the packing ratio of the micro-channels on the MCP and is a constant. Figure 4.6 shows the quantum efficiency of the photocathode for the Burle Planacon MCP-PMT. The quantum efficiency was determined by radiant sensitivity data provided by the manufacturer. The radiant sensitivity is defined as the

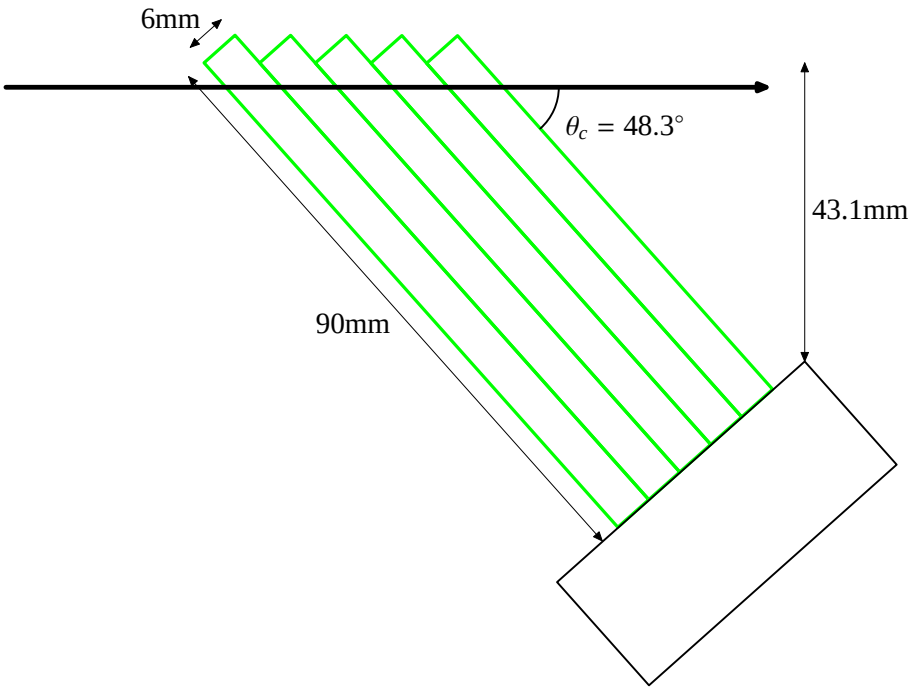

Figure 4.4. Geometry of the QUARTIC.

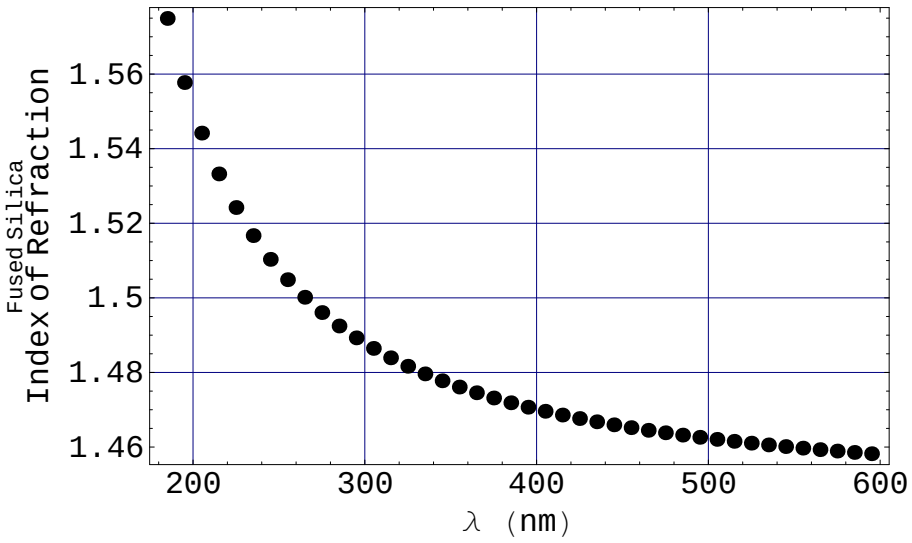

Figure 4.5. Index of Refraction for fused silica.

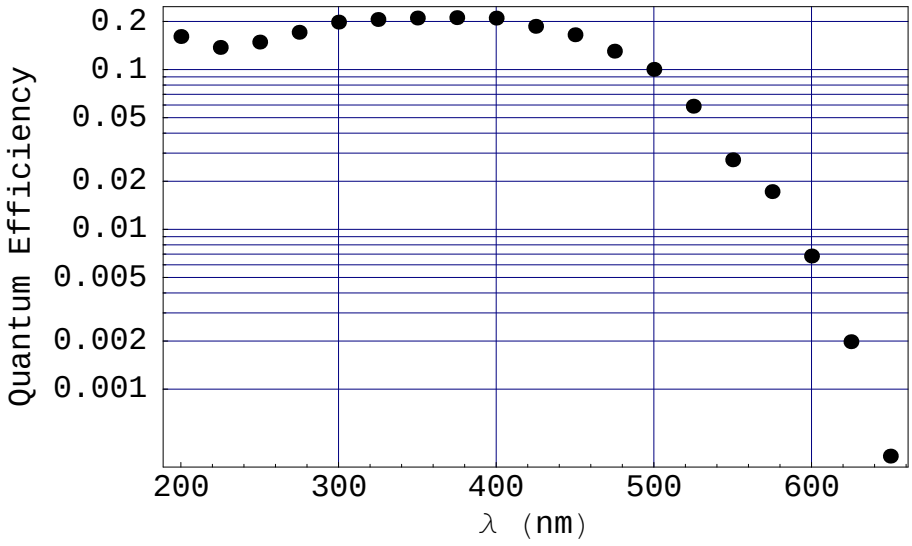

Figure 4.6. Photocathode quantum efficiency, Burle Planacon MCP-PMT.

photocathode current emitted per watt of incident radiation and is expressed in mA/W. One obtains,

$$\frac{N_{\rm pe}}{N_\gamma} = 100 \times \text{Q.E.} = (\text{R.S.})\,\frac{hc}{\lambda e} = (\text{R.S. in mA/W}) \times 123.9\,\text{W/mA}.$$

The internal transmittance of fused silica drops quickly to zero for wavelengths less than 185 nm and the quantum efficiency of the photocathode goes to zero for wavelengths greater than 650nm, so the integral in Eq.(4.1) is restricted to $\lambda_{\rm min} = 185$ nm and $\lambda_{\rm max} = 650$ nm. No internal transmittance factor is included in the integrand since this is a constant ≈ 1 in the whole 185-650 nm range. The number of photoelectrons accepted per bar not taking into account losses due to reflectivity, which depend on the number of bounces of each photon on the bar's boundary, is

$$N_\gamma = 2\pi\alpha L_{\rm rad} \int_{185\,\rm nm}^{650\,\rm nm} \frac{\epsilon(\lambda)}{\lambda^2}\left(1 - \frac{1}{n^2(\lambda)}\right) {\rm d}\lambda = 73\,\text{photons}$$

where the length of the path through the radiator is $L_{\rm rad} = (6/\sin\theta_c)$mm.

4.2 Ray tracing simulations

The distribution in time of the photons that arrive at the photodetector introduces the detector component of the TOF counter's resolution, see Eq.(3.1). This distribution depends on the properties of Cherenkov light and the geometry of the radiator. The first approach to study the feasibility of the original design was to carry out an "infinite statistics" simulation sweeping through the entire phase space of the problem and then normalizing the amount of light with N_γ obtained above. This gives us an idea of the average behavior of the amplified photoelectrons. The behavior obtained in this way is a statistical average since the number of emitted photons for every proton that goes trough is so small ($\sim$100). There are Poisson statistics effects in the actual number of emitted photons for a particular event and a uniform distribution of the azimuthal angles of emission of this photons in the Cherenkov cone.

A GEANT4 Monte Carlo study has been performed by Yushu Yao of Alberta. In this approach the passage of the proton through the radiator is simulated in a step-wise manner and photons are emitted discretely in a random fashion generated by the Monte Carlo engine GEANT4 according to the input materials and geometry. The passage of each of the emitted photons through the quartz is then followed and the time distribution of photons arriving at the photocathode is obtained. Repeating this process multiple times and averaging the time distributions of photons arriving at the photocathode one recovers the results obtained by our infinite statistics simulation.

An outgoing Cherenkov photon is parameterized by the azimuthal angle, its wavelength and the point in the radiator where it was emitted, see Fig. 4.7[1]. All the photons do not lie exactly on the cone, since their Cherenkov angle has a slight wavelength dependence. The simulation is carried out for each bar separately and a suitable coordinate system *abc* is defined with the *c*-axis going in the direction of the bar, the *a*-axis going

[1]Note that ϕ is unconventionally measured from the negative y-axis so that the bar is at $\phi = 0$

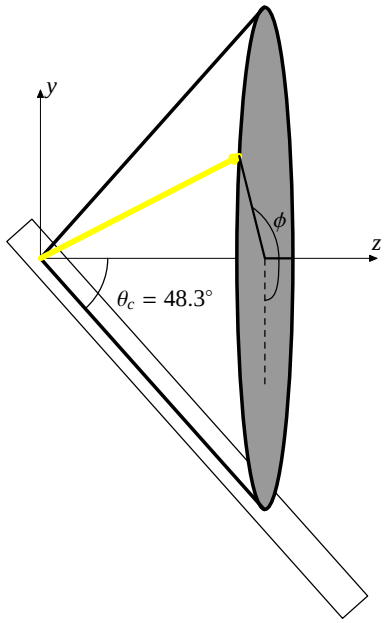

Figure 4.7. Emission of a Cherenkov photon.

into the paper in Fig. 4.7 and the b-axis perpendicular to the bar in the plane of the paper. The direction of the photon and the point of emission are transformed to this system and this allows a straightforward calculation of the time it takes for the photon to reach the photocathode and the details of its trajectory, i.e. bounces on the interfaces and total internal reflection. It is simple to visualize that the photons that reach the end of the bar first are traveling almost parallel to it and are internally reflected in the fused silica. In the simulation the photons are weighted by a factor

$$\frac{R(\lambda)^{(\#\text{ofbounces})}\epsilon(\lambda)}{\lambda^2},$$

where $R(\lambda)$ is the reflectivity of a thin aluminum boundary that isolates each bar, see Fig. 4.8. The factor $R(\lambda)^{(\#\text{ofbounces})}$ is only counted when there is no total internal reflection in the interfaces. Since $\epsilon(\lambda)$ includes the quantum and collection efficiency, we determine the number of photoelectrons that are ultimately multiplied (or amplified) by the photodetector, I refer to these as the accepted photoelectrons. The time

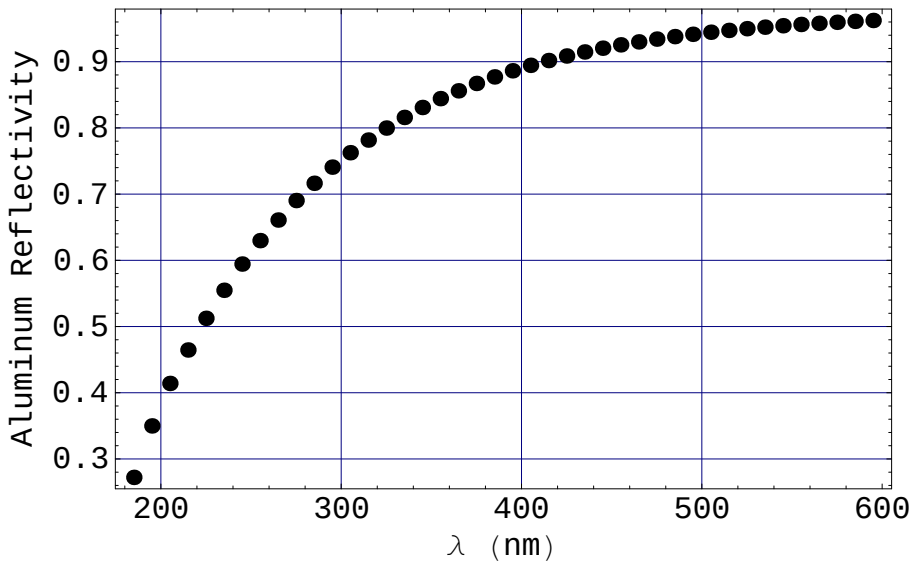

Figure 4.8. Aluminum reflectivity.

distribution of the accepted photoelectrons is shown in Fig. 4.9. The projections in the a, b, c-axes and the number of bounces associated with accepted photoelectrons are shown in Figs. 4.10 and 4.11. The projections give an idea of what section of the cone is most likely to make it to the PMT. A lot of light is seen to come from $\phi = \pm\pi/2$.
Other interesting plots are the spectra of light amplified by the photodetector, Fig. 4.12, the dependence of arrival times on wavelength, Fig. 4.13, and the dependence of arrival times on angle of emission on the cone, Fig. 4.14. A summary of the results for the simulation of the 90 mm bar is shown in Table 4.1. The results of this simulations were presented in the 2006 APS April meeting [32]. From the graphs one can conclude that the time spread arises due to the dispersion of the light in the fused silica. The shorter wavelengths in particular propagate much slower and this is the most significant contribution to the time spread. A way to reduce this effect is to have shorter bars, but since the tube has to remain at a fixed distance from the beam, the remaining gap has to be an aluminized air light guide all the way to the pixel.

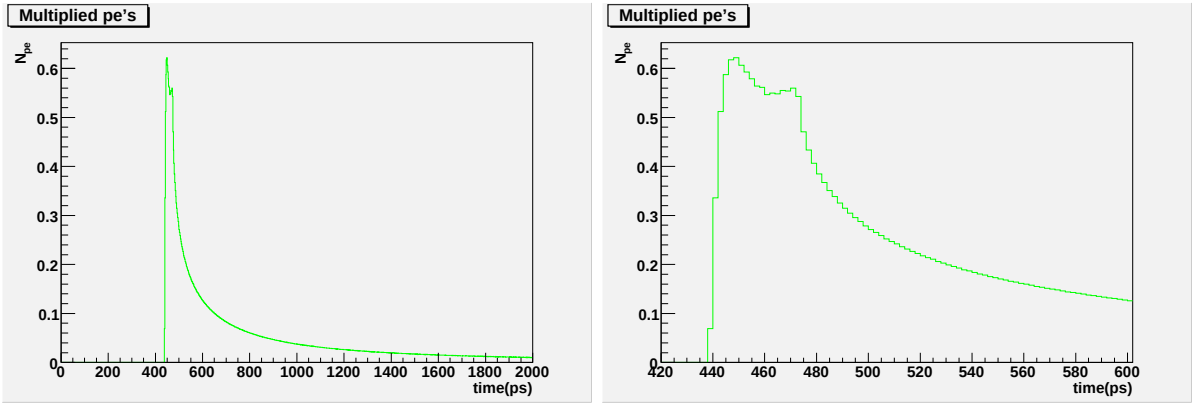

Figure 4.9. Time distribution of amplified photoelectrons (left) and a close up on the 400-600 ps range (right). 90 mm bar.

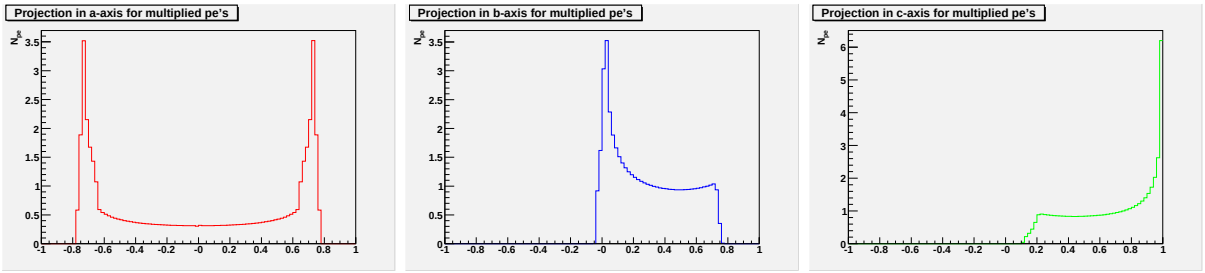

Figure 4.10. Direction of the photons. Projections in the a,b and c axes. 90 mm bar.

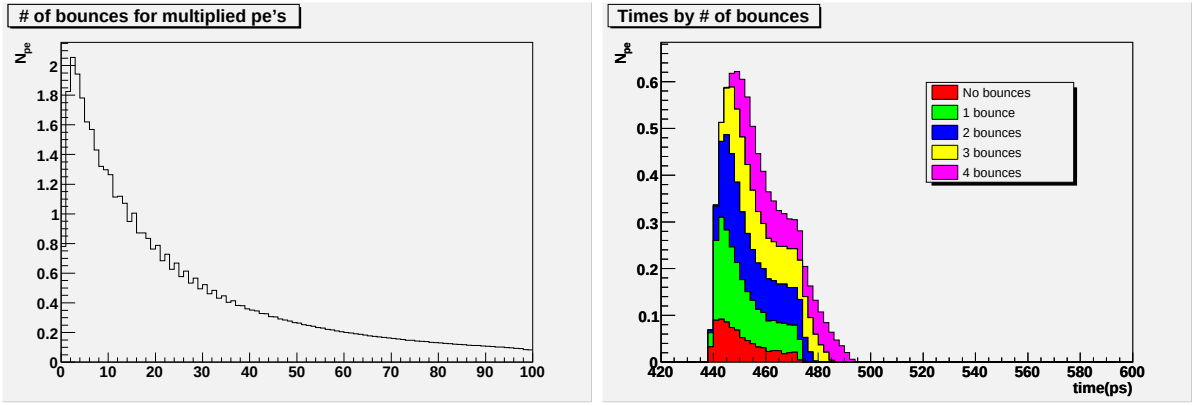

Figure 4.11. Number of bounces for amplified photoelectrons. 90 mm bar.

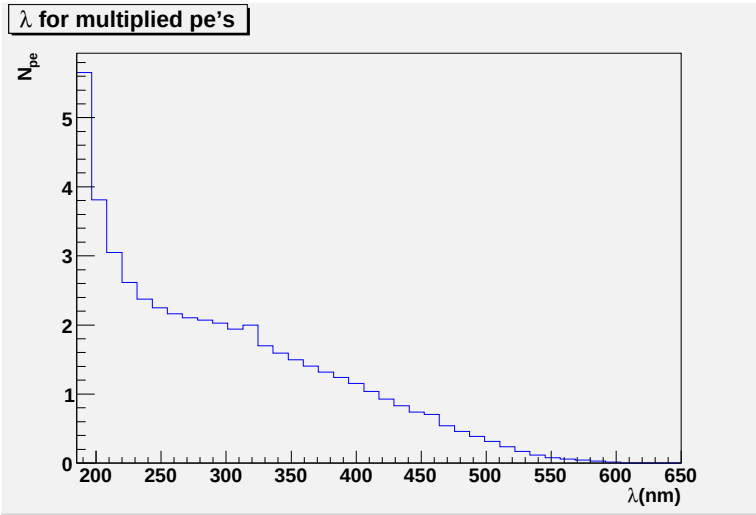

Figure 4.12. Wavelength distribution of photons that yielded amplified photoelectrons. 90 mm bar.

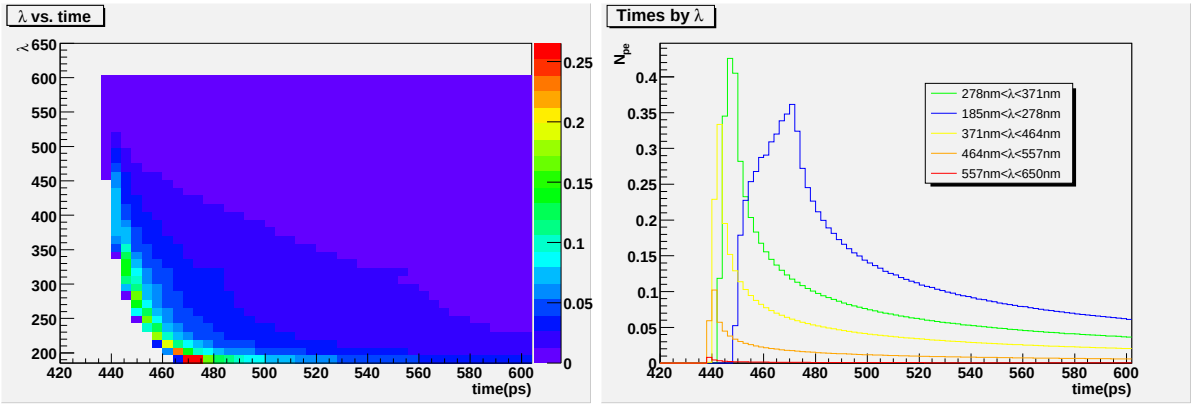

Figure 4.13. Arrival time dependence on wavelength, 90 mm bar.

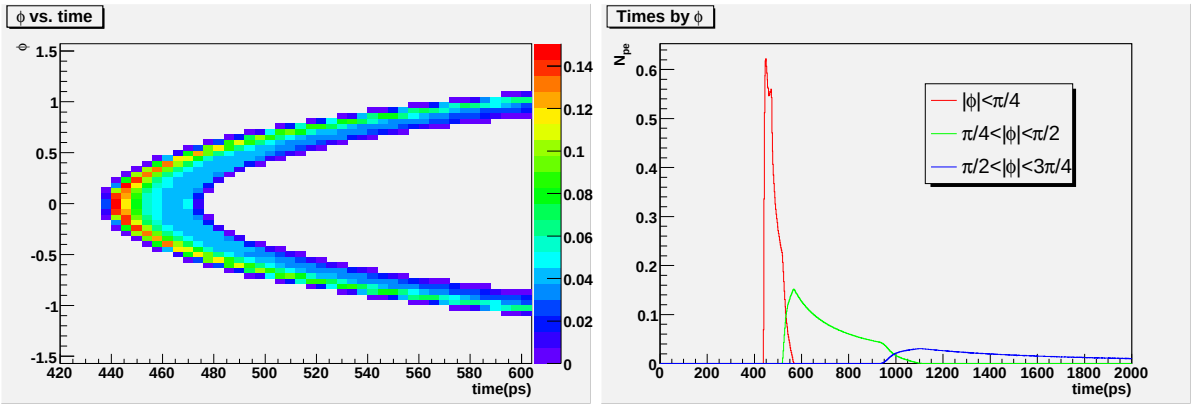

Figure 4.14. Arrival time dependence on angle, 90 mm bar.

Table 4.1. Summary of results for a 90 mm bar

Time of the first photon to arrive at the photocathode	437.9 ps
Total number of accepted pe's in the 0-2000 ps range	46
RMS of the time distribution	373 ps
FWHM of the time distribution	52 ps
Rise time	11.127 ps
Accepted pe's in the first 10 ps after the fastest photon	2.1
0-20 ps	5.0
0-30 ps	7.8
0-40 ps	10.4
0-80 ps	16.3
0-100 ps	18.3

4.3 Results of simulations for the second design

The second design with the air light guides is shown in Figs. 4.15, 4.16. It uses 15 mm-long fused silica bars and an aluminized air light guide. Here we have to consider the refraction of the photons in the silica-air interface. The photons will bend outwards from the normal and will bounce more times, some of them will be internally reflected and will not make it to the air light guide. The results of the simulation for the air guide design are in Figs 4.17-4.22 and Table 4.2.

Table 4.2. Summary of results for a 15 mm bar, 75 mm air guide

Time of the first photon to arrive at the photocathode	323.2 ps
Total number of multiplied pe's in the 0-2000ps range	5.12
RMS of the time distribution	19.2 ps
FWHM of the time distribution	4 ps
Rise time	1.76 ps
Accepted pe's in the first 10 ps after the fastest photon	3.5
0-20 ps	4.08
0-30 ps	4.39
0-40 ps	4.59
0-80 ps	4.99
0-100 ps	5.08

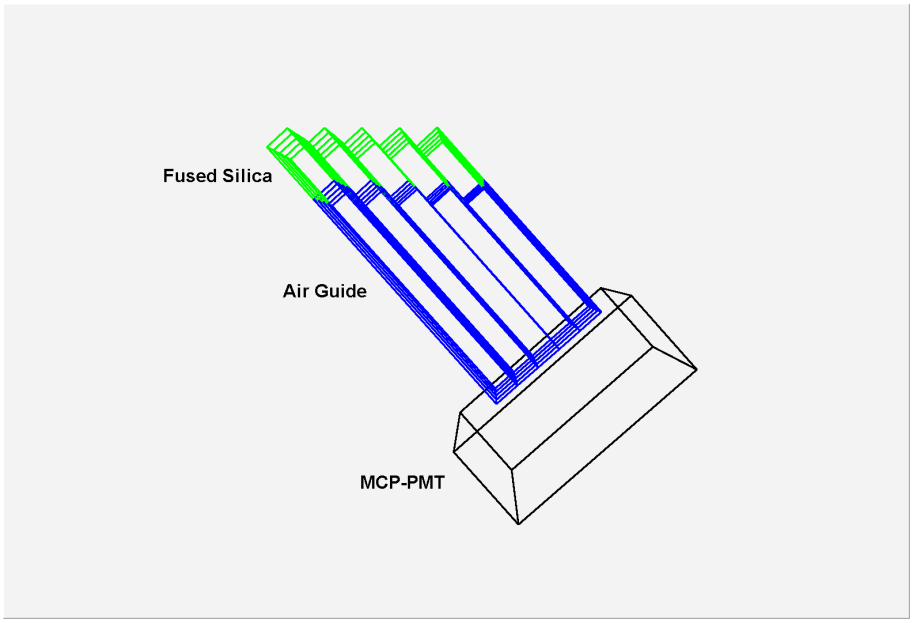

Figure 4.15. QUARTIC, air guide design.

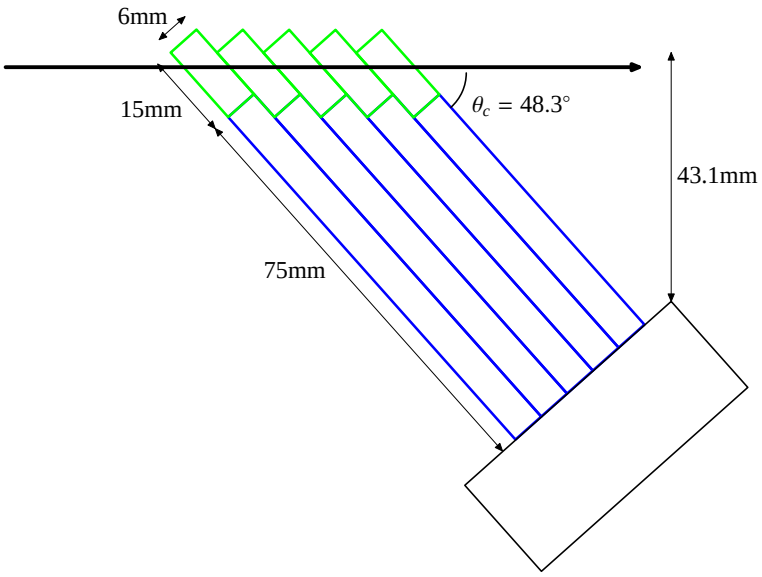

Figure 4.16. QUARTIC, air guide geometry.

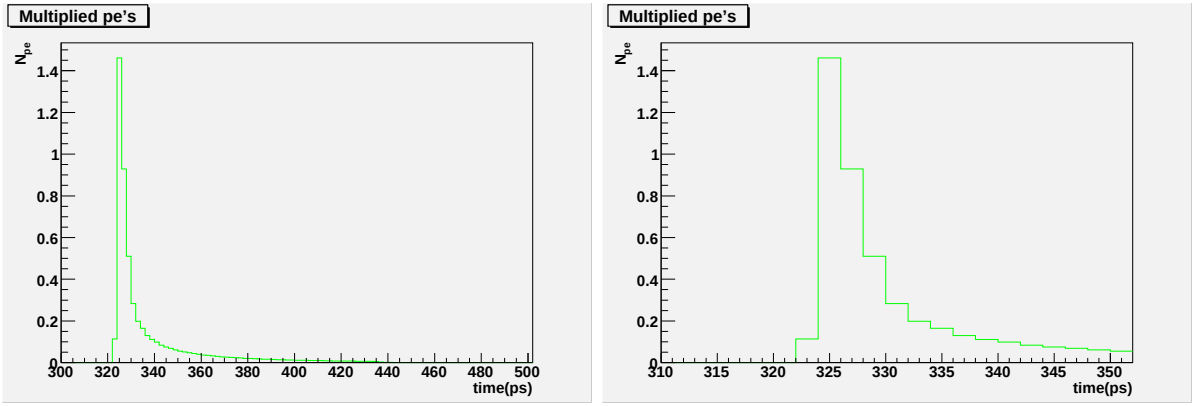

Figure 4.17. Time distribution of amplified photoelectrons (left) and a close up on the 310-350 ps range (right). 15 mm bar, 75 mm air guide.

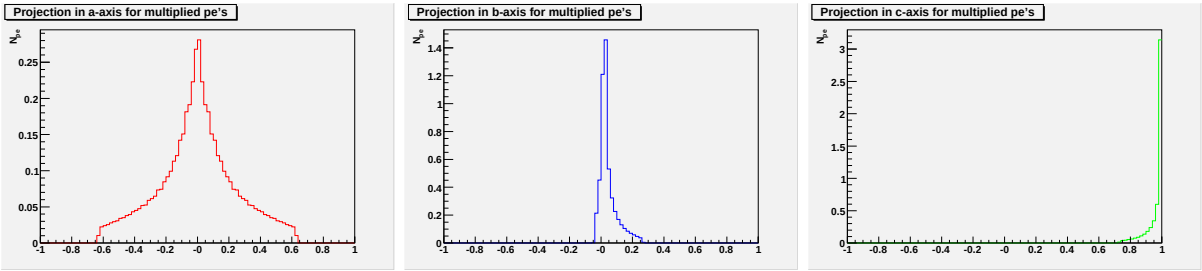

Figure 4.18. Direction of the photons. Projections in the a,b and c axes. 15 mm bar, 75 mm air guide.

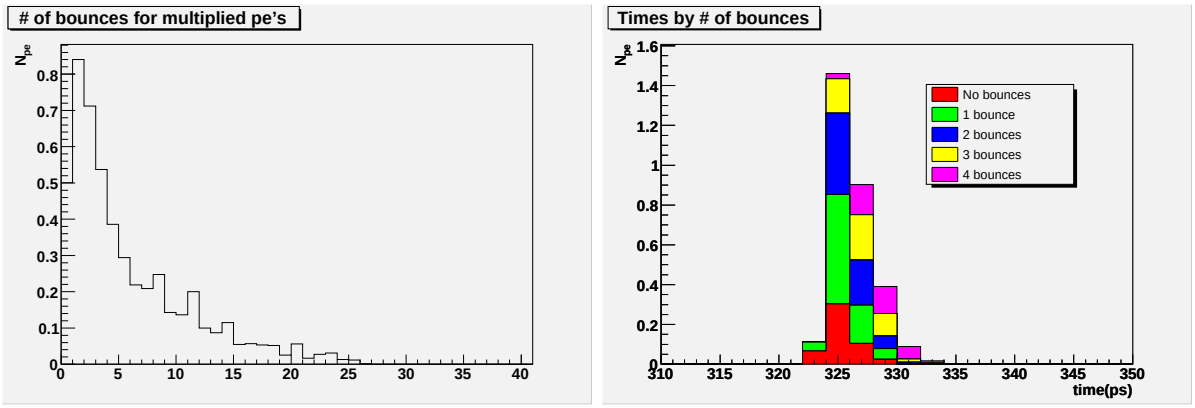

Figure 4.19. Number of bounces for amplified photoelectrons. 15 mm bar, 75 mm air guide.

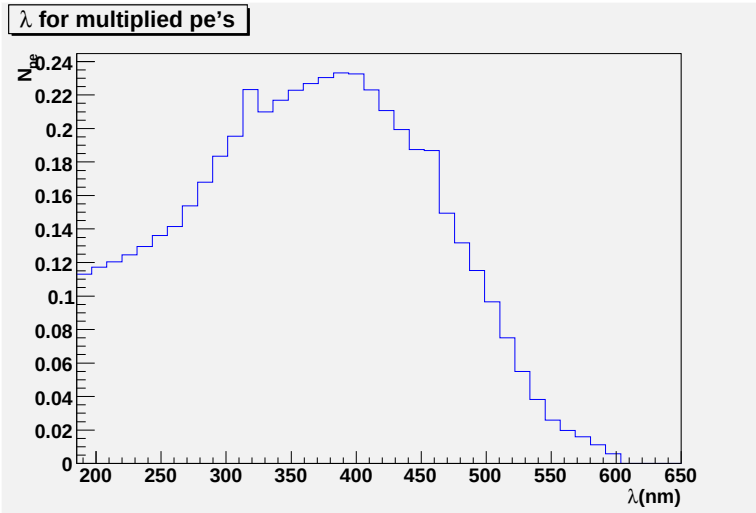

Figure 4.20. Wavelength distribution of photons that yielded amplified photoelectrons. 15 mm bar, 75 mm air guide.

The effect of the air guide modification is dramatic. The available photons are the same in both cases so this is effectively providing cutoffs to keep only the fastest photons. A comparison of the projections of the photons on the a axis shows that refraction at the silica-air interface causes more bounces in the aluminum, which singles out the ϕ=0 region of the cone, at the expense of most of the light generated, from 46 photons in

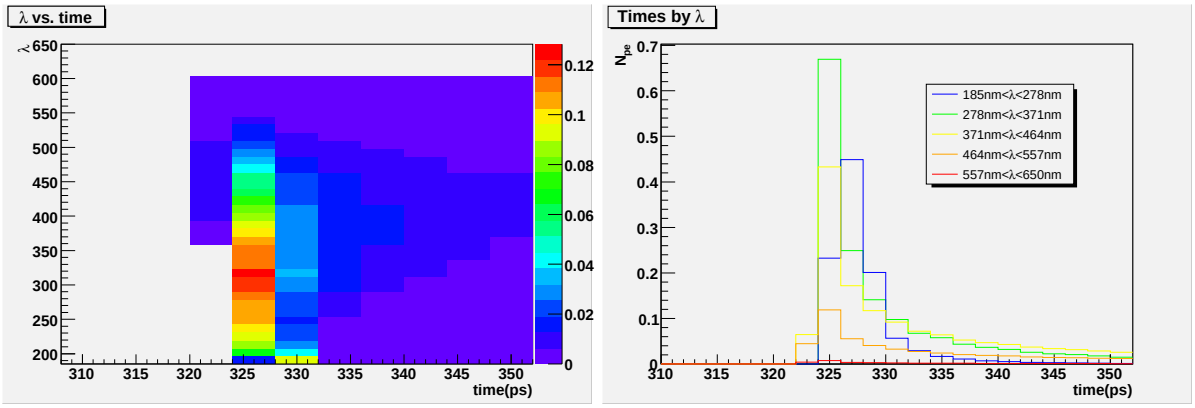

Figure 4.21. Arrival time dependence on wavelength, 15 mm bar, 75 mm air guide.

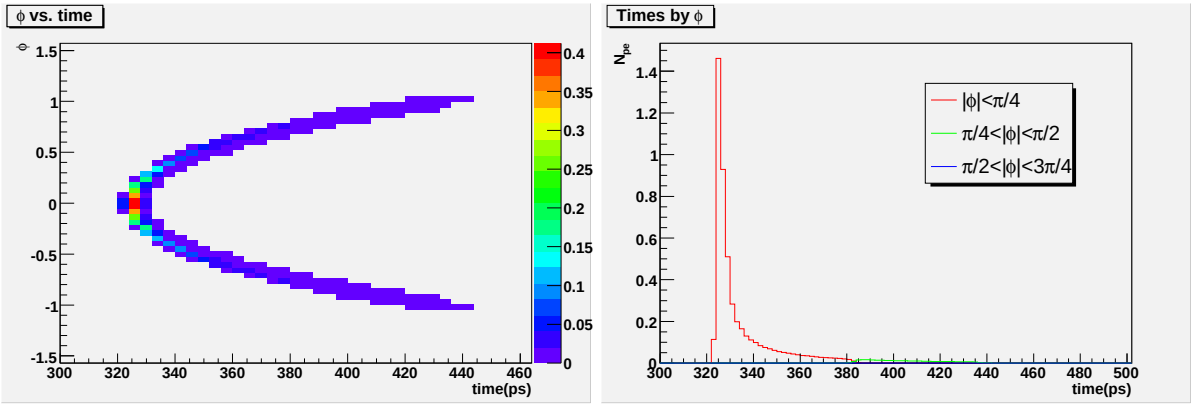

Figure 4.22. Arrival time dependence on angle, 15 mm bar, 75 mm air guide.

the 90 mm bar to 5 photons in the air guide case. The shorter fused silica section also minimizes chromatic spread of the time distribution.

The time distribution is not Gaussian, but in order to obtain an estimate of σ_{counter}, according to Eq.(3.1) we assume it is with an standard deviation of $\sigma_{\text{det}} = 20$ ps, the RMS of the time distribution. The results from the Stanford group concluded $\sigma_{\text{MCP}} \sim \sigma_{\text{TTS}}/\sqrt{N_{\text{p.e.}}}$, and in our case $N_{pe} \sim 1$ so $\sigma_{\text{MCP}} = \sigma_{\text{TTS}} = 71$ ps, for a 25 μm Burle MCP-PMT, see Fig. 3.7. For the electronics resolution component, suppose we had the $\sigma_{\text{elec}} = 4.1$ps Beckr&Hickl single photon counting module of the Nagoya group this would give us

$$\sigma_{\text{counter}} = \sqrt{20^2 + 71^2 + 4.1^2} = 74\text{ps}$$

for a single counter resolution, which using two identical counters would allow the measurement of a time difference with a resolution down to $\sigma_{\text{TOF}} = \sqrt{2} \times 74\text{ps} = 105\,\text{ps}$. With a 10 μm Burle tube (σ_{MCP}=33 ps) this estimate reduces to $\sigma_{\text{counter}} = 39$ ps and $\sigma_{\text{TOF}} = 55$ ps.

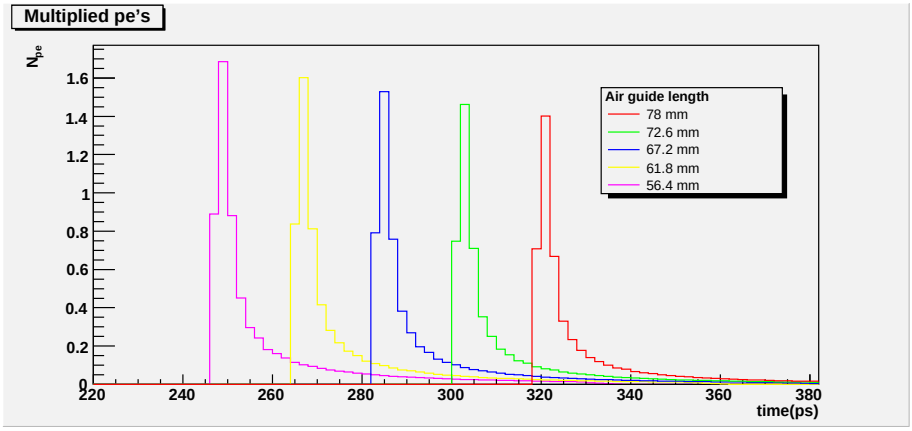

Figure 4.23. Multiplied p.e.'s time distribution for different air guide lengths..

4.3.1 Shorter light guides

Not all of the light guides in a row of the detector have the same length and the time distribution will not be identical for all of them. Each air light guide is $(6/\tan\theta_c)$ mm = 5.4 mm shorter than the previous one. So we have lengths of 78, 72.6, 67.2, 61.8, 56.4 mm. The time distributions for the various lengths are in Fig. 4.23. The average number of accepted photoelectrons is 5.0, 5.2, 5.6, 5.9, and 6.3 from longer to shorter air guides.

4.3.2 Detector Efficiency

The detector efficiency can be estimated assuming that the actual number of multiplied photoelectrons for each event has a Poisson distribution. The probability of having zero amplified photoelectrons is thus $e^{-\lambda}$ where λ is the average number of amplified p.e's obtained from the simulations. From longer to shorter air guides the ineffieciencies would be 0.7%, 0.5%, 0.3%, 0.2%, and 0.1%.

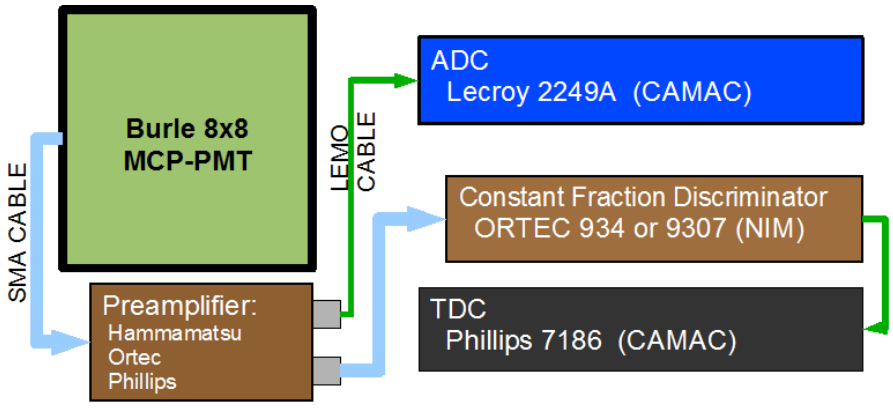

Figure 4.24. Readout electronics used in the Test Beam with the first prototype.

4.4 Readout electronics and reference time system

As was mentioned in Section 3.4.2, the MCP-PMT output pulses have randomly varying amplitudes and the electronics used to time them is an important component of the time resolution. The basic readout electronics consist of a preamplifier, a constant fraction discriminator (CFD) and a time to digital converter (TDC). Some of the pre-amps we used provide two outputs and the possibility of measuring the charge output of the pulses with an ADC (Analog to Digital Converter), see Fig. 4.24. The NIM output of the CFD is used as the START or STOP input of the TDC. For the purposes of this document, the TDC is considered part of the data acquisition system and is described in the next chapter.

In a CFD the input signal from the pre-amplifier is supplied to two circuits, as shown in Fig. 4.25, a regular threshold discriminator and the constant fraction circuit. The output of the CFD is the logical AND of the two circuits. The purpose of the threshold circuit is to enable the operation of the unit for pulses above a certain threshold only, this means that in the logical AND the CFD bit arrives later and dominates the timing. In the CFD part the input signal is split into two copies, one is attenuated and then subtracted from the other, which is delayed using a short cable. The resulting signal crosses zero

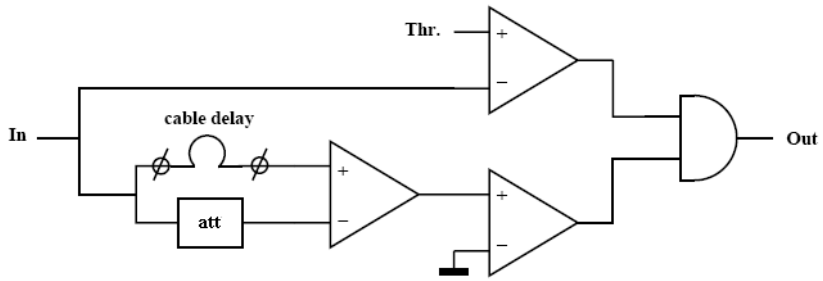

Figure 4.25. CFD schematic.

at a fixed time approximately independent of the amplitude of the input pulse. Another comparator switches to true at the zero crossing and triggers the AND. The principle of operation of the CFD's can be understood if the rising edge of the pulses is approximated linearly, then for the CFD part of the circuit,

$$V_{\text{delay}}(t) = m(t-d) \quad V_{\text{att}}(t) = mrt$$

where d is the delay and r is the attenuation factor. The zero crossing is given by

$$0 = V_{\text{delay}}(t_0) - V_{\text{att}}(t_0) = m(t_0 - d - rt_0)$$

$$\Rightarrow t_0 = \frac{d}{1-r},$$

independent of slope. The delay must be short enough such that the zero crossing is in the region where the rising edge of the pulse is still linear and long enough that the CFD bit arrives later than the threshold bit to the logic AND. The latter condition depends also on the level at which the threshold part of the circuit is set; the time when the pulse crosses the level being $t_L = V_L/m$, which depends on the slope. If the delay is short and the level is high then lower amplitude pulses will exhibit timewalk since the CFD circuit will trigger before the threshold circuit, implying that the threshold part of the circuit will determine the timing. The threshold must be selected just above the noise, to avoid problems with the lowest amplitude pulses.

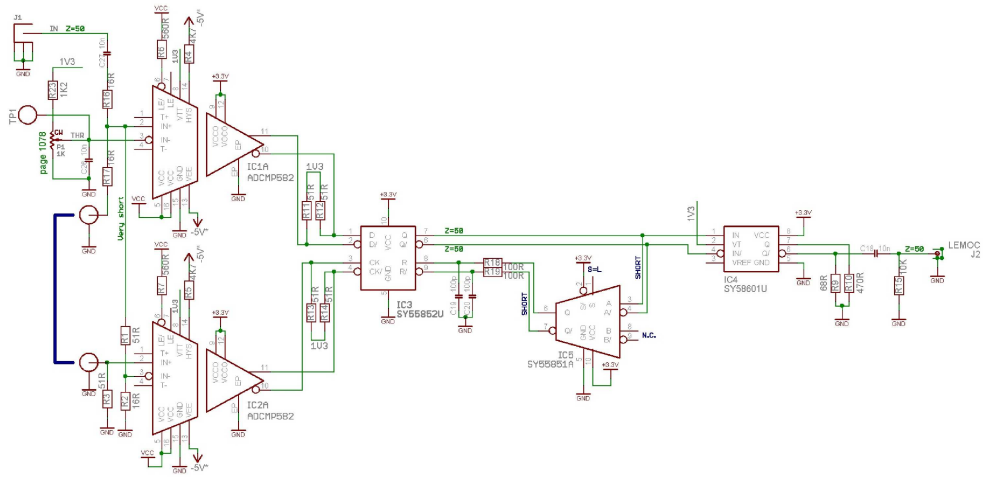

Figure 4.26. Louvain CFD board schematic.

For fast timing applications the best way to avoid noise and degradation of the signal is to have a short delay which requires pulses of fast rise times. The pre-amp that is used before the CFD unit must be very fast, at least 1 GHz bandwidth, to conserve the fast rise time of the MCP-PMT output pulses, $\sim$ 500 ps [2].

The choice of pre-amp and CFD is an important part of the overall detector design. Off-the-shelf components are bulky and expensive, so we are seeking a more compact and economical solution. The University of Alberta and UC Louvain are developing two different solutions for the readout electronics. Louvain developed a low cost custom-made fast amplifier board using a Phillips BGA2712 chip. This pre-amp board was used in the testing of the first prototype and was previously tested by the SLAC group and found to be almost as good as much more expensive commercial units. Louvain has also developed a 12 channel CFD NIM unit, see Fig. 4.26 that we used in the second run at the Test Beam in March 2007. Each channel consists of a separate daughter card that has an independent threshold control and a delay optimized for the phototube being used. We employed two different versions, one tuned for the faster Hamamatsu tube and the

[2]Rise time of a sine wave = $1/2f$=500 ps for f=1 GHz.

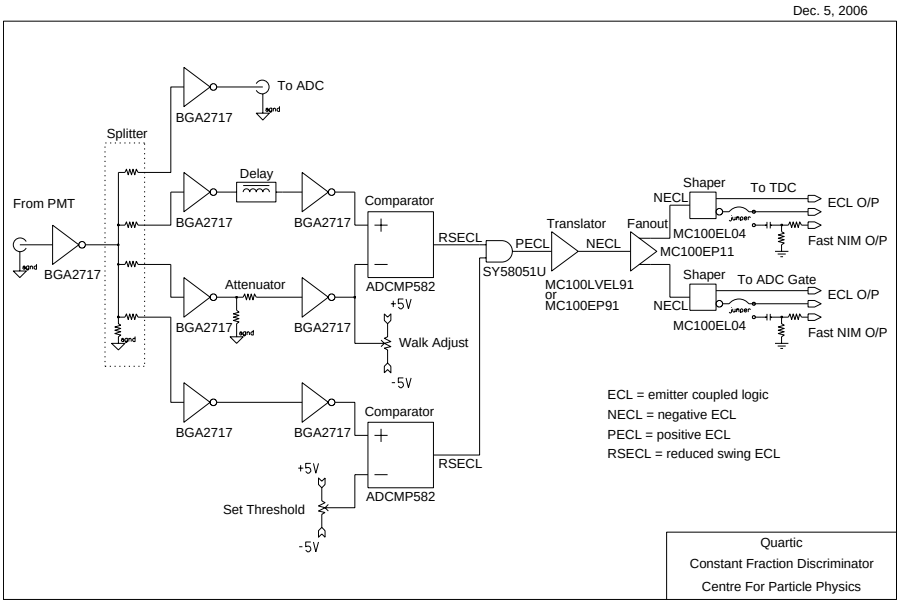

Figure 4.27. Alberta integrated board schematic.

other (most of the channels) optimized for the Burle MCP-PMT's. The engineers at Alberta are currently working on an integrated board containing both a pre-amp and a CFD to be used in the coming Test Beam run in July 2007. A feature of their board, see Fig. 4.27, is that it has ECL (Emitter Coupled Logic) outputs that can be used with the HPTDC chip (High-Performance TDC) which has a 25 ps least bit, is made of radiation hard 25 μm CMOS [33], and has been developed for use at the LHC. The ALICE collaboration has attained better than 20 ps in tests with the HPTDC [34]. The Alberta board also provides a copy of the pulse and a gate that can be fed into an ADC for pulse height measurements that would allow timewalk corrections after a suitable calibration.

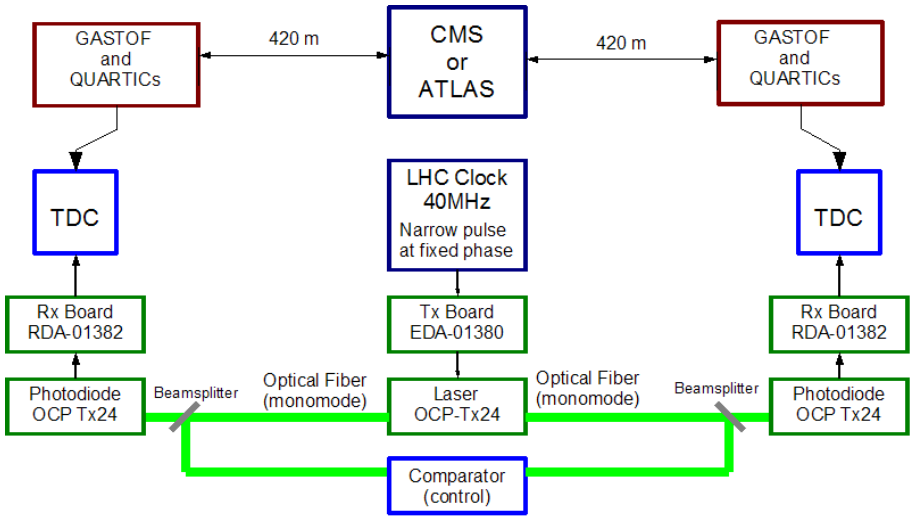

Figure 4.28. FP420 reference timing scheme.

4.4.1 Reference time system

Since we will measure the times at the left and right FP420 stations for each event, we need a reference time signal at both stations that has a small jitter. This signal will be provided by the LHC TTC (Timing Trigger and Control) system, see Fig. 4.28 [35]. A signal is derived from the 40 MHz LHC RF, converted to an optical pulse (Tx Board EDA-01380 and Laser type OCP Tx24) which is split and sent along fibers (as a monomode pulse) to both (L) and (R) detector stations for every bunch crossing. The pulse-to-pulse jitter between the arrival of these optical pulses is negligible (no electronics is involved). There can be longer term drifts, e.g. from temperature differences along the two arms, but these will be monitored by splitting the optical signal at the detectors and returning it to the source, where they are converted to electrical pulses in a receiver (Rx Board EDA-01382 and photodiode type OCP Rx24) and compared. At the detector stations the optical pulses are converted to electrical pulses to START or STOP the detector TDCs. Only jitter in this conversion affects the $t_R - t_L$ measurement used to determine the z-

vertex; any jitter in generation of the optical pulse cancels out. An rms (L-R) jitter of 4 ps can be expected, which is a negligible contribution to our resolution.

CHAPTER 5

FERMILAB TEST BEAM

In this Chapter I will describe Fermilab's Meson Test Beam Facility (MTBF), in which tests of the first and second QUARTIC and GASTOF prototypes have been carried out, and the DAQ solution that was implemented for our experiment.

5.1 MTBF Overview

The Meson Test Beam Facility [36] is a versatile beamline in which users can test equipment or detectors in a beam of moderate energy particles (1 to 120 GeV) at moderate intensities ($\sim$10 kHz). MTBF is a shielded area that has approximately 6 locations in the beamline where users can set up equipment to test, see Fig. 5.1. Our experiment, T958, was located in MT6 section 2C where there is a movable table with both horizontal and vertical motion, Fig. 5.2.

The MTBF beamline has 120 GeV protons coming from the Main Injector in RF buckets with a separation of 19 ns in a spill that lasts 4 s out of each minute. Beam is potentially delivered twelve hours per day with sporadic downtime due to shot setup of other accelerator operations. The composition of the beam is mostly protons for higher momentum tunes and mostly pions for lower momenta. The Test Beam facility has a tracking system consisting of Fenker type MWPC's (multi-wire proportional chambers) [37] which are modular in the sense that the number of chambers and their positions along the beam can be changed upon the user's request and MTBF approval. In our case, tracking is useful to measure the position of the counters in the beam and ultimately to measure how the efficiency varies with the position of the beam relative

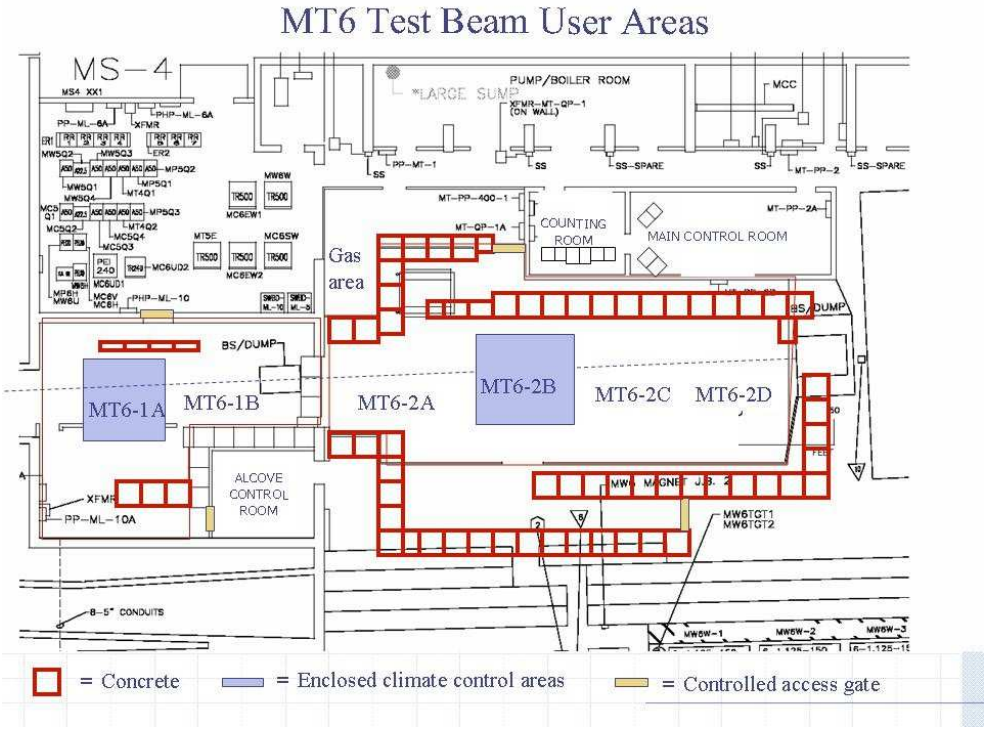

Figure 5.1. Test Beam user areas.

to the detector. At MTBF there is a DAQ system consisting of five CAMAC crates (Computer Automated Measurement and Control) controlled by a Linux PC. The Linux PC is in the main control room and one of the CAMAC crates is in the electronics room (or counting room), both are outside the beam enclosure, see Fig. 5.1, where the beam path is indicated by a dotted line. The other four CAMAC crates are located at different z locations along the beam. The CAMAC crate branch, controlled by a single computer, provides a versatile DAQ platform that can be adapted for the different experiments that are carried on at MTBF. With such a system the data taking rates are limited, though, unless some kind of fast readout system is implemented that does not require hand-shaking with the Linux PC for every data transfer.

Such is the case with the MTBF wire chamber tracking system. The tracking system is made up by MWPC stations, each connected to a CAMAC crate in the beam

Figure 5.2. MTBF section 2C.

line. Within each station there can be 4 to 6 planes (each plane is a 128-wire Fenker type MWPC for which the middle 64 wires are readout) oriented at 0,45,90,135,180, or 270° [1]. The spacing between the wires in each plane is 1 mm, with proper tracking software to fit the tracks, a good calibration algorithm, and sufficient amount of calibration data a resolution of 300 μm is expected. Each of the wires in a plane is readout by a LeCroy 3377 TDC operating in common stop mode. This means that whenever the passage of a charged particle fires a wire, the electronic signal from the wire START the TDC which counts the time until it receives a subsequent STOP signal. The LeCroy 3377 has 32-channels each connected to a wire and the common STOP signal is provided by the event trigger which is a coincidence of two scintillation counters in the beam line. The LeCroy 3377 modules are CAMAC units so at this point the readout could be performed by the Linux PC reading all the channels of all the TDC's one by one which would lend to a very low data taking rate. Instead, the TDC's are connected together via FERAbus[2] and dump data to one or more LeCroy 4302 16kB CAMAC memory modules. During the time it takes for the 3377's to dump data in the memories further triggers are inhibited using a gate generator, see Fig. 5.3. When the memory modules are 3/4 full they trigger

[1] 180° and 270° differ from 0° and 90° by an offset in the location of the wires.

[2] Fast Encoding and Readout ADC, the 3377 is a TDC compatible with the FERA Readout System.

readout by the Linux PC (a single memory can get 3/4 full and will trigger readout for all the MWPC stations). While the Linux PC is reading out the memories all further triggers are inhibited by a gate generator signal (LeCroy 2323) controlled by the PC. At the end of a spill the memory modules are also read out by the computer and it is up to the user if the current data file is closed and a new one opened or if writing continues on the same file. The data acquisition loop algorithm in pseudocode is as follows:

```
 1 open data file
 2 for ( n spills ) {
 3    do {
 4       if ( any 4302 memory > 3/4 full ) {
 5          /* Memory is 3/4 full */
 6          start gate 2323 veto
 7          for all crates read 4302 memories
 8          stop gate 2323 veto
 9          build data for events read
10          write data to file
11       }
11    } while (current spill)
12    /* Current spill is over */
13    start gate 2323 veto
14    for all crates read 4302 memories
15    stop gate 2323 veto
16    build data for events read
17    write data to file
18    /* User can select :
19    -- close file and open a new data file
20    -- continue with same file */
21 }
22 close data file
```

The hardware side of the procedure is explained in Fig. 5.3. The figure shows how any further triggers are vetoed while the memory modules are storing the data for an event as explained above, without intervention from the computer. The logic in the diagram

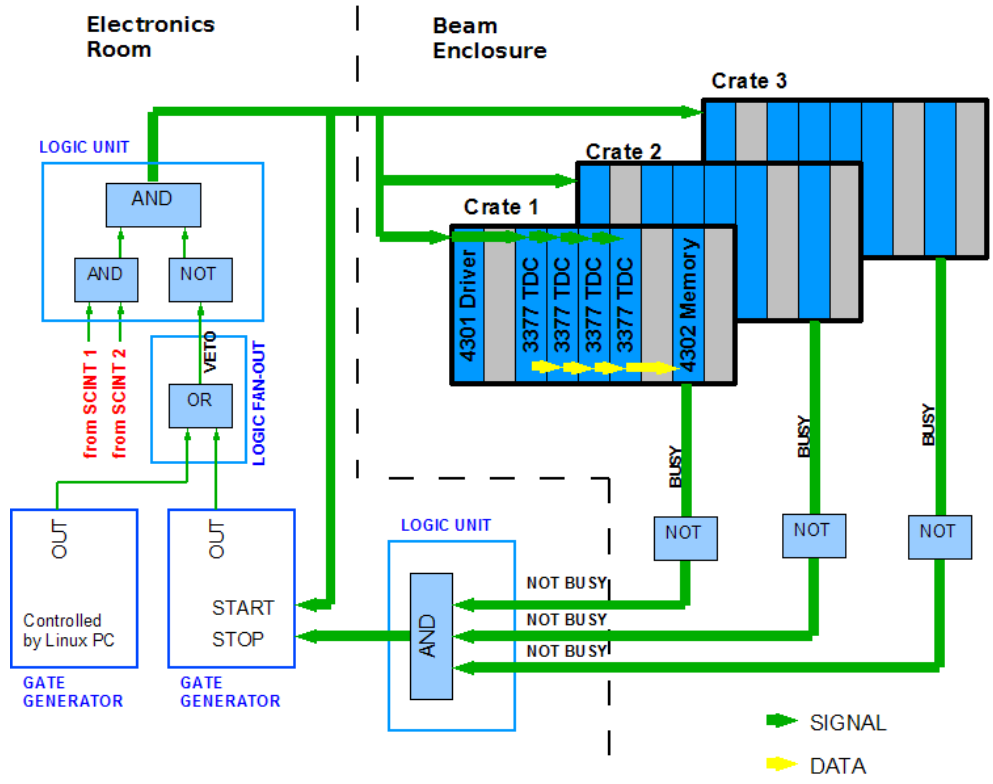

Figure 5.3. MWPC trigger logic.

should be followed starting from the coincidence of the two scintillators. The MWPC FERA DAQ system is very fast, when used by itself it can read out a few thousand of events per spill.

An experimenter that wants to take advantage of the tracking system has two possibilities. One would be to use FERA compatible TDC's (LeCroy 3377) and ADC's (LeCroy 4300B) to digitize any detector signals and connect them to the 4301 driver and 4302 memory modules. This would imply also some modification of the DAQ loop's source code and configuration settings for proper initialization of the added modules. Some experiments require data acquisition modules more specialized than the FERA TDC's and ADC's. The LeCroy 3377 TDC has a least significant bit of 500 ps, while the Phillips 7186 TDC that we use for fast timing has a least significant bit of 25 ps. The

second possibility to take advantage of the tracking is to synchronize any DAQ system that the experimenter may be using with the MWPC DAQ by providing them the same trigger. This has some subtleties since the trigger must be inhibited when any of the two systems is busy. This last option is the one that we implemented for our DAQ system and is described in the rest of this chapter. The next section describes the standalone DAQ system with the Phillips 7186 TDC and the last section describes the integration with the tracking system.

5.2 Standalone DAQ system

The main component of our DAQ system is the Phillips 7186 TDC [38]. This model is a 16-channel, single slot CAMAC module that has a 25 ps least bit and a 100 ns range. The 7186 has front end INHIBIT and CLEAR inputs and a BUSY output. It can be used in common start or common stop modes. The 7186 is installed in the CAMAC crate closest to the movable table in section 2C. A crucial element for fast timing is to avoid the degradation of the pulses as they travel through the signal cables. As was mentioned before, preservation of the fast rise time is important for the correct operation of the CFD. In coaxial cables the losses (measured in dB/m) are frequency dependent, becoming higher as the frequency increases. For this reason, the cables that connect the MCP-PMT to the pre-amp and the pre-amp to the CFD must be of the best quality and as short as possible. LEMO cables, routinely used in high energy physics experiments, have a loss of $\sim$0.3 dB/m at 100 MHz while SMA cables have less significant losses of 0.65 dB/m at 1 GHz and only 4.4 dB/m at 26 GHz [39]. We used SMA cables from MCP-PMT to pre-amp and from pre-amp to CFD. From CFD to TDC we used LEMO cables. To be able to keep the cables as short as possible the TDC is used in common

stop mode[3]. The signal from a QUARTIC bar starts a channel of the TDC and the trigger signal stops all channels at the same time about 70 ns after the starts, thus inside the 100 ns range of the 7186. The trigger is formed by the coincidence of two scintillator paddles in the path of the beam. In the testing of our TOF counters we do not have a precise time reference[4] so we have to measure time differences between two of our TOF counters. The time resolution of the scintillator trigger stop is $\gtrsim$1 ns but it cancels out when taking the difference between two channels of the TDC.

The 7186 is read out by the Linux PC after every event. When it receives a STOP it exerts a LAM (Look At Me) which is detected by the computer in a poll loop. A slightly delayed copy of the STOP signal starts a LeCroy 2323 gate generator that is connected to the INHIBIT input of the TDC and to the trigger veto. This inhibits any further start signals from the detectors and vetoes any further triggers until the event is read out. When all the channels have been read out the computer stops the 2323 gate and the process repeats itself. The loop algorithm in pseudocode is as follows:

```
1 open data file
2 while ( events read < n events ) {
3    do {
4      if ( 7186 has an event) {
5        read data to file
6        reset 7186
7        stop gate 2323 inhibit
8        events read ++
9      }
10   } while ( current spill )
11   close current file
12   open a new data file
```

[3]In common start mode the signal has to be delayed using long cables so that it arrives at the TDC after the trigger.

[4]In laser setup experiments described in Section 3.4 the pulsed laser provides a signal correlated with the light with less than $\sim$35 ps jitter.

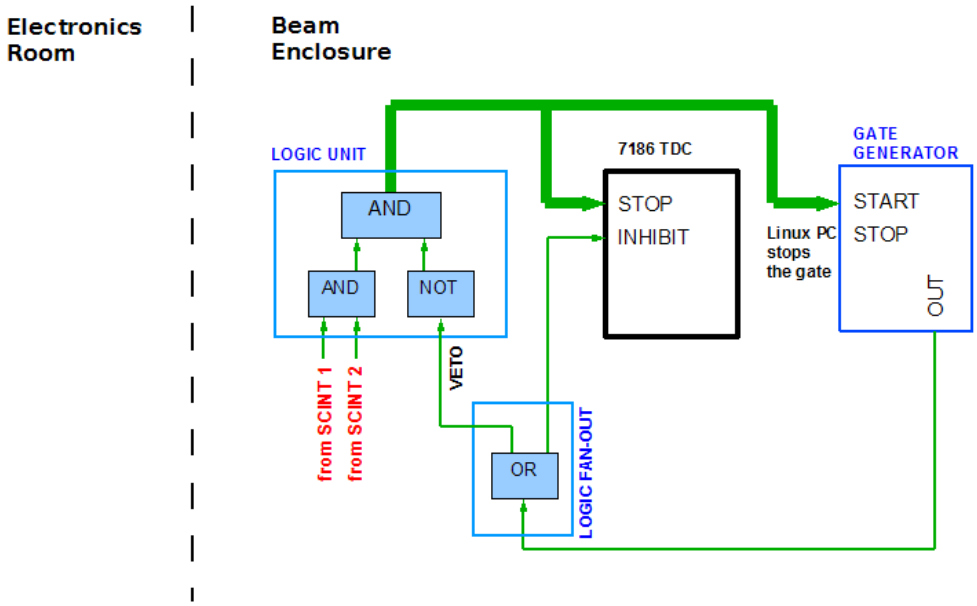

Figure 5.4. Standalone DAQ trigger logic.

```
13 }
14 close data file
```

Notice that the gate is started by the trigger and stopped by the computer. All the trigger modules are located inside the beam enclosure as can be seen in Fig. 5.4, which illustrates the procedure from the hardware point of view. The scintillators 1 and 2 here are different from the ones used in the MWPC trigger logic. In the standalone case they are two small (10 cm by 10 cm) pieces of scintillator that are parallel to each other, in the path of the beam and separated by about 5 cm. The pair was located in front of the movable table. The scintillators 1 and 2 in the MWPC trigger are more separated in z ($\approx$20 m) since they are also used to measure particle velocities in a TOF system for particle identification at MTBF.

5.2.1 sjyLX libraries

In order to implement the DAQ algorithm in the Linux PC, the appropriate libraries had to be written for the Phillips 7186 TDC. The way CAMAC works is there is a set of standard routines (the ANSI/IEEE CAMAC standard 758-1979 routines) that are used to control the CAMAC crates and the modules connected in the crates [40]. A CAMAC branch is a collection of crates connected in series or in parallel[5], whicn can be controlled by a single computer. Each CAMAC crate has a crate controller, which is generally a 2-slot wide module that is inserted in the last two slots of the crate. The branch controller is connected to the computer and controls the slave controllers in each crate. There are various CAMAC branch controllers available in the market and also several custom implementations of the standard routines that are made available to the user as a set of functions in some programming language (generally FORTRAN, C, or C++). At MTBF the branch controller is a Jorway 411S connected to the SCSI port of the Linux PC. Fermilab has developed an implementation of the standard CAMAC routines called sjyLX [41]. It consists of a user level interface between the CAMAC IEEE routines and the Linux generic SCSI driver. The interface is in the form of C functions that can be accessed just by including the appropriate header files and linking with the sjyLX library during compilation. The implementation of the IEEE routines include functions to initialize and reset crates, to encode the addresses of modules, and most importantly, to execute CAMAC functions on a particular module. The way CAMAC modules integrate themselves in the standard is that they provide a table of functions that can be executed on them by the branch controller. Every function is identified by its F(function) and A(subaddress) codes, for example in the 7186 TDC, F(0)A(X) reads the event data memory for channel X+1, storing the result in a 16 bit variable

[5]Series or parallel depends on the crate controller used. At MTBF it is the Jorway 73A which is parallel.

provided to the routine executing the function. The libraries I wrote for the 7186 using the sjyLX library to interface with the Jorway 411S implement all the function codes and routines for initializing, testing, setting the control registers, and reading out the Phillips 7186 module. The implementation of the DAQ loop in C code is then very simple and self explanatory. The implementation of some of the routines (the most basic ones) is collected in Appendix A along with a very simple DAQ example and a Makefile for proper compilation of the example.

5.2.2 PP004 libraries

In the UTA Fast Timing proposal one of the future goals is to set up an MCP-PMT test stand at UTA with a pulsed laser. For this purpose we purchased the CAMAC PP004 branch controller that acts as a master for the DSP 6002 CAMAC crate controller [42]. The PP004 connects to a Windows PC via the EPP (Enhanced Parallel Port) and can control up to two DSP 6002 slave crate controllers. The PP004 comes with software that implements the CAMAC IEEE routines in its own custom way, different from the sjyLX library. It interfaces with the user via the dynamically linked library (DLL) PP-CAM32.DLL. The DLL has the routines already compiled for a Windows 32-bit machine. In order to use the routines the user needs to start a Micrsoft Visual Studio 2005 project, link it with the DLL, and copy the appropriate libraries in the project's directory. I wrote a template project file that includes the basic 7186 routines. This basic set of routines are sufficient since the more specialized features of the module are not likely to be used at the test stand. Details of the routines and how to use the DLL's along with a short, already tested, DAQ example source file are provided in Appendix A.

5.3 DAQ synchronized with tracking

In the synchronized version of the DAQ, the trigger is formed locally (inside the enclosure) with the same two scintillators as in the standalone case. The trigger is sent to the electronics room and distributed to the MWPC stations without requiring significant modification of the MWPC trigger logic. Since the trigger is formed locally, in a NIM crate right beside the movable table, it also needs to be vetoed there. Immediately after a trigger is formed further triggers need to be vetoed until the 3377's transfer the event data into the 4302 memory module and the Linux PC has finished reading out the event from the 7186. Also, when a 4302 memory module is 3/4 full the trigger must be vetoed until the Linux PC has fully readout all the 4302 memories in the MWPC stations. The hardware implementation of this logic is illustrated in Fig. 5.5, compare with Figs. 5.3 and 5.4. Notice that any of two veto counters can also veto the trigger. The veto counters are two L shaped scintillators that are brought together to form a rectangular shaped hole. The idea is to align the hole with the QUARTIC bars and veto data taking for particles in the beam that do not go through the hole.

With this approach to synchronization the tracking DAQ program does not need to be modified. The tracking DAQ has the possibility of writing a separate data file for each spill so I implemented the same approach for the data read out from the 7186 TDC. The end of spill signal is provided bye the Beams Division, this signal triggers an RFD02 LAM module which in response exerts a LAM (Look At Me) that is detected by the computer. So the MWPC program after reading out the memories closes the data file and starts a new one for the new spill. A copy of the Beams Division signal is sent to a second RFD02 LAM module and this one is polled by the 7186 DAQ (or timing DAQ). When the end of spill is detected the timing DAQ closes the file and opens a new one. From the point of view of the PC, synchronization is a matter of running the two DAQ processes at the same time. The number of events to take is given to the timing DAQ

process as a parameter. A bash (Linux shell) script was written to start the tracking DAQ in the background and then run the timing DAQ, passing the pid (process id) of the tracking DAQ as a parameter. After the desired number of events have been written to disk the timing DAQ process leaves the 2323 gate generator on, to inhibit any further events and then uses the pid of the tracking DAQ to send it an interrupt signal. The tracking process handles this signal and closes gracefully, reading out the 4302 memory modules one last time. For this scheme to work it was critical to rebuild the sjyLX libraries with the semaphores option. The sjyLX library interfaces with the Linux SCSI driver and by default only one process can talk to the driver at the same time. The semaphores option in compilation of the sjyLX library enables more than one process to access the routines at the same time. The source file for the timing DAQ process and the bash script that runs both processes at the same time are presented in Appendix B. See the example in Appendix A for the Makefile to build the executable. The script that starts the two processes at the same time also launches a start of run interface which was used in the March 2007 test beam running period to keep a database with information from all the runs.

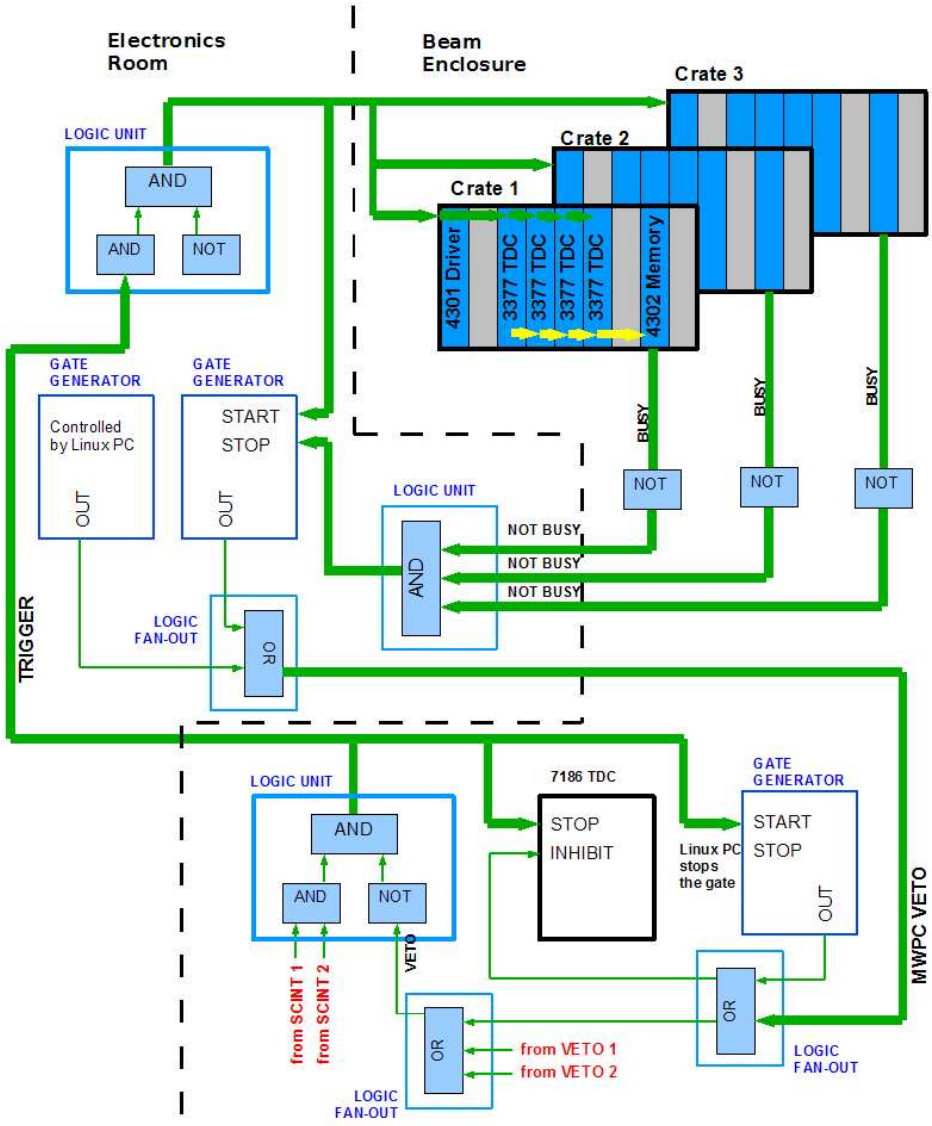

Figure 5.5. Synchronized DAQ trigger logic.

CHAPTER 6

ANALYSIS

6.1 Test Beam Run I

The test of the first prototype of the QUARTIC detector took place at the Meson Test Beam Facility over a period of a few weeks starting in mid-August 2006. I spent the Summer of 2006 at Fermilab learning about data acquisition systems and instrumentation to prepare for the running period. The first prototype consisted of four $21\times6\times6$ mm^3 fused silica bars inserted in an aluminized air light guide, see Section 4.3. Each bar was isolated and read out by a pixel of an 8 by 8 Burle 25 μm MCP-PMT[1]. The four bars were aligned in one row as shown in Fig. 6.1. The air light guide, fabricated by the Alberta group, was a single piece of plastic "printed" with a 3D plotter with holes for each of the bars. The interior of the light guides was lined with aluminized mylar. The final 20 mm section of the air light guides had a narrowing trapezoid to concentrate the light in the central region of the pixel. In Run I we also tested the GASTOF detector constructed by UC Louvain which uses uses C_4F_{10} or C_4F_8O gas as a radiator. The single-channel GASTOF detector, Fig. 6.2, is about 30 cm long; this is required to compensate for the lower index of refraction of gas compound to generate enough Cherenkov photons. The electronics that we had in this run were 6 custom-made (UC Louvain) amplifier boards (Phillips BGA2712 chip), 2 Hamamatsu preamplifiers, 2 Ortec 9306 (1 GHz) preamplifiers [43], 2 Ortec 934 CFD NIM units with four channels each, and an Ortec 9307 pico-TIMING CFD [44]. The setup consisted of two GASTOF counters followed by two QUARTIC counters, as can be seen in Fig. 6.3. The high voltage was supplied from

[1]Towards the end of the run we changed one of the tubes for a Burle 10 μm tube.

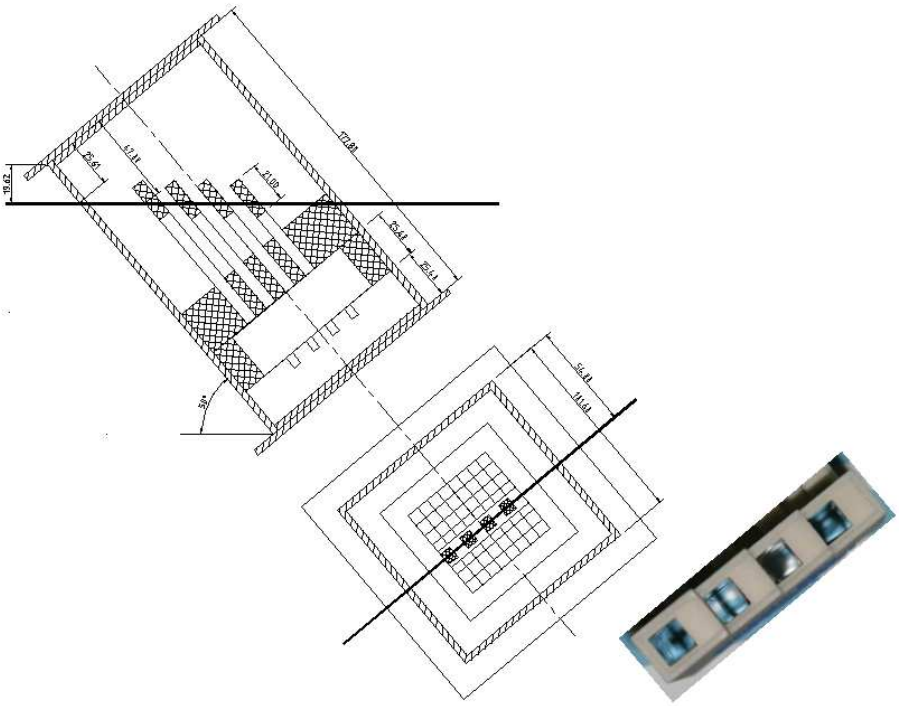

Figure 6.1. QUARTIC first prototype.
The lower right image shows a top view of the air light guide.

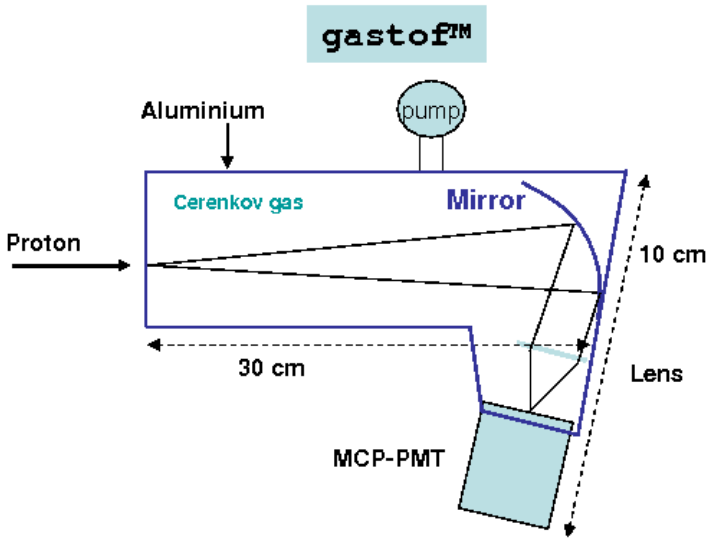

Figure 6.2. Schematic of GASTOF.

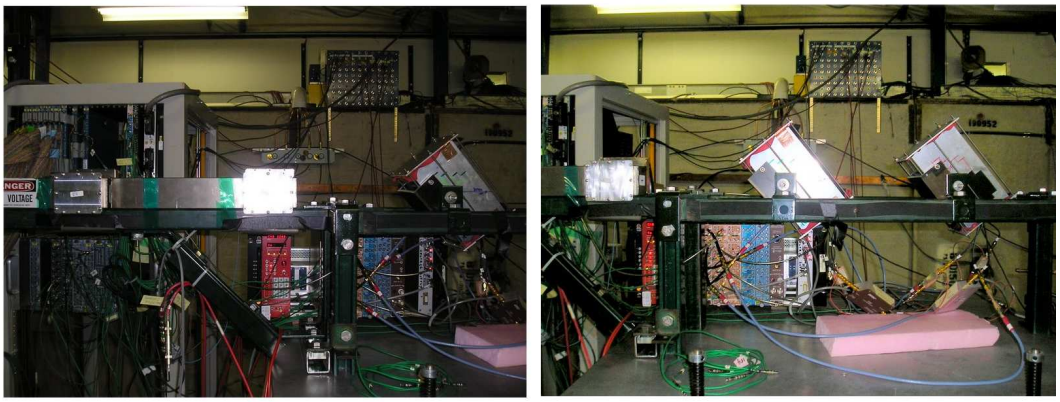

Figure 6.3. Setup in the beamline. Two GASTOF counters (left) and two QUARTIC counters (right).

within the control room although at the end of the running period we switched to local control. A NIM crate with the CFD modules was mounted on the movable table with the detectors to keep the length of the cables to the CFD's as short as possible. The CAMAC crate with the TDC was beside the table on a rack, see Fig. 6.3, also with the NIM crate that had the trigger logic units.

Run I was mostly a learning experience. At the time of the run the standalone DAQ was developed but not fully tested and we only achieved synchronization for a few runs at the end of the running period. The track reconstruction software was not developed yet also. The goal of this run was to achieve a not so bad time resolution considering that we were using the off-the-shelf Ortec 934 CFD, which is not particularly adapted for MCP-PMT pulses. We only had one channel of the more expensive Ortec 9307 which is recommended for MCP-PMT pulse rise times. The Ortec 934 is considerably difficult to tune because if offers the possibility of adjusting the zero crossing level (this parameter is referred to as the walk). This is used to correct for non-linearity of the pulses when the zero-crossing amplitude independence might not apply exactly. We observed that a badly tuned 934 ruins significantly the time resolution, sometimes even observing two

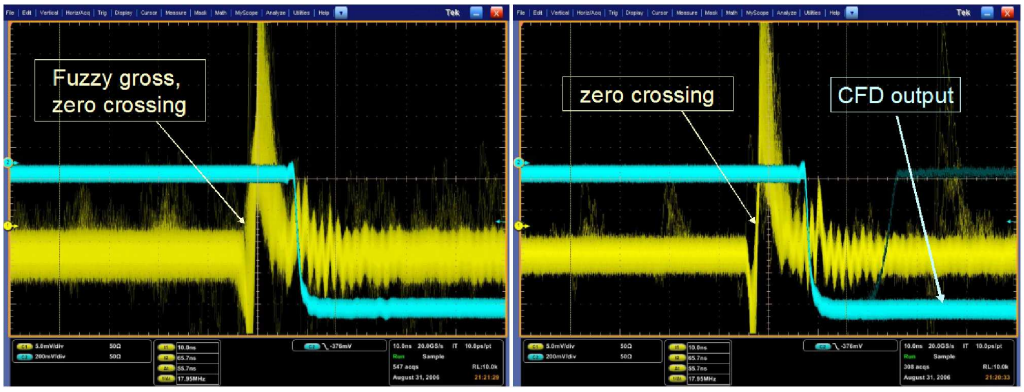

Figure 6.4. Tuning the 934 CFD.

distinct peaks in the distribution of times. Swapping the 934 for an Ortec9307, with no other changes, restored the single peak. To tune the 934 for optimum walk reduction, an actual detector signal has to be connected to the input. The 934 has a monitor signal, which is a copy of the input to the zero crossover comparator. While triggering on the output we set the walk adjust so that all monitor signals crossed the walk level at the same time, see Fig. 6.4. We tuned the 934 using the noise signals of the MCP-PMT that are produced by amplified thermal electrons that are emitted by the photocathode. This tunes the 934 for the single amplified electron case[2].

The alignment of the detectors in the beam was an issue that took more than a week of running to resolve completely. There was no clear reference as to where the beam was and we had to do thorough vertical and horizontal scans with the movable table (which we had to calibrate also) to locate it and optimize the position of the detectors. For the second run (March 2007) this was a lot easier because a laser alignment system was installed at MTBF that helps locate the position of the beam at any z location and a new interface with auto-calibration was installed to control the motion of the table. Even when using the laser in Run II, we found later with tracking that the bars were not

[2]Based on simulations presented in Chapter 4 we expect 5 photoelectrons from the passage of one proton through a QUARTIC bar

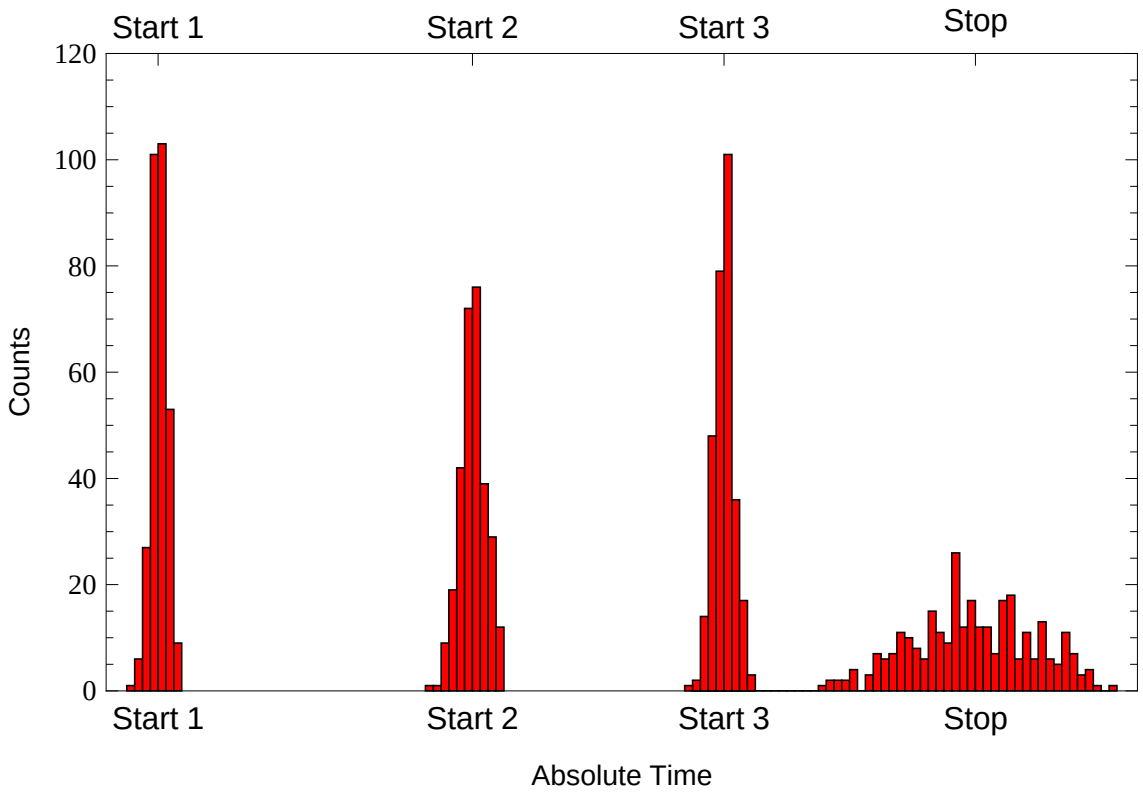

Figure 6.5. Arrival of signals to TDC in an absolute time frame..

always aligned with the central 1 cm^2 region of the beam, where almost 90% of the beam particles are concentrated. For the upcoming run of July 2007 we will be in a position to align the detectors with the beam using the facility's lasers and then fine tune the position of the bars with corrections from tracking, all in the first day of the running period.

6.1.1 Timing analysis

Unlike a laser setup or the actual LHC experiment, we don't have a low jitter signal to use as the TDC stop. In an absolute time frame the arrival of the signals to the TDC in our setup is shown in Fig. 6.5; in the perfect timing scenario all the counts would be localized as delta functions at the START and STOP times. The STOP is provided by

the coincidence of two scintillator paddles[3] in the beam and exhibits a considerable jitter $\gtrsim$1 ns. On the other hand the detectors we are testing have a resolution of the order of $\lesssim$100 ps and so in the absolute time frame this looks like a more peaked distribution. What we want to measure is the σ for each of the START distributions in the absolute time frame, as obtained when fitting the distribution with a Gaussian curve. We refer to this as the individual counter resolution. The TDC measures the difference between the common STOP and the individual channel STARTs. For event n, channel i, this is

$$T_i = \text{STOP}_n - \text{START}_i$$

The statistical variation of the start and the stop can be emphasized by writing

$$\text{STOP}_n = t_{\text{STOP}} + X_n$$

$$\text{START}_i = t_{\text{START},i} + I_i$$

where t_{STOP} and $t_{\text{START},i}$ are constants and X_n is a random variable that represents the jitter of the stop and has zero mean. I_i represents the jitter of the detectors, hence the individual counter resolution, and also has zero mean. If we had a low jitter stop then we could approximate $\text{Var}(X_n) \approx 0$ and a fit of the raw TDC counts distribution would give us the individual counter resolution,

$$\Rightarrow \sigma_i^2 = \text{Var}(I_i) \approx \text{Var}(T_i).$$

The constant times $t_{\text{START},i}$ and t_{STOP} depend on the separation along z of the start and stop detectors, and the time delays introduced by cable length and by the electronics in each of the paths. In an experiment, where the time measurement is used to determine another physical quantity (e.g. the interaction vertex in FP420 or the velocity of the particle in particle ID) the actual value of $t_{\text{START},i}$ and t_{STOP} is of no importance. A

[3]For part of Run I this coincidence also included a logical OR of some of the TOF counter signals.

calibration must be performed to find the conversion scale between the TDC values and the physical quantity to be determined, and it is not necessary to determine exact cable delays or delays introduced by the electronics, which remain constant throughout. The calibration is performed using a set of events for which the physical quantity of interest is already known by other methods or can be assumed to have a fixed value under certain conditions. At FP420 the calibration of the $t_L - t_R$ time difference will be done by considering [pXp] (pile-up background) events where X is any central system with a vertex narrowly defined by the central tracker.

6.1.1.1 Multiple counters along the beam

If one has two or more detectors along the beam but needs only one time measurement, the resolution can be improved by combining the measurements. A conversion scale between the desired physical quantity and the average $(T_1 + T_2)/2$ can be determined, and the experimental uncertainty using the average of the two measurements will be better because $\mathrm{Var}[(T_1 + T_2)/2]$ is less than $\mathrm{Var}(I_i)$. Assuming T_1 and T_2 are Gaussian with the same individual counter resolution, σ, then $\sigma_{\mathrm{avg}} = \sigma/\sqrt{2}$. If one has N identical counters along the beam a $\sqrt{N}$ improvement in the resolution can be achieved by considering all the independent measurements.

While we were discussing the way to obtain the best time measurement with information from several counters along the beam, Mike Albrow suggested the analogy between our timing setup which has several time measurements along z and a tracking device, which has several x, y measurements along z. In the tracking case one uses a least squares minimization procedure to find the parameters of the track which are x_0, y_0 and the slopes $dx/dz, dy/dz$. In the timing one has only one parameter to fit for, the time t_0, at a nominal point z_0. Assuming the speed of the particle is the speed of light throughout the track, the time predicted (tp) at the detectors is related to t_0 by a constant shift,

$tp_i = t_0 + C_i$. One sets up a likelihood function with the difference between measured (tm) and predicted times, weighted according to the quality of each measurement (w_i, could be a function of the individual counter resolution for example),

$$M(t_0) = \sum_{i=1}^{N} w_i (tp_i - tm_i)^2$$

Minimizing this with respect to t_0 one obtains it's most likely value.

$$\frac{\partial M}{\partial t_0} = 0$$

which gives the simple answer

$$t_0 = \frac{\sum_{i=1}^{N} w_i tm_i}{\sum_{i=1}^{N} w_i} - \frac{\sum_{i=1}^{N} w_i C_i}{\sum_{i=1}^{N} w_i}$$

The second term is a constant and will just produce a shift in the calibration scale when the t_0 values are calibrated with respect to another physical quantity. Defining t_{avg} as a normalized weighted average of the measured times,

$$t_{\text{avg}} = a_1 tm_1 + a_2 tm_2 + \ldots \quad \text{with} \quad a_1 + a_2 + \ldots = 1,$$

is thus equivalent to performing a least squares fit of the measured times, the calibration scale is shifted but not scaled by a factor, so the improvement on the resolution obtained by having several counters can be assessed by direct comparison of σ_{avg} and σ_i, the resolution of the individual counters. If one counter is known to be better than the others the coefficients of the weighted average can reflect this fact to obtain the best improvement on the resolution. A simple approach is to set the coefficient to be in the same ratio as the inverse of the measured individual counter resolutions for the counters on the beam line, that is $a_1 : 1/\sigma_1$ equal to $a_2 : 1/\sigma_2$, etc. In this case

$$\sigma_{\text{avg}} = \sqrt{N} \left(\frac{1}{\sigma_1} + \frac{1}{\sigma_2} + \ldots \right)^{-1}$$

recovering the $1/\sqrt{N}$ improvement factor when all the counters are identical.

The remarks above apply equally when there is an very precise time reference ($\mathrm{Var}(X_n) \approx 0$), as above, and in our setup where the stop is provided by a scintillator and $\mathrm{Var}(X) \gg \mathrm{Var}(I)$. In the latter case one subtracts the raw TDC values for two channels canceling out the jitter of the stop,

$$\mathrm{diff}_{i,j} = T_i - T_j.$$

If the counters can be assumed to be independent, then $\sigma^2_{\mathrm{diff}} = \sigma_i^2 + \sigma_j^2$. With several counters along the beam the $\sqrt{N}$ improvement in the resolution can be studied. One can take a weighted average of a set of counters and subtract it from a weighted average of another set of counters to cancel the effects of the stop, and shifting but not scaling the calibration scale. For example

$$\Delta = \frac{a_1 T_1 + a_2 T_2}{a_1 + a_2} - \frac{a_3 T_3 + a_4 T_4}{a_3 + a_4}$$

and σ_Δ can be compared to σ_{diff} to assess resolution improvement, since the weighted averages are normalized.

6.1.1.2 Individual counter resolution and height correction

From the measured values of σ_{diff} for all possible pairs, the individual counter resolutions can be fitted if four or more counters are available. Assuming the counters are independent from each other, a difference resolution can be predicted by

$$\sigma^2_{\mathrm{diff}_{ij}} = \sigma_i^2 + \sigma_j^2$$

The sum of the squares of the predicted minus measured differences is minimized to obtain the individual resolutions that best approximate the measured σ_{diff}'s. However, the counters are not all independent. There is a correlation between QUARTIC counters

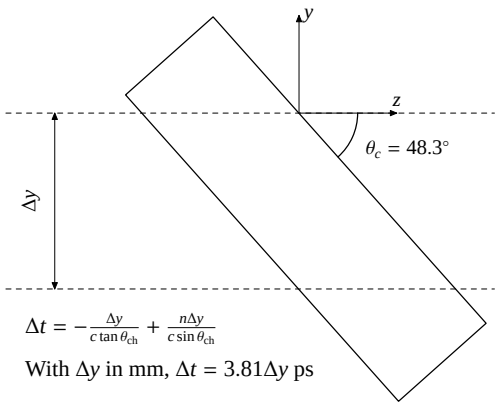

Figure 6.6. Height correction for QUARTIC times..

because the time measured depends on the height of the proton track, and this variation is the same for al bars in each event. With the height of the track, Δy, in mm the correction is $\Delta t = (3.81 \cdot \Delta y)$ ps, see Fig. 6.6. There is also some dependance on the height for the GASTOF measurement, but it is expected to be less significant. If a fit is made using measured differences between only QUARTIC bars then the times can be assumed independent because all have the same correlation, so this component of the resolution cancels out. When fitting differences of GASTOF's and QUARTIC's the correlation can be included as an additional parameter of the fit.

6.1.2 Time resolution results

The best difference resolution obtained with the QUARTICs was between Q15 (QUARTIC # 1, bar # 5) and Q23[4] of 128 ps. This result was with an Ortec9306-9307 combination on Q15 at 2300 V and an Ortec9306-934 on Q23 at 2300 V. We obtained better results with QUARTIC bars that had the Ortec 9306 preamplifiers than with bars that had Phillips preamplifiers, the same was observed for the 9307 over the 934 CFD. Fitting the measured differences to obtain the individual counter resolutions we were

[4]The instrumented bars in each QUARTIC were 1,3,5,7.

Table 6.1. Results of fitting the measured difference resolutions

Detector	Individual Resolution	
	Before	After
G1	107±9 ps	105±5 ps
G2	75±15 ps	63±10 ps
Q15	189±10 ps	170±7 ps
Q23	175±5 ps	107±5 ps

able to estimate the improvement achieved by using the 9307 CFD over the 934 CFD for QUARTIC bar pulses. Taking the resolutions measured for the two configurations shown below,

Before	After
G1 → 6dB + Hamamatsu → Ortec 934 → TDC 11	G1 → 6dB + Hamamatsu → Ortec 934 → TDC 11
G2 → 6dB + Hamamatsu → Ortec 934 → TDC 12	G2 → 6dB + Hamamatsu → Ortec 934 → TDC 12
Q15 → 6dB + Phillips → Ortec 934 → TDC 6	Q15 → 6dB + Phillips → Ortec 934 → TDC 6
Q23 → 6dB + Ortec9306 → Ortec 934→ TDC 14	Q23 → 6dB + Ortec9306 → Ortec 9307→ TDC 14

where in both columns all the PMT's were at 2300 V, the fitted detector resolutions obtained are shown in Table 6.1

Changing the 934 CFD for the 9307 improves the individual counter resolution of Q23 from 175 ps to 107 ps, which implies that all other QUARTIC channels were dominated by this 934 resolution component. The average difference resolution between pairs of QUARTIC bars (both bars with the 934 CFD) at different voltages is shown in Fig.6.7. At 2500 V the average value $\sigma = 164$ ps, assuming the bars are equal, gives us an average individual counter resolution of 115 ps. The resolution component introduced by the electronics in one channel can be estimated from the simulation results of Section 4.3. There we obtained an estimate of 73 ps for the resolution of one detector channel with

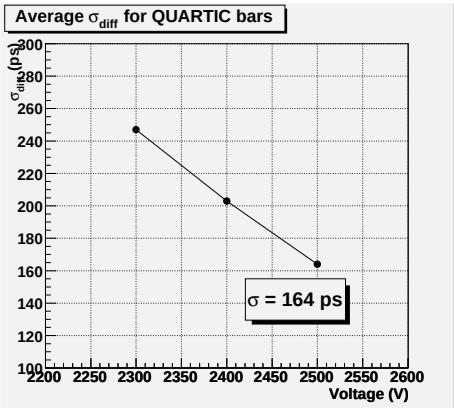

Figure 6.7. Average of the difference resolution for QUARTIC bars at different voltages using the Ortec 934 CFD..

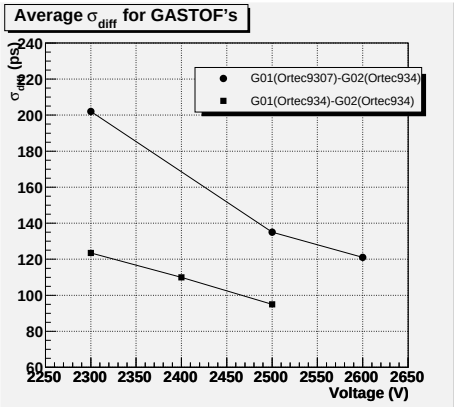

Figure 6.8. Resolution of the difference G01−G02 for different HV's.

the Burle 25 μm, which gives a value of $\sqrt{115^2 - 74^2} = 89$ ps for the average resolution of the electronics in one counter.

The observed resolution of the GASTOF counters was better than that of the QUARTIC's, see Fig. 6.8. The difference resolution improved as voltage on the PMT was raised, the best result obtained was 93 ps at 2500 V. Assuming identical counters this gives 65 ps for each GASTOF in the best case, consistent with the individual resolution obtained by fitting the mixed differences quoted in Table 6.1. The resolution was affected significantly when we changed the 934 CFD for the 9307 CFD on the GASTOF01 counter,

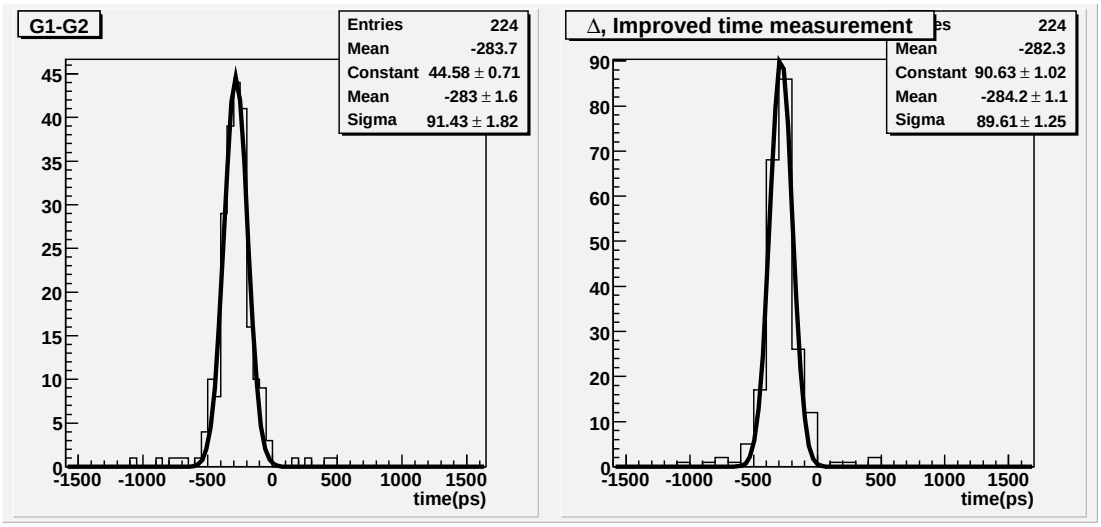

Figure 6.9. $T_{\mathrm{G1}} - T_{\mathrm{G2}}$ (left) and $\Delta = T_{\mathrm{G1}} - [(0.996) \cdot T_{\mathrm{G2}} + (0.004) \cdot T_{\mathrm{Q23}}]$ (right).

and unlike the QUARTIC, the GASTOF performed better with the Ortec 934. The MCP-PMT in the GASTOFs is a 2 by 2 pixel Burle 25 μm in which the outputs of the 4 anodes are ganged together to form a single channel output. We found in Run II that this affects the shape of the output pulse considerably, see Fig. 6.26. It is plausible that a longer risetime of the pulses makes the Ortec 934 more appropriate than the 9307 to time them.

The resolution of the G1−G2 difference can be improved using the time measurement from the QUARTIC bars along the beam. For the best difference resolution of 93 ps between GASTOFs at 2500 V the information from the QUARTIC's does not improve the resolution very much, see Fig. 6.9, only from 92 ps to 89 ps. For the improvement to be considerable the detectors need to have comparable individual resolutions, or else have more counters along the beam. At 2300 V, with Q23 connected to the 9307 discriminator for better resolution and using a total of four QUARTIC bars the resolution can be improved significantly, from 136 ps to 96 ps, see Fig. 6.10.

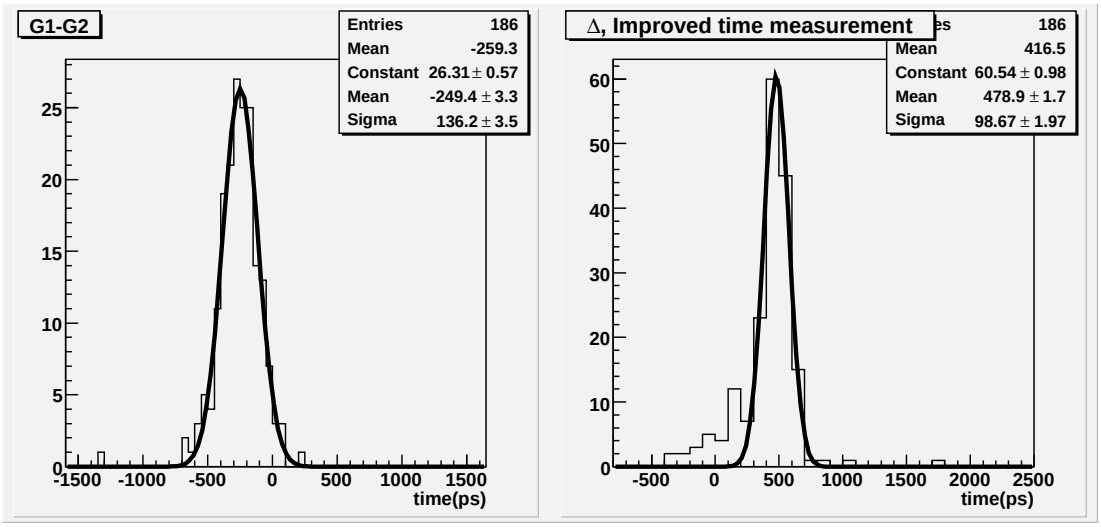

Figure 6.10. $T_{G1} - T_{G2}$ (left) and $\Delta = [(.81) \cdot T_{G1} + (.12) \cdot T_{Q23} + (.07) \cdot T_{Q11}] - [(.75) \cdot T_{G2} + (.13) \cdot T_{Q15} + (.12) \cdot T_{Q25}]$ (right).

6.1.3 Efficiency results

The efficiency was measured by counting the fraction of times a bar was on with a valid time when other bars were on as well. Since the GASTOF counters had a larger area, high efficiency and a more reliable alignment, they were required to be on as well. The efficiency for bar 5 in QUARTIC 1, for example, was measured as [# of Q15 good] out of events with [(G1 OR G2) AND Q1X], Q1X meaning at least one of the other bars in Q1 is on, to ensure the proton went through the instrumented row. The bars in the other QUARTIC are not taken into account because the two QUARTIC's were not perfectly aligned. The bar efficiencies are shown in Fig. 6.11. A variation from bar to bar is observed where the more efficient bars are the ones that have a shorter light guide. For some events we fail to get a correct time not due to inefficiency of the detector but to overflow of the TDC counts. This happened in this initial run because the triggers to the TDC were vetoed (or very restrictive in case one of the detectors is part of the trigger coincidence) but the front end continued receiving signals all the time since it was not inhibited. During the time interval when the front end is not inhibited, if it

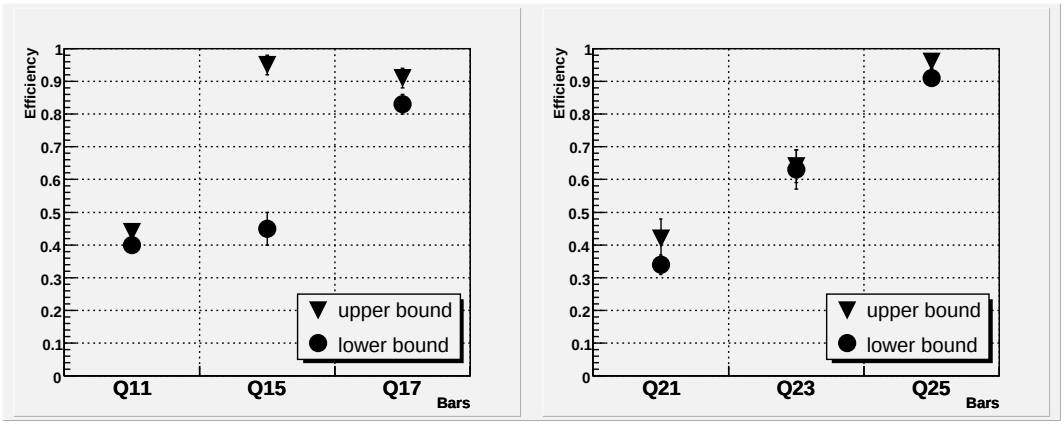

Figure 6.11. Efficiency of the QUARTIC bars..

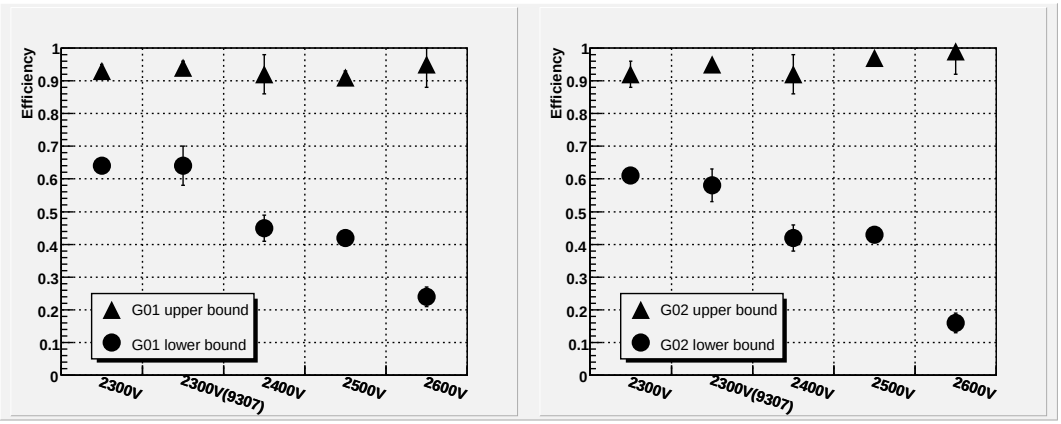

Figure 6.12. Efficiency of the GASTOF detectors..

receives a start but not a stop then it will start counting. When a good start-stop pair arrives later the TDC will register an overflow value in memory. This overflow issue was better addressed for Run II adn the setup described in Section 5.2 reduced the overflow fraction significantly. An upper bound of the efficiency includes the overflow values in the numerator. The efficiency of the GASTOF counters was measured as [# of G good] out of events with [Q1X AND Q2X]. The results are in Fig. 6.12. For the GASTOF's the efficiency apparently decreases with increasing voltages presumably because there is more noise causing an increase in overflows. The upper bound, however, remains constant

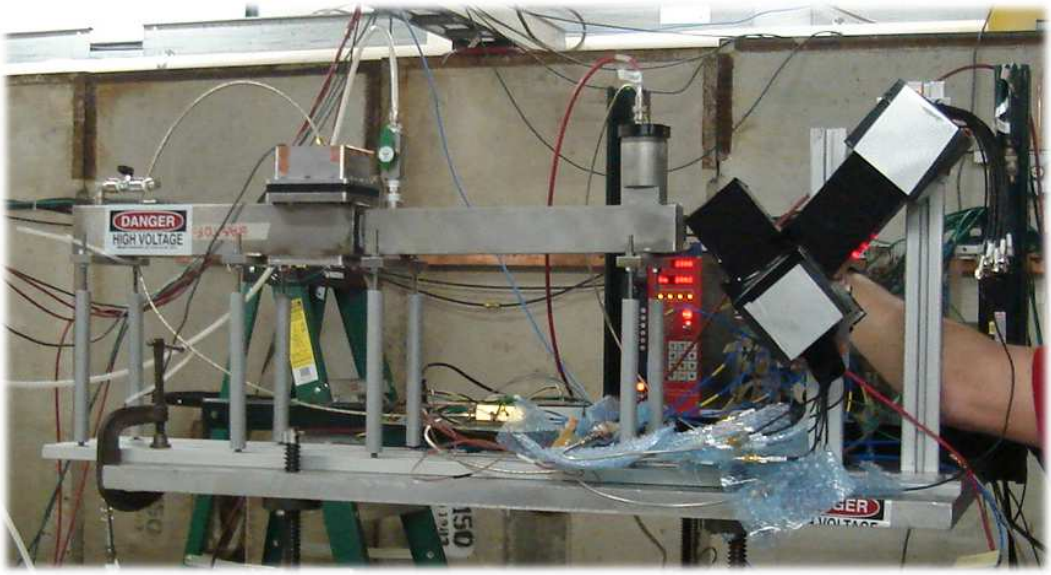

Figure 6.13. Setup of the detectors on the movable table for Run II.

independent of the applied voltage and is likely a more accurate representation of the efficiency.

6.2 Test Beam Run II

In Run II, which took place March 7-21 of 2007, we made a test of the second prototype of the QUARTIC detector. The QUARTIC2 prototype was built with 15 mm-long fused silica bars in a new mounting designed and constructed at Fermilab, that made alignment with the beam an easier task. The bars were read out by a Burle 10 μm MCP-PMT. The mounting provided space for two detectors with the bars at the Chrerenkov angle as shown in Fig. 6.13. We also had one of the first prototype GASTOF detectors and a new GASTOF2 prototype with an upgraded spherical mirror, a 6 μm Hamamatsu MCP-PMT, and a the fast non-inverting Mini-Circuits ZX-60 amplifier. We aligned the QUARTIC detectors using the laser guides installed at the MTBF facility but after the run found using tracking that this alignment was off by about 5 mm. At the time of Run

II the tracking analysis software was not completely developed. To have the tracking package available for analysis of the Run II data I followed up on a previous effort by UC Louvain and undertook the task of completing the code. I found some problems with the algorithm that they were developing and had to start working on the tracking using a different approach. Unfortunately there was not enough time to finish it before the running period was over and the analysis of the data with tracking was not done online but in the weeks following the end of the run. Our motivation for the third run in July 2007 is that the tracking solution is available and will give us quick feedback as we take data.

The main goal for Run II was to improve the timing performance of our detectors while using custom-made electronics that would reduce the cost per channel. We tested the custom-made LCFD (Louvain CFD) constant fraction discriminator NIM module (see Section 4.4). The LCFD provides the possibility of remotely controlling the thresholds by connecting the unit to the COM port of a computer in the control room, using a long cable that runs from the beam enclosure. The LCFD behaved as expected and we were able to achieve a better resolution with it, however the data we took in this run revealed several systematic problems with our detector. The main one being the evidence of cross-talk between the different channels of the MCP-PMT which appeared as a later time signal (coherent noise) present in one or more of the bars in a QUARTIC row for tracks that did not go through the row. At the beginning of the run we were preparing to test a single row QUARTIC readout and we would then consider the possibility of reading out another row and then another detector. With this in mind we instrumented more that one row from the beginning which made it possible that light generated in the adjacent row would produce a coherent noise signal on the row that we were reading out. The three rows that were instrumented were labeled QF (90mm bars), QE (12mm bars) and QB (15mm bars) which corresponded to rows 3,4,5 respectively of the 8 by

Figure 6.14. One bar gets a valid signal (yellow) and both pads in the anode ring about 2 ns later (yellow and blue)..

8 pixel MCP-PMT. We read out row QB. After the first week of running, observing the double peaks in the time distributions we had a reason to believe there was some kind of coherent noise in the tube. This was verified using the fast oscilloscope, see Fig 6.14. We changed the horizontal position of the detectors by +6 mm and +12 mm, and observed the coherent noise reduced. After the run, when the tracking analysis package was completed we found that for most of the running period we were taking data with the center of the beam spot on row QE, thus maximizing the possibility of coherent noise.

Another goal of Run II was to study the raw output pulses of the MCP-PMT. For this purpose we used a remote controlled fast oscilloscope[5] to record the pulse shape information and study a possible optimization of the attenuation and delay of the custom

[5]The Tektronix DPO 70404 with 4 GHz bandwidth.

made CFD units. The signals from the MCP-PMT's were connected to the oscilloscope which was in the beam enclosure and we remotely controlled the scope interface to save the pulse waveforms. In this way we collected waveforms for both Hamamatsu and Burle pulses. The idea is to analyze the average behavior of the pulses to optimize the design of the electronics, i.e. amplification and CFD parameters: delay and attenuation. This analysis is currently in progress by Tomasz Pierzchala of UC Louvain.

6.2.1 Tracking analysis algorithm

The tracking program analyzes the hits in a user defined number of MWPC stations located along the beam. Each station consists of four to six planes, see Fig. 6.15, with each plane measuring a coordinate x,y, u, or v. The planes are labeled X,Y,X',Y',U, and V [6]. At MTBF every wire is read out by a TDC channel which is common stopped by the event trigger. For a real track going through, the time of the wire hit is fixed with respect to the stop time. A time window is defined for every TDC in the wire chamber system to remove noise hits almost totally by making a cut on the TDC times. To obtain the time window all the times for each TDC are plotted in a histogram and the real track peak is readily identified.

Two approaches were tested for the tracking solution, at the end the results not being drastically different. The one we implemented first was a global fit where the information from all the planes in the four tracking stations was included in a single least squares fit of the most probable track parameters (x_0,y_0,dx/dz,dy/dz). Each plane measures a coordinate (x,y,u, or v) at a fixed z so the alignment in this case was done by shifting the planes so that the mean of the measured coordinate in each plane equals zero, effectively setting $x = 0, y = 0$ at the center of the beam spot. The algorithm was combinatoric, it started with the set of hits of an event and then considered all

[6] In the program's source code X'≡x (lowercase x).

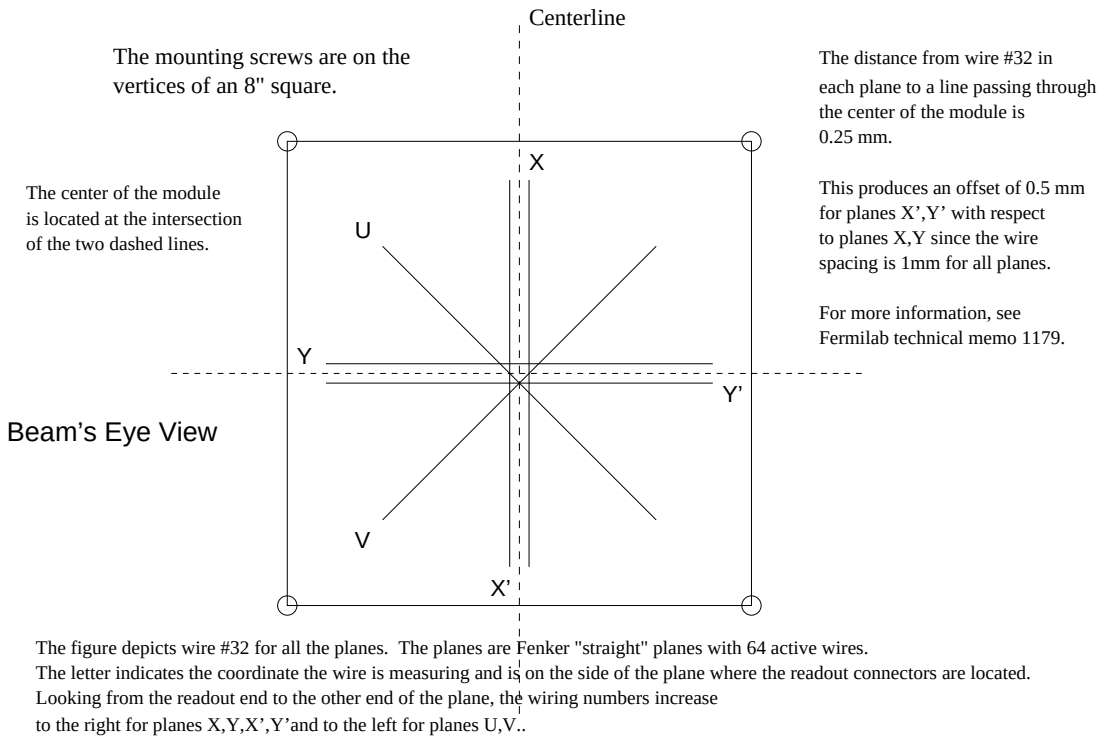

Figure 6.15. Orientation of the planes in an MWPC station.

possible combinations of 22 hits to try and fit a track[7], if it does not successfully find a track then it will try all possible combinations of 21 hits and so on. The value of the likelihood parameter to estimate the goodness of the fit and accept fit candidates was obtained empirically by observing the distribution of the minimized least squares functional for a broad set of events. The distribution is not exactly a χ^2 distribution since the measurement errors tend to be uniform (instead of gaussian) in a MWPC. The drawback of this method is that it is very time consuming to try all possible combinations, because the number of calculations increases factorially. In practice we started trying from combinations of 8 hits then 7 etc., to reduce running time of the program and because the MTBF's tracking stations very rarely produce a perfect event with all 22

[7]Most of the events have more than one hit per plane, only one or two hits at most being associated with the track, the others are noise.

planes. An average of 6-9 planes has the correct coordinate in an event, more hits can be present but they are generally found by the combinatorics to be noise hits.

The second approach, more complicated from a programming perspective, is to first obtain a point for each of the MWPC stations by fitting the hits in the station's planes, using combinatorics to explore the possible combination of wires that determine a point within a station. The points for the stations are then fitted to a line to obtain a track. The planes within a station are assumed to be all at equal z and the fit parameters are only x and y. For the track fit, the track is assumed to be a straight line (no magnetic field) with parameters x_0,y_0,dx/dz,dy/dz. The advantage of this method is that the station points obtained this way are very reliable because the systematic error in the calibration of the planes within a station is low, compared to the error introduced when calibrating a plain in station 1 with respect to a plane in station 4, for example, which are 14 m apart in z. The drawback is that the efficiency is reduced drastically because events with 3 or more fitted station points are not that frequent and a track is not always obtained. In this approach the plane and station x, y positions are calibrated with data. The z positions are available from Fermilab survey information. The calibration of the planes within a station is done by taking the X and Y planes as base planes. Plane X' is calibrated by selecting events that have single hits in X' and X and histogramming the difference in the measured coordinates, $x_{\mathrm{X}} - x_{\mathrm{X}'}$. The mean of this histogram gives the shift that needs to be applied to x coordinates measured with plane X'. For plane U, events are selected that have single hits in U, X, and Y. The coordinate u is predicted from as X and Y as $u_{\mathrm{p}} = (x_{\mathrm{X}} - y_{\mathrm{Y}})/\sqrt{2}$ and compared with the measured u_{U}. The predicted minus measured difference, $u_{\mathrm{p}} - u_{\mathrm{U}}$, is histogrammed and the mean of this histogram is the shift of measurements done by the U plane. The Y' and V planes are treated in a similar way. In order to understand the behavior of the MWPC's with real data, I wrote an event display program with a graphical user interface, see Fig. 6.16,

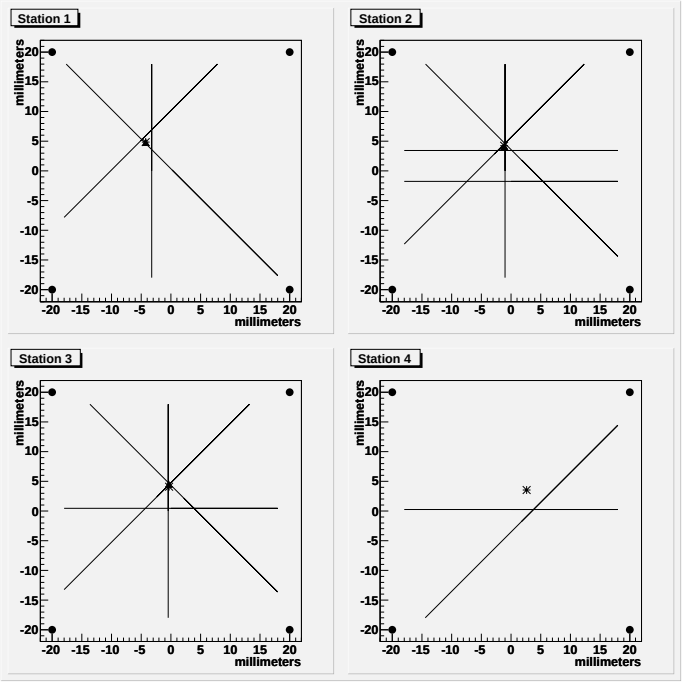

Figure 6.16. Example of a tracking event as seen on the event display.

that shows the wires that were hit and the points fitted for each station. If a track is determined for the event the extrapolated point at each of the stations is also shown. Using the event display is a very simple method of determining the performance of the individual stations, or if there are noise issues –for example a single wire that fires with a high frequency. In Run II we obtained a set of 45000 tracking events synchronized with the TDC data from our detector and this set was used as the calibration set. The histograms obtained for calibration of the planes in each station are shown in Fig. 6.17. The first step in the calibration procedure used to calibrate the station positions is to selec two reference stations for which the x and y offsets will be zero. Using the event display we determined that stations 1, 2, and 3 are the ones that produce the best points and selected stations 2 and 3 as the reference stations. Events are selected that have a point in the reference stations and a point in at least one of the other stations. The slope of the track is calculated with the points in the reference stations and the predicted

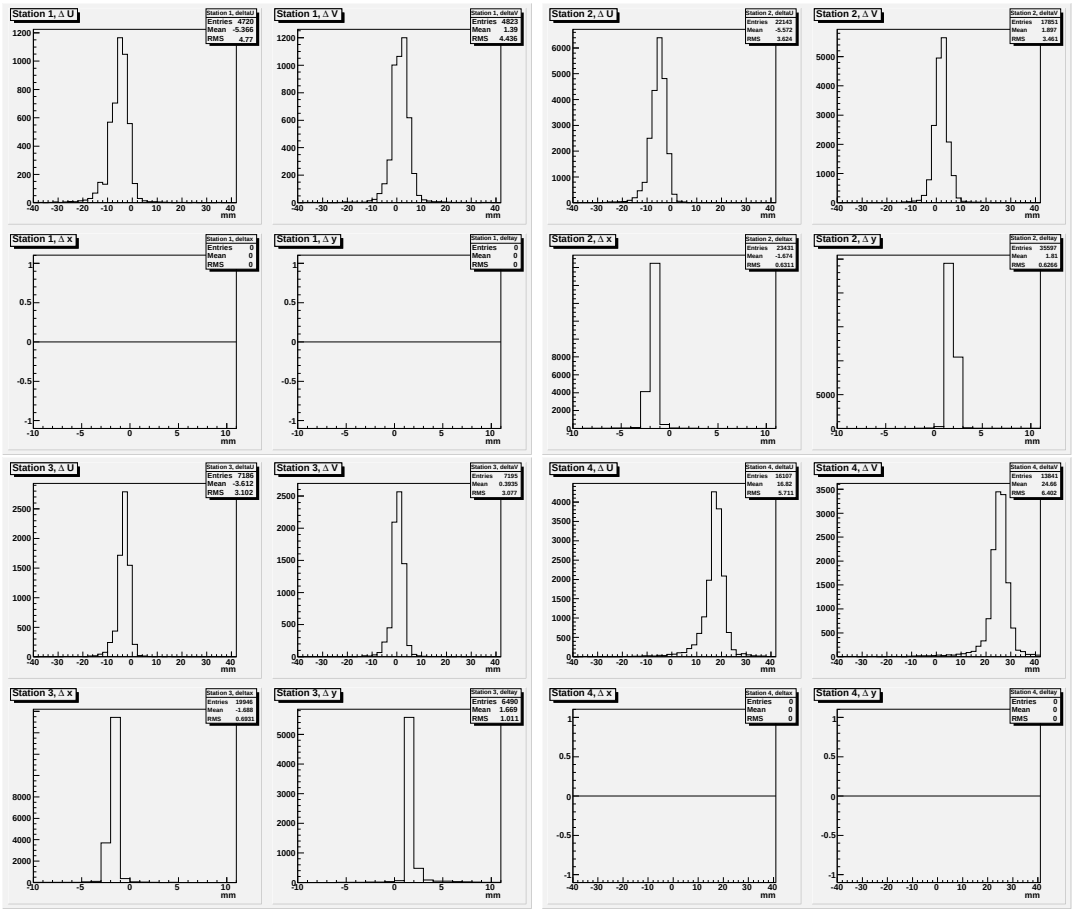

Figure 6.17. Plane calibration histograms (1 mm per bin), stations 1 and 4 do not have X' Y' planes..

minus measured x and y differences are histogrammed for the other stations. The mean of these histograms are the station's x, y shifts. The histograms obtained for calibration of the station positions are shown in Fig. 6.18. As seen in the plots, the calibration showed us that station 4 is very unreliable so for the construction of the points we used only information from stations 1, 2, and 3, fitting a line to form a track when three points were available. This proved to have very low efficiency because the tracks did not typyically have three points.

A planned improvement for the tracking analysis software is to merge the two approaches to take advantage of both of them. First a fit would be attempted using

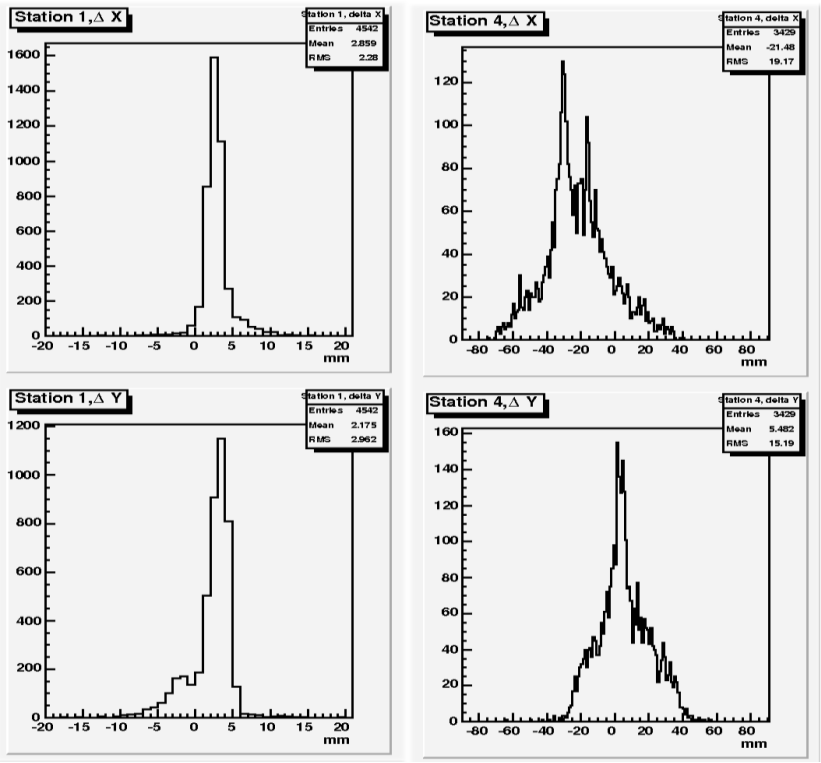

Figure 6.18. Station calibration histograms (1mm per bin).

the second approach with station points and if this were to fail a more time consuming global fit would be tried, thus increasing the efficiency of the tracking algorithm. An implementation of this procedure is currently underway.

6.2.2 Run II Analysis and Results

The main analysis of the Run II data used the 45000 events synchronized with tracking to understand the coherent noise we observed. By looking at a scatter plot of the raw times of two different channels one can see the effect of the jitter of the common stop and the presence of coherent noise. Figure 6.19 shows the coherent noise between two adjacent bars QBB and QBC (The second letter is the row and the third letter is the bar) and two non-adjacent bars QBB and QBE. The four spots indicate that there are two time peaks for each channel. The early time peak (top right) for both channels

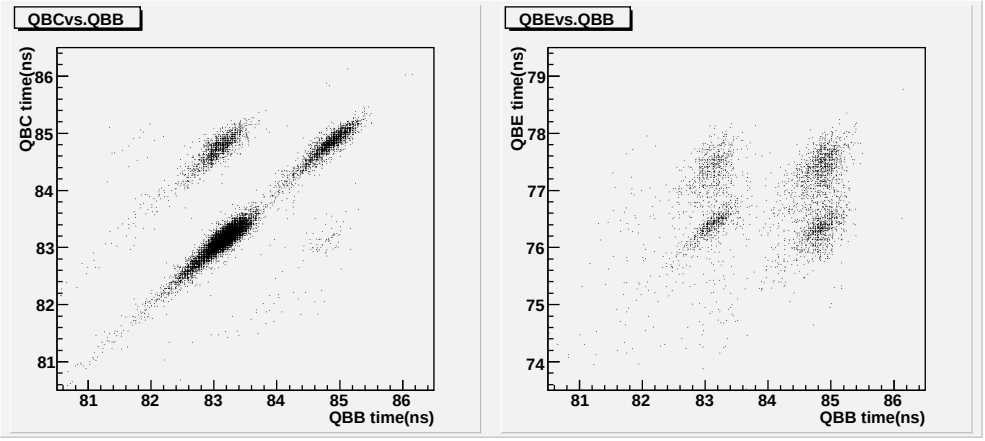

Figure 6.19. Adjacent pixels (left), and non-adjacent pixels scatter plot (right).

is the signal[8] A noise time can be produced in an inefficient channel by a proton that goes through the row and generates light in an adjacent bar. We think that adjacent pixel crosstalk is the reason that the adjacent bars QBB and QBC (left) show a higher correlation than the non-adjacent pair QBB, QBE. We plan to gain more understanding of this in the next Test Beam Run.

We took data synchronized with tracking in three table positions, +0 mm (21000 events), +6 mm (9000 events), and +12 mm (15000 events). The beam spot in x is mostly localized in a 10 mm region as shown in Fig. 6.20, and to see the profiles of the QUARTIC bars in the beam we plot the bin fraction, which considers bin by bin of the beam's x profile histogram and gets the fraction of the tracks in the bin that had signal times in one or more QUARTIC bars in the row being read out (row QB). To assign a time as signal or noise we use the GASTOF detector, which is free of coherent noise, as a reference. A scatter plot of GASTOF times vs. QUARTIC bar times, see Fig. 6.21, permits the identification of signal and noise times which would otherwise would be obsucred by the jitter of the common stop. We plot the bin fraction for tracks with

[8]The TDC is in common stop mode so larger TDC times mean earlier absolute time frame times.

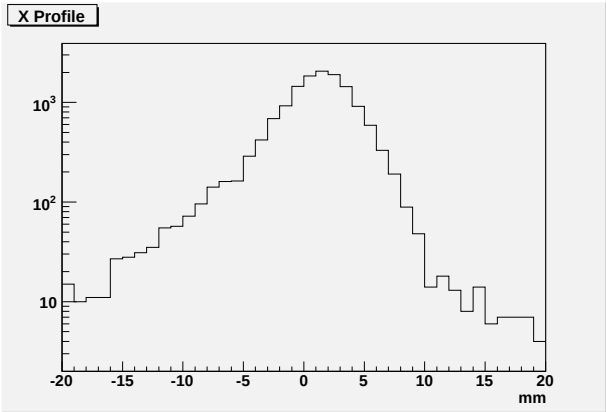

Figure 6.20. X profile of the proton beam.

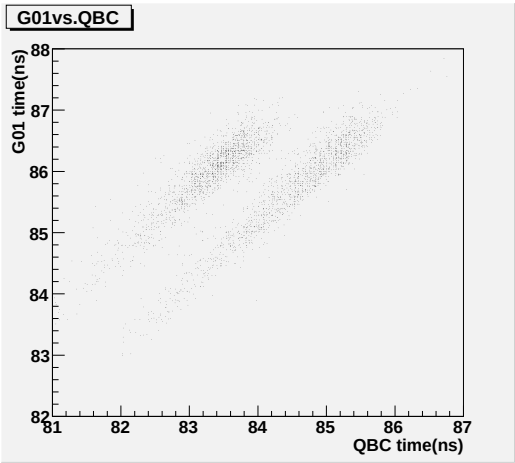

Figure 6.21. Noise (left band) and signal (right band) selection using GASTOF times.

signal and with noise with the movable table at three different positions in Fig. 6.22. These plots show that the noise mostly came from the adjacent instrumented rows which were to the right of the row that was being read out, which in the signal plots moves consistently to the right as the table position is increased. This is evidence that the noise time peak in the distributions was related to the other instrumented rows. There are no instrumented rows to the left of row QB and this is consistent with an almost empty noise plot (lower right) when the table is at is right most position. Conversely, selecting tracks through row QB or outside row QB, we plotted whether this tracks corresponded

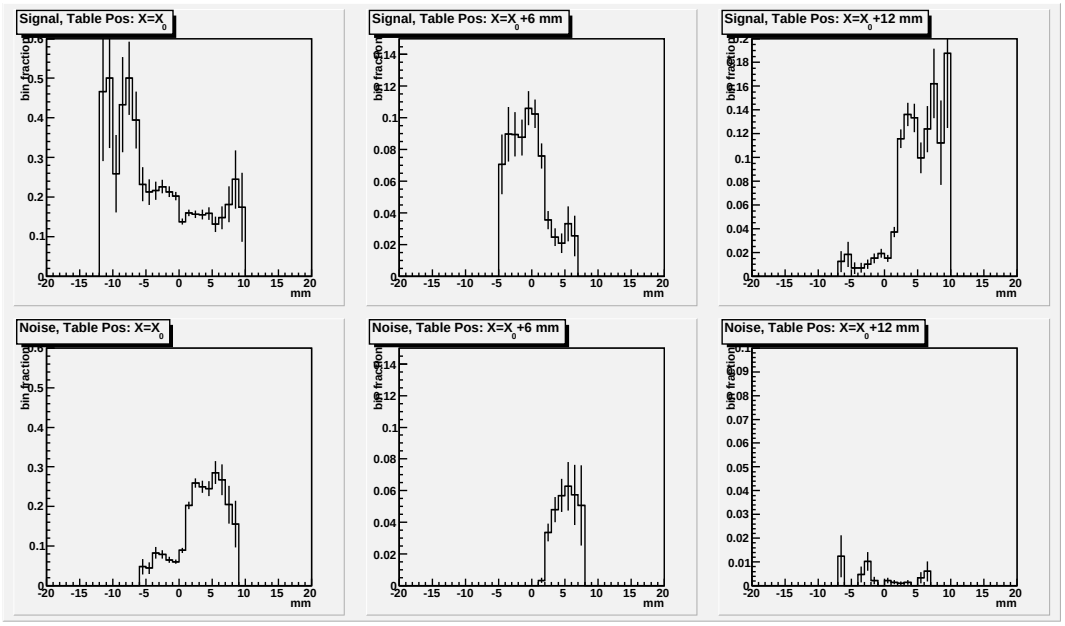

Figure 6.22. Bin fraction for signal and noise tracks in three table positions, +0 mm (left), +6 mm (center), and +12 mm (right).

to signal or noise. The results are in Fig. 6.23. The time peaks were identified using the GASTOF counter but the raw time is plotted, so they overlap. The tracks through row QB are correlated with the signal times and the tracks outside the row produce mostly noise times.

Selecting the tracks going through the QB row we obtained events free from noise produced by the other instrumented rows and measured the time resolutions and the the performance of the custom-made electronic boards. Since we were concerned about pixel to pixel crosstalk we also made the requirement that the TOF differences were from non-adjacent bars and that the bar in between had been off in the event. This gave us a clean sample but with not a lot of statistics. The best difference resolution result of 88 ps was obtained between $\boxed{\mathsf{QBC} \rightarrow \mathsf{6dB} + \mathsf{Hamamatsu} \rightarrow \mathsf{LCFD8} \rightarrow \mathsf{TDC\ 8}}$ and $\boxed{\mathsf{QBE} \rightarrow \mathsf{6dB} + \mathsf{Ortec9306} \rightarrow \mathsf{LCFD10} \rightarrow \mathsf{TDC\ 10}}$, both at 2800 V. We also obtained 93 ps in another run with this same setup, the plots are shown in Fig. 6.24. The average

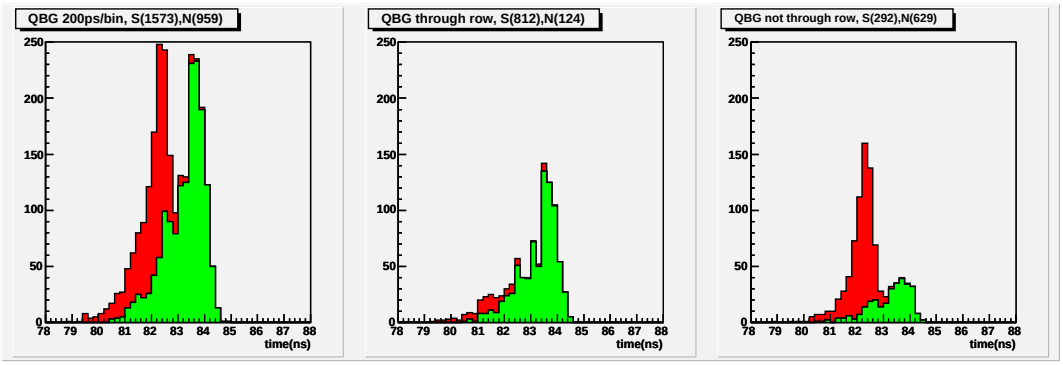

Figure 6.23. Stacked histograms, signal (green) and noise (red) times for any track (left), tracks through row QB (center), and tracks not through QB.

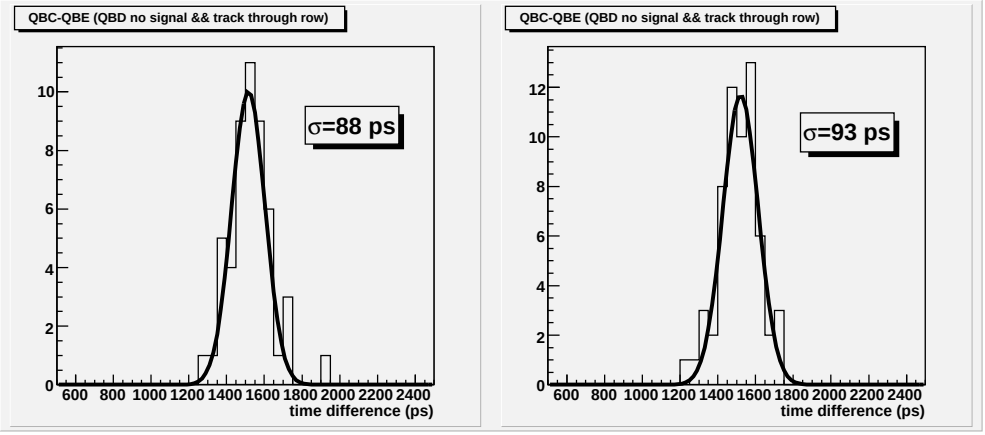

Figure 6.24. Best resolution between two QUARTIC bars.

difference resolution obtained with this cuts to avoid noise and cross-talk was 116 ps, this translates to an average individual counter resolution of 82 ps.

Considering the estimate of the detector resolution presented in Section 4.3, which was of 39 ps for the 10 μm tube we can make an estimate of the performance of the electronics. The resolution component introduced is $\sqrt{82^2 - 39^2}$ =72 ps on the average. This shows an improvement by using the LCFD over the 934 discriminator used in Run I, where the average resolution component of the electronics of one counter was 88 ps.

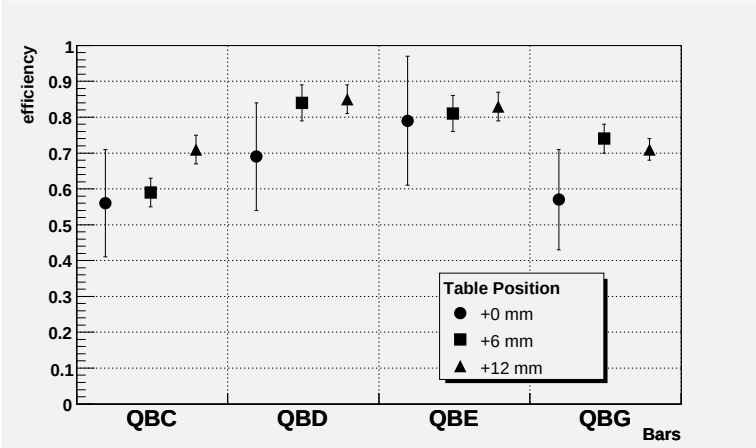

Figure 6.25. Efficiency of the QUARTIC bars. (Note that the table position is not with respect to the beam spot. +0 mm is furthest from the spot and +6, +12 mm are closest.

6.2.2.1 Efficiency

The efficiency was determined for the events that had tracking, at the three table positions. For each bar we defined the efficiency as the fraction of events with signal times out of events with a track through the row and another two bars on. The average efficiency of the QUARTIC bars was 75%. For the different table positions we see that at +0 mm when row QB further away from the beam center the efficiency is the lowest, see Fig. 6.25. The reason for this being that most tracks hit the detector near the edge. The efficiency of the GASTOF counters was determined also. Counting the fraction of events with good times out of those that had a track through the detectors. The average efficiency was 90% for the GASTOF1 prototype and 36% for the GASTOF2 prototype.

6.2.3 Oscilloscope data

The data taken with the oscilloscope consists of waveforms with a 20 ps/pt resolution. In order to achieve a better resolution with the scope we did not use the scintillator

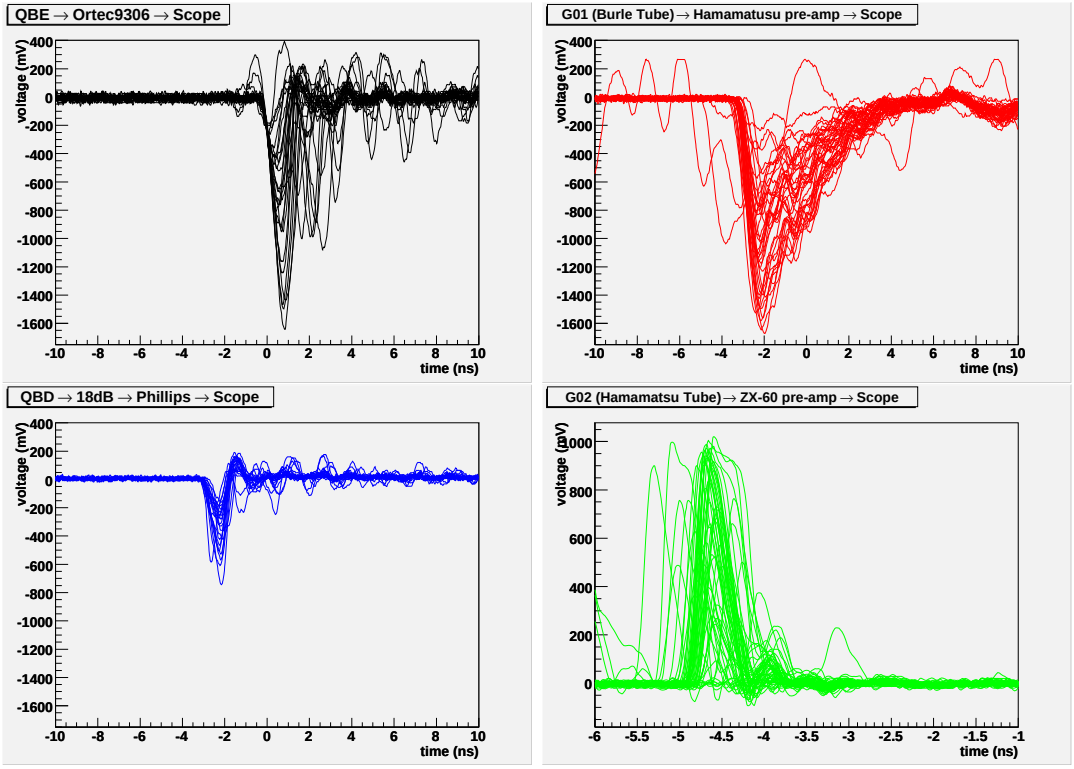

Figure 6.26. Waveforms for proton events obtained with the oscilloscope, 20 ps/pt. The lower right (Hamamatsu MCP-PMT has a different time scale.

trigger [9] but triggered the scope with a coincidence from two of the detectors in the beam. The oscilloscope has four channels and we connected two QUARTIC bars and the GASTOF1 and GASTOF 2 prototypes. The pulses were found to have an almost linear rising edge, but the trailing edge was not linear and oscillations were observed. The risetime of the GASTOF 2 pulses (Hamamatsu MCP-PMT) was shorter than the GASTOF1 or QUARTIC (Burle MCP-PMT) as expected, justifying the different design parameters for the CFD channels. A persistance view of the pulses for each detector is shown in Fig. 6.26. The waveforms have been analyzed by Tomasz Pierzchala from UC Louvain who has applied the LCFD timing algorithm to the pulses to determine what

[9] The scintillator trigger arrives about 70 ns later and the scope's dynamic range is shorter when the sampling rate is increased

Table 6.2. Comparison of applying threshold and LCFD timing algorithms to scope waveforms

	Treshold	LCFD
σ(G01-G02)	45 ps	35 ps
σ(G01-QBE)	106 ps	74 ps
σ(G01-QBD)	140 ps	64 ps
σ(G02-QBE)	99 ps	69 ps
σ(G02-QBD)	120 ps	50 ps
σ(QBE-QBD)	89 ps	63 ps

Including QBE-QBD

individual counters	
σ(G01)	42 ps
σ(G02)	24 ps
σ(QBE)	59 ps
σ(QBD)	40 ps

Differences	Predicted	Measured
σ(G01-G02)	48 ps	35 ps
σ(G01-QBE)	72 ps	74 ps
σ(G01-QBD)	58 ps	64 ps
σ(G02-QBE)	63 ps	69 ps
σ(G02-QBD)	46 ps	50 ps

Distance from measured values (likelihood parameter) = 16.2
.

Table 6.3. Fit results including QBD-QBE measurement

improvement is obtained over a normal threshold discriminator. His results are shown in Table 6.2. The last row is highlighted in red,because since the bars used in the scope readout were adjacent and the times in them might be correlated. Indeed, when performing a fit to find the most probable detector resolutions we get biased results when including the QBE-QBD measurement, in other words, no set of individual counter resolutions matches all six differences measured based on the assumption of independence of the individual counter resolutions. Removing the correlated measurement and fitting we get a reasonable likelihood value for the fit, and determine the individual counter resolutions, see Tables 6.3 and 6.3.

Excluding QBE-QBD

individual counters	
σ(G01)	32 ps
σ(G02)	13 ps
σ(QBE)	68 ps
σ(QBD)	52 ps

Differences	Predicted	Measured
σ(G01-G02)	35 ps	35 ps
σ(G01-QBE)	75 ps	74 ps
σ(G01-QBD)	61 ps	64 ps
σ(G02-QBE)	69 ps	69 ps
σ(G02-QBD)	54 ps	50 ps

Distance from measured values (likelihood parameter) = 4.8
.

Table 6.4. Fit results excluding QBD-QBE measurement

Taking the average of the two resolutions obtained in the fit, 60 ps, and the 82 ps per bar on the average with the electronics allows us to measure the jitter of the electronics and separate it from the component introduced by the timing algorithm. $\sigma_{\text{jitter}} = \sqrt{82^2 - 60^2} = 55$ ps.

6.3 Summary of Results and Conclusion

In Run I we obtained a counter resolution of 115 ps, which according to the simulations gives a component of 88 ps introduced by the off-the shelf electronics used in this run.

In Run II we obtained a resolution of 82 ps per counter, which can be separated into an electronic jitter component of 55 ps, and a combination of algorithm (or timewalk) and detector component of 60 ps. The analysis of Run II data was more complicated because of the existence of coherent noise originated by the instrumentation of adjacent rows. In the next run our initial objective is to find a way of eliminating the coherent signal by understanding in a better way how it originates, whether it is optical crosstalk before the light hits the MCP-PMT or electronic crosstalk at the multi-pad anode. Also

one of the next steps in the development of the detector must be to achive reproducibility of the best results obtained so far in several channels of readout at the same time.

The detector simulations show that there should be enough light in every event to keep the efficiency at a very high value. So far the efficiencies observed are lower than expected, and improvement on this aspect is also one of the next steps for the development of the QUARTIC.

The possibility of improving the time resolution by having several detectors along the beam was demonstrated in both Run I and II, and based on this and the measured average individual counter resolution, with two QUARTIC detectors of 8 bars each and a bar efficiency of 75% a time resolution of at least $\sim 82/\sqrt{12}$=23 ps is expected to be achieved by the QUARTIC detector at the LHC, with no further improvement. This time resolution of the QUARTIC detectors, combined with the resolution of the GASTOF detectors would allow rejection of more than 95% of the pile-up background for central exclusive production of the Higgs boson decaying to $b\bar{b}$, which would make this channel a potential Higgs discovery channel.

APPENDIX A

User guide for the 7186 sjyLX and PP004 libraries

A.1 7186 sjyLX libraries

This libraries can be used in a Linux computer with the Jorway 411S branch controller and the sjyLX CAMAC interface. A simple DAQ example is provided in Section A.1.2.3 and the Makefile used to compile this example is also provided, in Section A.1.3. The implementation of only the most basic routines for the 7186 is presented here. To fully understand this routines the user needs access to the 7186 user's manual [38].

A.1.1 Header Files

A.1.1.1 7186tdc.h

```
1  /* ************************************************************
2   *
3   *  Definitions for the Phillips 7186 TDC routines.
4   *
5   * ************************************************************ */
6
7  #ifndef SEVEN_ONE_EIGHT_SIX_H
8  #define SEVEN_ONE_EIGHT_SIX_H
9
10 /* CAMAC system constants and types.*/
11 #define BRANCH 18
12 #define MaxCrate 6
13 #define MaxSlot 25
14 #define MaxSub 15
15 /* array of encoded CAMAC module addresses */
16 typedef int EXT [BRANCH+1][MaxCrate+1][MaxSlot+1][MaxSub+1];
17
18
19 /* general constants */
20
21
22 #define PEDESTAL 0
23 #define LOWER_THRESHOLD 1
24 #define UPPER_THRESHOLD 2
25 #define PARAMETER_TEST_REGISTER 4
26 #define DIGITAL_TEST 0
27 #define ONETHIRD_TEST 1
28 #define TWOTHIRD_TEST 2
29
30 /* global variables  */
31
32 /* function prototypes */
33
34 int  hellotdc();
35 void init_extarray        (EXT ext);
36 int  clear7186            (int *ext);
37 int  reset7186            (int *ext);
38 int  enableLam            (int *ext);
39 int  readLam              (int *ext);
40 int  pollLam              (int *ext);
41 int  writeread7186        (int *ext, unsigned short *dataw,
```

```
42                              unsigned short *datar, unsigned short channel);
43  int  enableControlRegister (int *ext, unsigned short enable);
44  int  disableControlRegister(int *ext, unsigned short disable);
45  int  readControlRegister   (int *ext, unsigned short *data);
46  int  readHitRegister       (int *ext, unsigned short *data);
47  int  readSparseData        (int *ext, int tdctag);
48  int  readSparseDataToFile  (int *ext, FILE *fp, int tdctag);
49  int  readChannelDataToFile (int *ext, FILE *fp,int ch);
50  int  writeParameterMemory  (int *ext, unsigned short *data,
51                              int parameter, unsigned short channel);
52  int  readParameterMemory   (int *ext, unsigned short *data,
53                              int parameter, unsigned short channel);
54  int  selectTestPattern     (int *ext, unsigned short pattern);
55  int  digitalTest           (int *ext);
56  int  frontEndOneThirdTest  (int *ext);
57  int  frontEndTwoThirdTest  (int *ext);
58
59
60  int  enableREG_Rfd02 (int *ext);
61  int  enableLAM_Rfd02 (int *ext);
62  int  checkLAM_Rfd02  (int *ext);
63  int  readLAM_Rfd02   (int *ext);
64
65  int  init_2323    (int *ext, int chan);
66  int  gatestop_2323(int *ext, int chan);
67
68  int  clear2249    (int *ext);
69  int  enable2249LAM(int *ext);
70  int  read2249ChannelDataToFile(int *ext,FILE *fp,int ch);
71
72  #endif /* SEVEN_ONE_EIGHT_SIX_H */
```

A.1.1.2 daq_routines.h

```
1  /* ************************************************************
2   *
3   *  Header file for the daq routines.
4   *
5   * ************************************************************ */
6
7  #ifndef DAQ_ROUTINES_H
8  #define DAQ_ROUTINES_H
9
10 typedef struct module {
11   int branch;
12   int crate;
13   int slot;
14   int *ext;
15 } MODULE;
16
17 /* Function Prototypes */
18 void init_module( MODULE *mod, char name[], int branch, EXT all);
19
20 #endif /* DAQ_ROUTINES_H */
```

A.1.2 Source Files

A.1.2.1 7186tdc.c

```
1  /* ************************************************************
2     This file contains C functions that can be used with the 7186
3     Phillips TDC camac module. The CAMAC cssa calls are made with
4     the function number and not a constant that indicates which parti-
5     clar function is being called.  So access to the users manual
6     of the module is necessary to understand this code.
7
8     All the TDC routines recieve a pointer to the TDC module
9     extension: int ext* . The subaddressed extension for a cssa
10    call is obtained by dereferencing this pointer:
11         SubAd = 1;
12         cssa(F,ext[SubAd],&data,&qres);
13
14    The main program that uses this routines needs to be consistent
15    with the subaddress dereferencing scheme assumed by this
16    routines.  A simple way to accomplish this is to encode all
17    subadresses in a global address array with the init_extarray
18    routine.  See test7186.c for an example of how to use this
19    routines.
20
21    This file also has routines for the RFD02 module, the
22    2249a ADC module, and the 2323a gate generator module
23    which are used in the T958 experiment.
24
25   Pedro M Duarte
26   tb user 958
27
28   06/15/06 pmd CREATED
29   07/10/06 pmd Added RFD02 routines
30   01/17/07 pmd Upgraded with more documentation.
31   01/17/07 pmd The data-to-file format has changed.  Programs that
32                analyze data files need to be careful with their parsing.
33
34
35 ** ************************************************************/
36
37 /* Other Libraries */
38 #include <stdio.h>
39 #include <stdlib.h>
40 #include <string.h>
41
42 #include "ieee_fun_types.h"
43 #include "7186tdc.h"
44
45 /*
46 ** init_extarray - initialize global address aray 'ext' for CAMAC
47                    modules
48 */
49 void init_extarray(EXT ext)
50 {
51   int j,k,m;
52   int crate;          /* CAMAC crate */
53   int slot;           /* CAMAC slot number */
54   int subad;          /* CAMAC subaddress */
55   /*encode all possible encoded address values for CAMAC commands */
56     for (j=0; j<=MaxCrate; j++) {
57       crate = j;
58       for (k=0; k<=MaxSlot; k++) {
59             slot = k;
60             for (m=0; m<=MaxSub; m++) {
61               subad = m;
62               cdreg( &(ext[BRANCH][j][k][m]),BRANCH,crate,slot,subad);
63              /* printf("ext = 0x%0x\n",ext[BRANCH][j][k][m]);*/ }}}
64 }
65
66
67 /*
68 ** clear7186 - Clear the Module. Resets front end, clears and disables
69                LAM, disables pedestals and thresholds.  The address lines
```

```
70                have no effect on this command.
71  */
72  int clear7186(int *ext)
73  {
74    int qres=0;
75    unsigned short blankdata=0;
76
77    cssa(9,ext[0],&blankdata,&qres);
78    if(qres == 1) return 0;
79    else{ printf("error clearing module: no q response\n");
80          return 1;}} /*clear7186*/
81
82
83  /*
84  ** reset7186 - Reset the Hit Register, LAM and data memory.
85  */
86  int reset7186(int *ext)
87  {
88    int qres=0;
89    unsigned short blankdata=0;
90
91    int extAux;
92    extAux = ext[3]; /* SubAd=3-Resets Hit Register, Lam and data memory */
93
94    cssa(11,extAux,&blankdata,&qres);
95    if(qres == 1) return 0;
96    else{ printf("error reseting module: no q response\n");
97          return 1;}} /*reset7186*/
98
99
100 /*
101 ** enableLam - Enable LAM. Enables LAM on the S1 strobe. The address
102               lines have no effect on this command.
103 */
104 int enableLam(int *ext)
105 {
106   int qres=0;
107   unsigned short blankdata=0;
108
109   cssa(26,ext[0],&blankdata,&qres);
110   if(qres == 1) return 0;
111   else{ printf("error enabling LAM: no q response\n");
112         return 1;}} /*enableLam*/
113
114
115 /*
116 ** readLam - reads LAM, returns read value.
117 */
118 int readLam(int *ext)
119 {
120   int qres=0;
121   unsigned short blankdata=0;
122
123   cssa(8,ext[0],&blankdata,&qres);
124   if(qres == 1) return 1;
125   else{ return 1;} } /*readLam*/
126
127
128 /*
129 ** pollLam - reads LAM, returns read value.
130 */
131 int pollLam(int *ext)
132 {
133   int qres=0;
134   unsigned short blankdata=0;
135
136   int pollcount=0;
137   int maxpollcount=5;
138
```

```
139     cssa(8,ext[0],&blankdata,&qres);
140     while ( !qres && pollcount++ < maxpollcount ){
141       cssa(8,ext[0],&blankdata,&qres);
142     }
143     return qres; } /*pollLam*/
144
145
146
147   /*
148   ** readSparseDataToFile - Only those channels with data that falls between
149                             upper and lower thresholds are read, starting with
150                             the highest numbered channel.  Each read presents
151                             the next channel on the hit list.  As each channel
152                             is read, its bit in the Hit Register is reset.
153                             Reading and empty buffer returns Q false, X true.
154
155                             Dumps data to a provided file.
156   */
157   int readSparseDataToFile(int *ext, FILE *fp, int tdctag)
158   {
159     int qres=0;
160     unsigned short data=0;
161
162     unsigned short channeldata;
163     unsigned short channelnumber;
164
165     cssa(4,ext[0],&data,&qres);
166
167     int n=0;
168     while(qres==1&&n!=16){
169        channeldata   = data &0xfff ; /* 0xfff = 0000111111111111 */
170        channelnumber = tdctag*16+(data >> 12)+1;
171        fprintf(fp,"# %2d %6d ps\n", channelnumber,channeldata*25);
172        cssa(4,ext[0],&data,&qres);
173        n++;
174     }
175
176    /* printf("Entire hit register read to file.\n");*/
177     return 0;} /*readSparseDataToFile*/
178
179
180
181   /*********************************
182    Routines for the 2323a Gate Generator
183   *********************************/
184
185
186   /* init_2323 - Sets the 2323 to latch mode.
187   */
188   int init_2323(int *ext, int chan)
189   {
190     unsigned short tmpdata=0;
191     int qres=0;
192
193     if (ext == NULL) return qres;
194
195     if((chan<0) || (chan>1)) printf("error: 2323 channel must be 0=A or 1=B\n");
196     /* stop channel output*/
197     cssa(9,ext[chan],&tmpdata,&qres);
198     /* write programming word*/
199     tmpdata=0x2000;
200     cssa(17,ext[chan],&tmpdata,&qres);
201     /* read back programming word*/
202     tmpdata=0;
203     cssa(1,ext[chan],&tmpdata,&qres);
204     if(tmpdata!=0x2000) printf("error: 2323 initialization failed\n");
205
206     if(qres == 1) return 0;
207     else{ printf("error initializing gate: no q response\n");
```

```
208           return 1;}
209   }
210
211
212   /* gatestop_2323 - Stops the 2323 gate.
213   */
214   int gatestop_2323(int *ext, int chan)
215   {
216     unsigned short tmpdata=0;
217     int qres=0;
218
219     if (ext == NULL) return qres;
220     if((chan<0) || (chan>1)) printf("error: 2323 channel must be 0=A or 1=B\n");
221     cssa(9,ext[chan],&tmpdata,&qres);
222
223     if(qres == 1) return 0;
224     else{ printf("error stopping gate: no q response\n");
225           return 1;}
226   }
227
228
229
230   /*********************************
231    Routines for the RFD02 LAM Module
232   *********************************/
233
234   /*
235    * Enable Fermi RFD02 module REGISTERS.
236    */
237
238   int enableREG_Rfd02(int *ext)       /* encoded module address */
239   {
240     unsigned short   data[1]={0xFFFF};  /* Enable all inputs on the rfd02 */
241     int              qres=0;            /* Q response */
242     /* Write Trigger mask */
243     cssa(16,ext[0],data,&qres);
244     return qres;
245   }
246
247
248   /*
249    * Enable Fermi RFD02 module LAM.
250    */
251
252   int enableLAM_Rfd02(int *ext)       /* encoded module address */
253   {
254     unsigned short   tmpSdata[2]={0}; /* temp short data */
255     int              qres=0;          /* Q response */
256     /* reset and enable LAM */
257     cssa(28,ext[0],tmpSdata,&qres);
258     return qres;
259   }
260
261   /*
262    * Check Fermi RFD02 module for LAM.
263    */
264
265   int readLAM_Rfd02(int *ext)         /* encoded module address */
266   {
267     unsigned short   tmpSdata[2]={0}; /* temp short data */
268     int              qres=0;          /* Q response */
269     /* test for LAM */
270     cssa(8,ext[0],tmpSdata,&qres);
271     if (qres) {
272       cssa(28,ext[0],tmpSdata,&qres);  /* reset and enable LAM */
273       return 1;
274     } else {
275       return 0;
276     }
```

```
277 }
278
279
280 /*
281  * Check Fermi RFD02 module's LAM. Differen from read because it does
282  * not reset the LAM.
283  */
284
285 int checkLAM_Rfd02(int *ext)          /* encoded module address */
286 {
287   unsigned short   tmpSdata[2]={0}; /* temp short data */
288   int              qres=0;          /* Q response */
289   /* test for LAM */
290   cssa(8,ext[0],tmpSdata,&qres);
291   if (qres) {
292     return 1;
293   } else {
294     return 0;
295   }
296 }
297
298
299
300 /*********************************
301  Routines for the 2249a ADC Module
302 *********************************/
303
304 /* clear2249 - Clears the module
305 */
306 int clear2249(int *ext)
307 {
308   unsigned short tmpdata=0;
309   int qres=0;
310   if (ext == NULL) return qres;
311   cssa(9,ext[0],&tmpdata,&qres);
312   if(qres == 1) return 0;
313   else{ /*printf("error clear2249: no q response\n");*/
314         return 1;}} /*clear2249*/
315
316
317
318 /* enable2249LAM - Enables the 2249LAM
319 */
320 int enable2249LAM(int *ext)
321 {
322   unsigned short tmpdata=0;
323   int qres=0;
324   if (ext == NULL) return qres;
325   cssa(26,ext[0],&tmpdata,&qres);
326   if(qres == 1) return 0;
327   else{ /*printf("error enable2249LAM: no q response\n");*/
328         return 1;}} /*enable2249LAM*/
329
330
331 /*
332 ** read2249ChannelDataToFile - Dumps 2249 data to a provided file.
333 */
334 int read2249ChannelDataToFile(int *ext,FILE *fp,int ch)
335 {
336   int qres=0;
337   unsigned short data=0;
338
339   cssa(2,ext[ch],&data,&qres);
340   fprintf(fp,"& %2d %6d *0.25pC\n", ch,data);
341
342   return 0;} /*read2249ChannelDataToFile*/
```

A.1.2.2 daq_routines.c

```
1  /* ***********************************************************
2     This file contains a C routine to initialize CAMAC modules.
3     A CAMAC module is represnted by the MODULE data type.
4
5    Pedro M Duarte
6    tb user 958
7
8    01/19/07 pmd CREATED
9
10
11 ** ********************************************************** */
12
13 /* Other Libraries */
14 #include <stdio.h>
15 #include <stdlib.h>
16 #include <string.h>
17 #include <unistd.h>
18
19 #include "ieee_fun_types.h"
20 #include "7186tdc.h"
21 #include "daq_routines.h"
22
23
24 /*
25 ** init_module - Initializes a module structure.
26 */
27 void init_module( MODULE *mod, char name[], int branch, EXT all){
28   mod->branch = branch;
29
30   printf("\n Initializing %s module : \n", name);
31
32   printf("%s crate ", name);
33   scanf("%d", &(mod->crate) );
34   printf("%d\n", mod->crate);
35
36   printf("%s slot ", name);
37   scanf("%d", &(mod->slot) );
38   printf("%d\n", mod->slot);
39
40   mod->ext = &( all[mod->branch][mod->crate][mod->slot][0] );
41   return;
42 }
```

A.1.2.3 example.c

```
1  /* ******************************************************
2
3    This file makes the simplest data acquisition loop for the
4    Phillips 7186 TDC. It can be used for debugging purposes
5    or as an example.
6
7    Pedro M Duarte
8    tb user 958
9
10   03-01-06   CREATED
11
12 ****************************************************** */
13
14 /* Libraries */
15 #include <stdio.h>
16 #include <stdlib.h>
```

```
17 #include <string.h>
18 #include <time.h>
19 #include <signal.h>
20
21 #include "ieee_fun_types.h"
22 #include "7186tdc.h"
23 #include "daq_routines.h"
24
25
26
27 int main(int argc, char **argv) {
28
29     MODULE tdcA;
30
31     EXT all;
32     init_extarray(all);
33
34     int branch=18;
35     init_module( &tdcA , "tdcA", branch, all);
36
37     char timestamp[12];
38     printf("enter timestamp: ");
39     scanf("%s",timestamp);
40
41     int nevents;
42     printf("enter number of desired events for this run: ");
43     scanf("%d",&nevents);
44
45     /* open the SCSI device */
46     if( (cdchn(branch,1,0) &1) != 1){
47         perror("cdchn error; cannot open branch");
48         return 1;
49     }
50
51     /* set the controller type */
52     ccctype(branch,0,1);  /* parallel - Jor73A is considered parallel */
53     int extcrate;
54     int crate=tdcA.crate;
55     int slot=tdcA.slot;
56     cdreg( &extcrate, branch,crate,slot,0 );
57         /* crate clear */
58          cccc(extcrate);
59         /* crate initialize*/
60          cccz(extcrate);
61         /* remove crate inhibit */
62          ccci(extcrate,0);
63
64
65     unsigned short  data = 0;
66
67     clear7186(tdcA.ext);
68     printf("\n");
69     printf("disabling upper,lower,pedestal...\n");
70     disableControlRegister(tdcA.ext,111);
71     readControlRegister(tdcA.ext,&data);
72     printf("...controlregister...0x%x\n\n", data);
73     enableLam(tdcA.ext);
74     reset7186(tdcA.ext);
75
76     FILE *fpdat=NULL;
77     char tempname[256] = "/usr/home/mtbf_user/t958/daq/data/tdconly/";
78     strcat(tempname,timestamp);
79     char makedir[256] = "mkdir ";
80     strcat(makedir,tempname);
81     system(makedir);
82     strcat(tempname,"/data");
83     strcat(tempname,timestamp);
84     char datafile[256];
85
```

```
86      fpdat = fopen(datafile,"w");
87      printf("Data file : %s", datafile);
88      fputs(datafile,fpdat);
89      fprintf(fpdat,"\n");
90
91      int ratetest=0;
92      printf("\ntaking data...\n");
93
94      while( ratetest < nevents ) {
95
96        printf("Waiting for LAM...\n");
97        int qresA=0;
98        while ( qresA !=1 ){ qresA = readLam(tdcA.ext); }
99
100
101         fprintf(fpdat,"\n!Event #%d\n",ratetest+1);
102         readSparseDataToFile(tdcA.ext,fpdat,0);
103         reset7186(tdcA.ext);
104       ratetest++;
105     }
106
107   fclose(fpdat);
108   printf("Number of Hits Taken.....%d\n",ratetest);
109
110   return 0;
111 }
```

A.1.3 Makefile

```
1  # Example Makefile for the T958 daq programs.
2  # Compiles example.c
3  #
4  # The directory paths correspond to the MTBF daq computer.
5  #
6  # Author: Pedro M Duarte, 01/16/2007
7
8  CC        = gcc
9  ObjSuf    = o
10 HeaSuf    = h
11 SrcSuf    = c
12 ExeSuf    =
13 OutPutOpt = -o
14
15 CFLAGS  = -I/usr/include -I/fnal/ups/prd/sjyLX/v2_5/Linux-2-4/include -Iinc -g -Wall #-ansi
16 LDFLAGS = -I/usr/include -I/fnal/ups/prd/sjyLX/v2_5/Linux-2-4/include -Iinc
17 LIBRARY = /fnal/ups/prd/sjyLX/v2_5/Linux-2-4/lib/libsjy.a
18
19 # Rules
20 %.o : src/%.c inc/%.h
21         $(CC) $(CFLAGS) -c src/$*.c -o $@
22
23 # Files
24
25 TDC7186O    = 7186tdc.$(ObjSuf)
26 TDC7186S    = src/7186tdc.$(SrcSuf)
27 TDC7186H    = inc/7186tdc.$(HeaSuf)
28
29 DAQROUTO    = daq_routines.$(ObjSuf)
30 DAQROUTS    = src/daq_routines.$(SrcSuf)
31 DAQROUTH    = inc/daq_routines.$(HeaSuf)
32
33 EXAMPLEO    = example.$(ObjSuf)
34 EXAMPLES    = src/example.$(SrcSuf)
35 EXAMPLE     = example$(ExeSuf)
36
```

```
37 OBJS          = $(TDC7186O) $(DAQROUTO) $(EXAMPLEO)
38
39 PROGRAMS      = $(TEST7186) $(EXAMPLE)
40
41 #-------------------------------------------------------------------------
42
43 all    : $(PROGRAMS) clean
44
45 $(TDC7186O):     $(TDC7186S) $(TDC7186H)
46
47 $(DAQROUTO):     $(DAQROUTS)   $(DAQROUTH)
48
49 $(EXAMPLE):               $(EXAMPLES) $(TDC7186O) $(DAQROUTO) $(LIBRARY)
50         $(CC) $(CFLAGS) $^ -lm -o $@
51         @echo "$@ done"
52
53 clean:
54         @rm -f $(OBJS)
55
56
57 ###
```

A.2 7186 PP004 libraries

To use the CAMAC PP004 branch controller the user needs to create a Microsoft Visual Studio 2005 project. This project must have a source file with a main function which is the entry point for the application. In this section I present a sample source file with a simple DAQ loop. To build the executable the user needs to save a copy of the following files to the project's directory. The files are available for download in [42]:

- WinIo.lib
- WinIo.sys
- WinIo.dll
- WinIo.h
- WINIO.VXD
- Winmm.lib
- PPCam32.ini
- PPCam32.lib
- PPCam32.dll
- PPCAM32.H

To correctly link the executable with the dynamically linked libraries (DLL's) the user needs to go to the Project::Properties menu (shortcut Alt+F7) under Linker, under Command Line in the Additional Options box write: `PPCam32.lib WinIo.lib`.

A.2.1 pp004example.cpp

```
1  // pp004example.cpp : Defines the entry point for the console application.
2  //
3  // This example file contains the prototype and implementation for the
4  // most used 7186 routines.  They are used in a simple DAQ loop.
5
6  #include "stdafx.h"
7  #include "ppcam32.h"
8
9  #include <stdio.h>
10 #include <iostream>
11 #include <fstream>
12
13 #define Crate 1
14 #define Station 12  // Station or slot where the module is installed
15
16
17 //--------------------------------------------------------------------
18 // Function Prototypes
19
20 void camac(int *p_N,int *p_F,int *p_A, int *p_D,int *p_Q,int *p_X);
21 int  getRunNum();
22
23 int  reset7186();
24 int  clear7186();
25 int  enableLam();
26 int  waitForLam();
27 void readDataToFile(FILE *fp, int ch);
28
29
30 int main(int argc, char* argv[])
31 {
32         int qres=0;
33         int xflag=0;
34
35         int crate = Crate;
36         Crate_set(&crate);
37
38         unsigned int ZCI_bits = 1; //1= Z (Initialize) Cycle
39         camcl(&ZCI_bits);
40         ZCI_bits = 2; // 2 = C (Clear) Cycle
41         camcl(&ZCI_bits);
42
43         reset7186();
44         clear7186();
45         enableLam();
46
47         int maxevs;
48         std::cout << "Events ? ";
49         std::cin >> maxevs;
50
51         int runnum = getRunNum();
52         char name[256];
53         sprintf_s(name,"Run%04d.txt",runnum);
54         FILE *fp;
55         errno_t err;
56         if( (err  = fopen_s( &fp, name, "w" )) !=0 ){
```

```
57                  printf( "The file %s was not opened\n",name );
58                  return 1;
59          }
60          fputs(name,fp);
61          fprintf(fp,"\n");
62
63          for(int nevs=0; nevs!=maxevs; nevs++){
64                  waitForLam();
65                  fprintf(fp,"\n!Event #%d\n", nevs+1);
66                  // read connected channels
67                  readDataToFile(fp,1);
68                  readDataToFile(fp,2);
69                  readDataToFile(fp,3);
70                  clear7186();
71                  enableLam();
72          }
73
74          fclose(fp);
75
76          std::cout << maxevs << " written to file." << std::endl;\
77          return 0;
78  }
79
80
81  //----------------------------------------------------------------------
82  // Function implementations
83
84  void camac(int *p_N,int *p_F,int *p_A, int *p_D,int *p_Q,int *p_X){
85          if(*p_F<8){
86                  cami(p_N,p_F,p_A,p_D,p_Q,p_X);
87          }
88          else {
89                  camo(p_N,p_F,p_A,p_D,p_Q,p_X);
90          }
91  }
92
93  int getRunNum(){
94          int runnum=0;
95          std::cout << "Type the run number : ";
96          std::cin >> runnum;
97          return runnum;
98  }
99
100 int reset7186(){
101         int qres=0;       int xflag=0;  int blankdata=0;
102         int c=Crate;  int s=Station;
103         int f=11;     //reset
104         int subad=3; //reset
105         camac(&s,&f,&subad,&blankdata,&qres,&xflag);
106         if(!xflag) std::cout << "No Xflag" << std::endl;
107         if(!qres)  std::cout << "No Qres" << std::endl;
108         return qres;
109 }
110
111 int clear7186(){
112         int qres=0;       int xflag=0;  int blankdata=0;
113         int c=Crate;  int s=Station;
114         int f=9;      //clear
115         int subad=0; //clear
116         camac(&s,&f,&subad,&blankdata,&qres,&xflag);
117         if(!xflag) std::cout << "No Xflag" << std::endl;
118         if(!qres)  std::cout << "No Qres" << std::endl;
119         return qres;
120 }
121
122 int enableLam(){
123         int qres=0;       int xflag=0;  int blankdata=0;
124         int c=Crate;  int s=Station;
125         int f=26;     //enableLam
```

```
126         int subad=0; //enableLam
127         camac(&s,&f,&subad,&blankdata,&qres,&xflag);
128         if(!xflag) std::cout << "No Xflag" << std::endl;
129         if(!qres)  std::cout << "No Qres" << std::endl;
130         return qres;
131 }
132
133 int waitForLam(){
134         int qres=0;      int xflag=0;  int blankdata=0;
135         int c=Crate;  int s=Station;
136         int f=8;     //enableLam
137         int subad=0; //enableLam
138         while (qres!=1) camac(&s,&f,&subad,&blankdata,&qres,&xflag);
139         if(!xflag) std::cout << "No Xflag" << std::endl;
140         if(!qres)  std::cout << "No Qres" << std::endl;
141         return qres;
142 }
143
144 void readDataToFile(FILE *fp, int ch){
145         int qres=0;      int xflag=0;  int data=0;
146         int c=Crate;  int s=Station;
147         int f=0;        //read data
148         int subad=ch-1; //channel
149         camac(&s,&f,&subad,&data,&qres,&xflag);
150         int channeldata   = data & 0xFFF ;
151         int channelnumber = (data >> 12)+1;
152         if(!xflag) std::cout << "No Xflag" << std::endl;
153         if(!qres)  std::cout << "No Qres" << std::endl;
154         fprintf(fp,"# %2d %6d ps\n", channelnumber, channeldata*25);
155 }
```

APPENDIX B

T958 DAQ Source Code

B.1 T958 timing DAQ code

This is the source code for the timing process which runs in parallel with the MTBF tracking DAQ process. The MTBF tracking DAQ source code can be found in the MTBF computer or obtained by contacting Test Beam Coordinator Erik Ramberg, ramberg@fnal.gov.

```
/* ******************************************************

   This file makes a data acquisition loop for the
   Phillips 7186 TDC.  Routines are collected in
   daq_routines.c and 7186tdc.c

   Creates a directory with the timestamp of th run.
   Writes the data to a separate file for each spill.

   Modify the code where indicated to read a second
   7186 TDC or a 2249a ADC.

   The crate clear, initialize and remove inhibit are
   commented since this code is meant to run at the same
   time as mtest, which is the MWPC's daq system.  The MWPC
   process is run in the background before this one and
   takes care of initialization of the CAMAC crates.

   Pedro M Duarte
   tb user 958

   07/20/06  pmd  CREATED
   01/18/07  pmd  Included a module structure in the
                  daq_routines.c file.
   01/24/07  pmd  Finished first revision of modifications
                  for 2nd run.

****************************************************** */

/* Libraries */
#include <stdio.h>
#include <stdlib.h>
#include <string.h>
#include <time.h>
#include <unistd.h>
#include <signal.h>

#include "ieee_fun_types.h"
#include "7186tdc.h"
#include "daq_routines.h"

int cntrlc=0;
void stop_daq(void);

int main(int argc, char **argv) {

    if( argc<2 ){ printf("USAGE: daq <pid>\n");
                  return 1; }
    int pid_mtest=atoi(argv[1]);

    MODULE tdcA;
    MODULE tdcB;
    MODULE adc;
    MODULE gate;
    MODULE rfd02;
```

```
56
57      EXT all;
58      init_extarray(all);
59
60      int branch=18;
61
62      init_module( &tdcA, "tdcA", branch, all);
63      init_module( &tdcB, "tdcB", branch, all);
64      init_module( &adc,  "adc" , branch, all);
65      init_module( &gate, "gate", branch, all);
66      init_module( &rfd02,"rfd02",branch, all);
67
68      char timestamp[12];
69      printf("enter timestamp: ");
70      scanf("%s",timestamp);
71
72      int nevents;
73      printf("enter number of desired events for this run: ");
74      scanf("%d",&nevents);
75
76      /* open the SCSI device */
77      if( (cdchn(branch,1,0) &1) != 1){
78          perror("cdchn error; cannot open branch");
79          return 1;
80      }
81      /* set the controller type */
82      ccctype(branch,0,1);
83
84      /* waits 5 seconds for MMPC process to initialize the
85         crates and the MMPC modules */
86      sleep(5);
87
88      /* Does not initliazize crates. MMPC process takes care
89         of this. */
90      /* int extcrate;*/
91      /* cdreg( &extcrate, branch,crate,slot,0 ); */
92      /* crate clear */
93      /* cccc(extcrate);*/
94      /* crate initialize*/
95      /* cccz(extcrate);*/
96      /* remove crate inhibit */
97      /* ccci(extcrate,0); */
98
99      unsigned short  data = 0;
100
101     /* The rfd02 module must be set in CAMAC mode
102        via switch in the front panel. */
103     enableREG_Rfd02(rfd02.ext);
104     enableLAM_Rfd02(rfd02.ext);
105
106     init_2323(gate.ext,1); /*1 is ChB*/
107
108     clear7186(tdcA.ext);
109     printf("\n");
110     printf("disabling upper,lower,pedestal...\n");
111     disableControlRegister(tdcA.ext,111);
112     readControlRegister(tdcA.ext,&data);
113     printf("...controlregister...0x%x\n\n", data);
114     enableLam(tdcA.ext);
115     reset7186(tdcA.ext);
116
117     /*Possibility of having a second 7186 read out */
118     /*clear7186(tdcB.ext);
119     printf("disabling upper,lower,pedestal...\n");
120     disableControlRegister(tdcB.ext,111);
121     readControlRegister(tdcB.ext,&data);
122     printf("...controlregister...0x%x\n\n", data);
123     enableLam(tdcB.ext);
124     reset7186(tdcB.ext); */
```

```
125
126       /*Possibility of having an ADC read out*/
127       /*clear2249(adc.ext);
128       enable2249LAM(adc.ext); */
129
130       FILE *fpdat=NULL;
131
132       char tempname[256] = "/usr/home/mtbf_user/t958/daq/data/tdc/";
133       strcat(tempname,timestamp);
134
135       char makedir[256] = "mkdir ";
136       strcat(makedir,tempname);
137       system(makedir);
138
139       strcat(tempname,"/data");
140       strcat(tempname,timestamp);
141       char datafile[256];
142       strcpy(datafile,tempname);
143
144       int  spill=0;
145       char spillstr[10];
146       sprintf(spillstr,"%03d",spill);
147
148       strcat(datafile,".");
149       strcat(datafile,spillstr);
150
151       fpdat = fopen(datafile,"w");
152       printf("\nData file : %s", datafile);
153       fputs(datafile,fpdat); fprintf(fpdat,"\n");
154
155       int ratetest=0;
156       printf("\ntaking data...\n");
157
158       int spillend=0;
159       signal(SIGINT,stop_daq);
160
161       while( ratetest < nevents ) {
162
163           do {
164             if ( cntrlc ) break;
165
166             if ( pollLam(tdcA.ext) ){
167                 fprintf(fpdat,"\n!Event #%d\n",ratetest+1);
168                 readSparseDataToFile(tdcA.ext,fpdat,0);
169
170                 /*readSparseDataToFile(tdcB.ext,fpdat,1);*/
171
172                 /*read2249ChannelDataToFile(adc.ext,fpdat,0);*/
173                 /* Add more ADC channels to readout here */
174
175                 reset7186(tdcA.ext);
176                 /*reset7186(tdcB.ext);*/
177                 /*clear2249(adc.ext);*/
178                 /*enable2249LAM(adc.ext);*/
179
180                 /*Do not stop veto for last event or if
181                   process has been interrupted*/
182                 if( ratetest < nevents-1 && !cntrlc) gatestop_2323(gate.ext,1);/*1 is ChB*/
183
184                 ratetest++;
185             }
186
187             /* Read RFD02 for end of spill trigger */
188             /* If LAM is found readLAM resets it */
189             spillend = readLAM_Rfd02(rfd02.ext);
190
191           } while (!spillend);
192
193           if (cntrlc) break;
```

```
194
195           printf("T958 : end of spill DETECTED\n");
196           printf("T958 : %d events so far.\n",ratetest);
197           fclose(fpdat);
198           strcpy(datafile,tempname);
199           spill++;
200           sprintf(spillstr,"%03d",spill);
201           strcat(datafile,".");
202           strcat(datafile,spillstr);
203           fpdat = fopen(datafile,"w");
204           spillend=0;
205       }
206
207       kill(pid_mtest,SIGINT);
208       fclose(fpdat);
209       printf("Number of Hits Taken.....%d\n",ratetest);
210
211       return 0;
212   }
213
214   /*Signal handler to close gracefully on cntrl-c*/
215   void stop_daq(){
216       printf("\n-Terminating daq-\n");
217       cntrlc=1;
218   }
```

B.2 Synchronized mode bash script

This bash script is used to start the tracking and timing DAQ programs at the same time. The tracking DAQ runs in the background. Interrupt signals are handled by the timing DAQ process which propagates them to the tracking process for a graceful termination with ctrl-c without loosing synchronization.

```
1   #!/bin/sh
2
3   # Start of run interface
4   python ~/t958/daq/settings/interface.py
5
6
7   # MTEST daq
8   #-mtest'S pid is saved in pid variable
9   cd /fnal/ups/prd/mtest/v2_1/bin
10  ./mtest958 < ~/t958/daq/settings/input_mtest &
11  pid=`ps | awk '/mtest958/ && !/awk/ {print $1}'`
12  echo "mtest pid = $pid"
13
14  # T958 daq
15  #-When the desired number of events is completed
16  #-it sends a signal to mtest.
17  cd ~/t958/daq/t958daq
18  ./daq $pid < ~/t958/daq/settings/input_daq
```

REFERENCES

[1] Michael E. Peskin. Supersymmetry: The next spectroscopy. Werner Heisenberg Centennial Symposium Munich, Germany, December 5-7, 2001. arXiv:hep-ph/0212204v1.

[2] Paul De Jong. Challenges for early discovery in ATLAS and CMS. Moriond 2007. Electroweak Interactions and aUnified Theories. arXiv:hep-ex/07050611v1.

[3] Vincenzo. Barone and Enrico. Predazzi. *High-Energy Particle Diffraction*. Springer, Berlin-Heidelberg, 2002.

[4] E.Predazzi. Diffraction: past, present and future. Lectures given at Hadrons VI (Florianopolis, Brazil). arXiv:hep-ph/9809454v1.

[5] J. D. Bjorken. Rapidity gaps and jets as a new-physics signature in very-high-energy hadron-hadron collisions. *Physical Review D*, 47:101–113, 1993.

[6] G. Ingelman and P.Schlein. Jet structure in high mass diffractive scattering. *Physics Letters B*, 152:256–260, 1985.

[7] A. Brandt et al. Evidence for a super-hard pomeron structure. *Physics Letters B*, 297:417–424, 1992.

[8] D0 and CDF. Rapidity gaps between jets at D0 and CDF. See for example references in http://citeseer.ist.psu.edu/cs.

[9] A. Bialas and P. V. Landshoff. Higgs production in pp collisions by double-pomeron exchange. *Physics Letters B*, 256:540–546, 1991.

[10] Brian Cox. A review of forward proton tagging at 420m at the lhc, and relevant results from thetevatron and hera. Talk presented at the 15th Topical Conference on Hadron Collider Physics, HCP2004. arXiv:hep-ph/0409144v1.

[11] A. De Roeck, V.A. Khoze, A.D. Martin, R. Orava, and M.G. Ryskin. Ways to detect a light higgs boson at the LHC. *Eur. Phys. J. C.*, 25:391–403, 2002. arXiv:hep-ph/0207042v2.

[12] A.B. Kaidalov, V.A. Khoze, A.D. Martin, and M.G. Ryskin. Extending the study of the higgs sector at the LHC by proton tagging. *Eur. Phys. J. C.*, 33:261–271, 2003. arXiv:hep-ph/0311023v2.

[13] R. Battiston et al. The "roman pot" spectrometer and the vertex detector of experiment UA4 at the CERN SPS collider. *Nuclear Instruments and Methods in Physics Research A*, 238:35–44, July 1985.

[14] R. Appleby, P. Bussey, et al. FP420 : An R&D proposal to investigate the feasibility of installing proton tagging detectors in the 420m region at LHC. fp420.com.

[15] T. Mäki, J. Kalliopuska, J.W. Lämsä, N. Marola, R. Orava, K. Österberg, M. Ottela, and S. Tapprogge. Detecting leading protons in exclusive central diffractive processes at the LHC. fp420.com.

[16] C.Da Via et al. Advances in silicon detectors for particle tracking in extreme radiation environments. *Nuclear Instruments and Methods in Physics Research A*, 509:86–91, 2004.

[17] Andrew Pilkington. *Central Exclusive Production at TeV energies*. PhD thesis, University of Manchester, 2006.

[18] B.E. Cox, A. De Roeck, V.A. Khoze, et al. Detecting the standard model higgs boson in the ww decay channel using forward proton tagging at the LHC. *Eur. Phys. J. C*, 45:401–407, 2006. arXiv:hep-ph/0505240v3.

[19] ATLAS Collaboration. ATLAS: Detector and physics performance technical design report. Technical report, ATLAS Collaboration, 1999. Pages 86-90. ATLAS TDR.

[20] Monika Grothe. Prospects for diffractive and forward physics at the lhc. Talk at Particle Physics Seminar, University of Helsinki. grothe.

[21] CDF Collaboration. The cdf ii beyond the baseline proposal: An inner silicon layer and a time of flight detector. www-cdf.fnal.gov.

[22] W.-M. Yao et al. Review of particle physics. *Journal of Physics G*, 33, 2006.

[23] Claus Grupen. *Particle Detectors*. Cambridge University Press, Cambridge, 1996.

[24] John David Jackson. *Classical Electrodynamics*. John wiley & Sons, Inc, 1998.

[25] Dan Green. *The Physics of Particle Detectors*. Cambridge University Press, 2000. Page 65.

[26] J. Va'vra et al. Development of photon detectors for a fast focusing DIRC. 5th International workshop on ring Imaging Cherenkov Counters (RICH 2004). Playa del Carmen, Mexico. SLAC-PUB-11107.

[27] J.L. Wiza. Microchannel plate detectors. *Nuclear Instruments and Methods*, 162:587, 1979.

[28] M. Akatsu et al. MCP − PMT timing property for single photons. *Nuclear Instruments and Methods in Physics Research A*, 528:763–775, 2004.

[29] H. Frisch et al. See for example talks by University of Chicago group at the Pico-sec Timing HHardware Workshop, Chicago, IL, Nov. 2005. hep.uchicago.edu, 2005.

[30] K.Inami et al. A 5ps TOF-counter with an mcp-pmt. *Nuclear Instruments and Methods in Physics Research A*, 560:303–308, 2006.

[31] J. Va'vra et al. A 30 ps riming resolution for single photons with multi-pixel burle MCP − PMT. 10th Pisa Meeting On Advanced Detectors: Frontier Detectors For Frontier Physics. Elba, Italy. SLAC-PUB-11934.

[32] P. Duarte. QUARTIC: A Fast Time-of-flight Counter. *APS Meeting Abstracts*, April 2006.

[33] CERN/EP-MIC. Hptdc manual. www.

[34] A.V. Akindinov and others (ALICE Collaboration). Design aspects and prototype test of a very precise TDC system implemented for the multigap RPC of the

ALICE – TOF. *Nuclear Instruments and Methods in Physics Research A*, 533:178–182, 2004.

[35] Fast Timing section of the FP420 Technical Design Report. In preparation.

[36] See MTBF's web page at http://www-ppd.fnal.gov/MTBF-w/.

[37] H. Fenker. A standard beam pwc for fermilab. Technical report, Fermilab, 1983. TM-1179.

[38] See specifications online, http://www.phillipsscientific.com/pdf/7186ds.pdf.

[39] www.lemo.com and www.smelectronics.us.

[40] http://www-esd.fnal.gov/esd/catalog/intro/introcam.htm.

[41] J.Streets and D.Slimmer. LINUX IEEE CAMAC library for the Jorway 411s SCSI CAMAC driver and the Jorway 73A SCSI CAMAC crate controller. www.fnal.gov, 2003.

[42] http://www.computer-methods.com/Our_Products/pp004.html.

[43] http://www.ortec-online.com/pdf/9306.pdf.

[44] http://www-esd.fnal.gov/esd/catalog/main/egg/934-spec.htm, http://www.ortec-online.com/pdf/9307.pdf.

BIOGRAPHICAL STATEMENT

Pedro Miguel Duarte was born in Bogotá, Colombia, in 1983. He received his Physics Diploma degree from Universidad de los Andes, Colombia, in 2005, his M.S. degree in Physics from The University of Texas at Arlington in 2007. In Spring 2007 he was awarded the Outstanding Physics Student award by the Department of Physics and was recognized as a University Scholar by the UTA President's Convocation for Academic Excellence.